Spin-dependence of angle-resolved photoemission from spin-orbit split surface states

Dissertation zur Erlangung des naturwissenschaftlichen Doktorgrades
der Julius-Maximilians-Universität Würzburg

vorgelegt von

Henriette Maaß
aus Hanau

Würzburg 2016

Eingereicht am: 07.12.2016
bei der Fakultät für Physik und Astronomie

1. Gutachter: Prof. Dr. Friedrich Reinert
2. Gutachter: Prof. Dr. Matthias Bode
3. Gutachter: Prof. Dr. Aitor Mugarza
der Dissertation

Vorsitzende(r): Prof. Dr. Peter Jakob
1. Prüfer: Prof. Dr. Friedrich Reinert
2. Prüfer: Prof. Dr. Matthias Bode
3. Prüfer: Prof. Dr. Johanna Erdmenger
im Promotionskolloquium

Tag des Promotionskolloquiums: 13. Juni 2017

Doktorurkunde ausgehändigt am: ....

Zusammenfassung

Spin- und winkelaufgelöste Photoelektronenspektroskopie bietet einen Einblick in die elektronische Struktur spinpolarisierter Zustände an Festkörperoberflächen. Inwieweit eine Messung der Spinpolarisation emittierter Photoelektronen den tatsächlichen intrinsischen Spincharakter eines elektronischen Zustandes wiedergibt, ist die zentrale Fragestellung der vorliegenden Arbeit. Dabei zeigt sich, dass die gemessene Spinpolarisation stark von den experimentellen Gegebenheiten wie etwa der Polarisation des einfallenden Lichtes oder der Photonenenergie abhängt und der Photoemissionsprozess eine somit nicht zu vernachlässigende Rolle für das Messergebnis spielt. Das Ziel dieser Arbeit ist es, den Zusammenhang zwischen dem Ergebnis einer spinsensitiven Messung und dem Spincharakter des Grundzustandes zu entschlüsseln und dabei ein tieferes Verständnis der Spinpolarisation im Photoemissionsprozess zu gewinnen.

Als Modellsysteme dienen dabei Materialien, die aufgrund einer starken Spin-Bahn-Kopplung spinaufgespaltene Zustände aufweisen. Daher wird zum einen der Spin-und Orbitalcharakter der elektronischen Struktur von Modellsystemen mit Rashba-artigen Oberflächenzuständen untersucht, wie sie etwa BiTeI(0001) oder die Oberflächenlegierungen $BiAg_2$/Ag(111) und $PbAg_2$/Ag(111) aufweisen. Zum anderen wird die Oberflächenbandstruktur der topologischen Isolatoren Bi_2Te_2Se(0001) und Bi_2Te_3(0001) genauer analysiert.

Mithilfe der winkelaufgelösten Photoelektronenspektroskopie mit unterschiedlicher Lichtpolarisation wird die orbitale Struktur der untersuchten elektronischen Zustände entschlüsselt. Im folgenden Schritt wird das Wissen um den orbitalen Charakter der Wellenfunktion genutzt, um durch zusätzliche Detektion des Photoelektronenspins einen Einblick in die gekoppelte Spin- und Orbitalstruktur zu gewinnen. Hierbei zeigt sich, dass sowohl der topologische Oberflächenzustand von Bi_2Te_2Se(0001) als auch der Rashba-artige Oberflächenzustand von BiTeI(0001) chirale Spinstrukturen aufweist, die an die in der Oberflächenebene orientierten p-artigen Orbitale gekoppelt sind. Für Orbitale, die tangential an den Oberflächenzustand angeordnet sind, und solche, die radial angeordnet sind, findet sich dabei eine entgegengesetzte Chiralität. Die Resultate dieser Arbeit dienen somit als Nachweis, dass die Kopplung zwischen Spin und Orbital unter dem Einfluss starker Spin-Bahn-Kopplung bei topologischen

wie nicht-topologischen Zuständen in ähnlicher Form auftritt.

Systematische photonenenergieabhängige Messungen der Spinpolarisation parallel zur Oberflächennormalen im topologischen Oberflächenzustand von Bi_2Te_3(0001) weisen eine starke Photonenenergieabhängigkeit und sogar Vorzeichenwechsel in der Photoelektronenspinpolarisation auf. In ähnlicher Weise zeigt auch die am Rashba-artigen Zustand von $BiAg_2$/Ag(111) gemessene Spinpolarisation starke Änderungen bis hin zu einer Umkehr der Spinpolarisation mit der Photonenenergie. In $BiAg_2$/Ag(111) gehen die Veränderungen der gemessenen Spinpolarisation mit deutlichen Modulationen der Photoemissionsintensität einher. Dies impliziert einen möglichen Zusammenhang zwischen den Veränderungen des Photoelektronenspins und dem Wirkungsquerschnitt des Photoemissionsprozesses.

Ein solcher Zusammenhang wird zuletzt im Rahmen eines einfachen Modells genauer untersucht. Dieses basiert auf den Übergangsmatrixelementen, die die vorgestellten Photoemissionsexperimente beschreiben, und ermöglicht es, die beobachteten Veränderungen des Photoelektronenspins auf die Kopplung des Spins an die Realraumwellenfunktion des Ausgangszustands zurückzuführen. Das Modell wird durch *ab initio*-Photoemissionsrechnungen unterstützt, die eine hohe Übereinstimmung mit den gemessenen Daten aufweisen.

ABSTRACT

Spin- and angle-resolved photoelectron spectroscopy is the prime method to investigate spin polarized electronic states at solid state surfaces. In how far the spin polarization of an emitted photoelectron reflects the intrinsic spin character of an electronic state is the main question in the work at hand. It turns out that the measured spin polarization is strongly influenced by experimental conditions, namely by the polarization of the incoming radiation and the excitation energy. The photoemission process thus plays a non-negligible role in a spin-sensitive measurement. This work is dedicated to unravel the relation between the result of a spin-resolved measurement and the spin character in the ground state and, therefore, to gain a deep understanding of the spin-dependent photoemission process.

Materials that exhibit significant spin-splittings in their electronic structure, owing to a strong spin-orbit coupling, serve as model systems for the investigations in this work. Therefore, systems with large Rashba-type spin-splittings as BiTeI(0001) and the surface alloys $BiAg_2$/Ag(111) and $PbAg_2$/Ag(111) are investigated. Likewise, the surface electronic structure of the topological insulators $Bi_2Te_2Se(0001)$ and $Bi_2Te_3(0001)$ are analyzed.

Light polarization dependent photoemission experiments serve as a probe of the orbital composition of electronic states. The knowledge of the orbital structure helps to disentangle the spin-orbital texture inherent to the different surface states, when in addition the spin-polarization is probed. It turns out that the topological surface state of $Bi_2Te_2Se(0001)$ as well as the Rashba-type surface state of BiTeI(0001) exhibit chiral spin-textures associated with the *p*-like in-plane orbitals. In particular, opposite chiralities are coupled to either tangentially or radially aligned *p*-like orbitals, respectively. The results presented here are thus evidence that a coupling between spin- and orbital part of the wave function occurs under the influence of spin-orbit coupling, independent of the materials topology.

Systematic photon energy dependent measurements of the out-of-plane spin polarization of the topological surface state of $Bi_2Te_3(0001)$ reveal a strong dependence and even a reversal of the sign of the photoelectron spin polarization with photon energy. Similarly, the measured spin component perpendicular to the wave vector of the surface state of $BiAg_2$/Ag(111) shows strong modulations and sign reversals when the

photon energy is changed. In BiAg$_2$/Ag(111) the variations in the photoelectron spin polarization are accompanied by significant changes and even a complete suppression of the photoemission intensity from the surface state, indicating that the variations of the spin polarization are strongly related to the photoemission cross section.

This relation is finally analyzed in detail by employing a simple model, which is based on an evaluation of the transition matrix elements that describe the presented experiments. The model shows that the underlying cause for the observed photoelectron spin reversals can be found in the coupling of the spin structure to the spatial part of the initial state wave function, revealing the crucial role of spin-orbit interaction in the initial state wave function. The model is supported by *ab initio* photoemission calculations, which show strong agreement with the experimental results.

TABLE OF CONTENTS

1

INTRODUCTION

The spin polarization of electronic states is attracting a lot of fascination in current solid state research, owing to its key role in spin-based device concepts like spin transistors [1] or spin-filtering devices [2]. The potential of spintronics to open a new era in the field of electronic applications triggers an increasing effort to achieve a deep understanding of the intrinsic spin properties that arise in electronic states under the influence of spin-orbit coupling [3–6].

Topological states that emerge at the surface of topological insulators as a result of the non-trivial inversion of the bulk valence and conduction band manifest helical spin-textures characterized by a locking between spin and momentum. They have become of particular interest, especially due to their robustness against scattering [7–10]. While this is the most prominent example, there is a multitude of other intriguing cases of materials with interesting spin properties induced by strong spin-orbit coupling. Other topological materials as topological crystalline insulators, which exhibit multiple Dirac cones with a complex orbital texture in their electronic structure [11–13], Weyl semimetals, which realize a gapless topological phase [14, 15] or topological Kondo insulators, characterized by their inherent interplay between a non-trivial topology and strong electronic correlations [16, 17] are attracting more and more attention. But also polar semiconductors as well as ferroelectric semiconductors [18, 19] with large spin splittings in their electronic structure show high potential for exploitation of their intrinsic spin structure, which can potentially be tuned by an extrinsic electric field [18, 19]. Other examples, where the spin-texture is frequently debated, are transition metal dichalcogenides [20–22] as well as transition metal oxides [23, 24].

The large variety of materials that exhibit spin polarized electronic states, owing to the influence of spin-orbit coupling, demonstrates the need for a spectroscopic method

that allows a spin-selective probe of band structures in solids. A well-established approach is spin- and angle-resolved photoelectron spectroscopy, which allows to measure the spin of photoelectrons emitted from a solid. A long succession of photoemission experiments as well as theoretical models shows that the photocurrent is spin polarized for photoemission from magnetic materials [25–27], as well as materials with an intrinsic spin polarization governed by spin-orbit coupling [28–31], but also for photoelectrons from unpolarized or degenerate ground states [32–34]. The actual spin polarization measured in these experiments in many cases depends a lot on the symmetries which are present [29, 31, 35]. Despite these observations, the measured photoelectron spin from spin polarized ground states is often directly attributed to the initial state wave function. The influence of the photoemission process in such an interpretation is completely neglected. The question remains, however, whether the relation between the measured photoelectron spin and the spin properties of the initial state is in fact that simple. What role does for instance spin-orbit interaction in the initial state play for a spin-resolved experiment? Can the influence of the final state be neglected when considering the spin polarization and what role do in general the photoemission cross section and experimental geometry play?

To disentangle the spin properties of the initial state from effects that arise due to the photoemission process, a systematic investigation of the role of symmetries in the experiment as well as the photoemission final state for the measured spin polarization is essential. For such fundamental investigations, it is sensible to start out with model materials that are characterized by strong spin-orbit coupling and, therefore, show a spin polarized electronic structure, where the separation in energy and momentum between states of different spin character is large enough to be easily accessible by spin- and angle-resolved photoelectron spectroscopy. Besides, whereas many experimental or theoretical works focus on either topological or non-topological states, a direct comparison can yield insight into the role of spin-orbit coupling as well as the non-trivial topology with regard to spin polarization effects. Therefore, the experiments which will be presented in this work, are based on a variety of model materials, covering topological as well as non-topological states: thin films with a simple two-dimensional structure like for example the surface alloy $BiAg_2/Ag(111)$, as well as layered van-der-Waals crystals as the topological insulator $Bi_2Te_3(0001)$ or the giant-Rashba semiconductor BiTeI are investigated to gather an overall picture of spin polarization effects from materials with different structure and topology.

This work is dedicated to deepen the understanding of the spin properties in strongly spin-orbit coupled systems using spin- and angle-resolved photoelectron spectroscopy. In particular, a systematic and detailed examination of the relation between the measured photoelectron spin polarization and the intrinsic spin structure inherent to an electronic state is performed. Gaining insight into the role of the experimental

conditions for the measured spin polarization is a prerequisite in the careful design of an experiment that is fitting for a specific material and scientific question.

<p style="text-align:center">∗∗∗</p>

The results which will be presented in this work are based on spin-resolved as well as spin-integrated photoelectron spectroscopy on topological insulators and materials with Rashba-type spin splittings in their electronic structure. The principal theoretical concepts which are the basis for understanding the electronic structure as well as the spin properties in these materials — namely spin-orbit coupling, which is a main ingredient for the Rashba-Bychkov effect and the emergence of topological states — are shortly described in chapter 2. In chapter 3 the methodical approach by photoelectron spectroscopy as well as the experimental setups are introduced. Chapter 2 and 3, therefore, summarize the theoretical as well as methodical foundation for the analysis in the subsequent chapters.

A short overview over the model materials which were examined in this work is presented in chapter 4. In particular their crystal as well as electronic structure is briefly introduced and their specific benefits regarding the scientific questions addressed in this work are summarized.

Chapter 5 and 6 are focused on the detailed description and discussion of the experimental results. Thereby, the first part, namely chapter 5.1, is concerned with the orbital character of the electronic states. In the following, the question of how the spin-orbit interaction manifests itself in the spin character of different orbital parts of the wave function is addressed in chapter 5.2. Some of the content presented in chapter 4 and 5 of this work was already published [36, 37].

Chapter 6 summarizes the influence of the photon energy on the measured photoelectron spin polarization of the topological surface state in a layered topological insulator (chapter 6.1) as well as two-dimensional states in surface alloys (chapter 6.2). The results are utilized to develop a model description of the relation between the photoelectron spin polarization and the intrinsic spin of an electronic state. In chapters 5 and 6 a particular focus is dedicated to the role of spin-orbit coupling in the ground state as well as topology and crystal structure of the material for the outcome and correct interpretation of a spin-resolved photoemission experiment. Finally, the work will finish with a conclusive discussion and outlook in chapter 7.

2

SPIN POLARIZED ELECTRONIC STATES IN SOLIDS

2.1 Spin-Orbit Coupling

Spin-orbit coupling (SOC) is the driving force for the emergence of spin polarized electronic states in solids. It describes the interaction between the spin and orbital momentum of an electron and leads to many interesting phenomena in the electronic structure of solid states. At the surface of a crystalline solid, for example, the breaking of inversion symmetry together with spin-orbit coupling leads to the energy splitting of two-dimensional electron gases, called Rashba-Bychkov effect [38, 39]. The Rashba-Bychkov effect will be described in section 2.3. In topological insulators spin-orbit coupling is responsible for the inversion of the band order, which mediates the existence of helical Dirac fermions in the energy gap [9], as summarized in section 2.4. The following pages give a short overview of spin-orbit coupling and its relevance for the spin structure associated with electronic states.

In the framework of a non-relativistic approximation of the Dirac equation, spin-orbit coupling can be described by the Hamiltonian H_{SOC} for an electron in the electrostatic potential V of the nucleus [40]:

$$(2.1) \qquad H_{SOC} = \frac{\hbar}{4m_e^2 c^2} \boldsymbol{\sigma} \cdot (\nabla V \times \boldsymbol{p}),$$

The Pauli matrix vector $\boldsymbol{\sigma} = (\sigma_x, \sigma_y, \sigma_z)$ is the spin operator, p the momentum operator, m_e stands for the free electron mass, $\hbar = \frac{h}{2\pi}$ is the reduced Planck constant, and c is the speed of light. The potential gradient ∇V is highest close to the nucleus

and depends on the atomic number Z. The atomic spin-orbit coupling is, therefore, especially pronounced in high Z elements as for example Bi or Pb.

The coupling between the spin $\mathbf{S} = \frac{\hbar}{2}\boldsymbol{\sigma}$ and the orbital momentum $\mathbf{L} = \mathbf{r} \times \mathbf{p}$, is implicitly included in the spin-orbit Hamiltonian H_{SOC}. This becomes easily visible, when a spherically symmetric potential $\nabla V = \frac{\mathbf{r}}{r}\frac{dV}{dr}$ is assumed, yielding [41]:

$$(2.2) \qquad H_{SOC} = \frac{1}{2m_e^2 c^2}\frac{1}{r}\frac{dV(r)}{dr}\mathbf{L}\cdot\mathbf{S}.$$

Due to the coupling ($\mathbf{L}\cdot\mathbf{S}$) of spin $\mathbf{S}$ and orbital momentum $\mathbf{L}$, the two momenta $\boldsymbol{S}$ and $\boldsymbol{L}$, separately, are no good quantum numbers anymore and $[S,L] \neq 0$. The total momentum $\boldsymbol{J}$, on the other hand, fulfills the commutation relation $[H,\boldsymbol{J}] = 0$ and its eigenvalues are also eigenvalues of the Hamiltonian H which describes the system. $\boldsymbol{J}$ has two possible values, $\boldsymbol{J} = \boldsymbol{L} \pm \boldsymbol{S}$, depending on whether the magnetic moments associated with the spin and the orbit of the electron are aligned parallel or antiparallel. As a result, two states emerge, which are split in energy. The spin-orbit splitting can be observed in the energy levels of atoms or molecules as well as in core levels of solids. It is for example large for core levels of heavy elements, where it can reach values up to over $100\,\mathrm{eV}$ [42].

Spin-orbit coupling leads to additional effects in the band structure of solids. Before describing different mechanisms that lead to a spin-splitting in the presence of spin-orbit coupling, a simple model of the electronic structure in crystalline solids will be revised.

2.2   Electronic states in solids

In an ideal infinite periodic crystal the wave function $\Psi_{\boldsymbol{k}}(\boldsymbol{r})$ can be described in a simple picture via the Bloch theorem [43, 44]. Within the Bloch description, the periodicity of the crystal is expressed by a weak periodic potential $V(\boldsymbol{r}) = V(\boldsymbol{r}+\boldsymbol{R})$, where $\boldsymbol{R}$ is the crystal lattice vector, and the electrons are considered as nearly free electrons. Without spin-orbit coupling the solutions of the Schrödinger equation yield [44]:

$$(2.3) \qquad \Psi_{\boldsymbol{k}}(\boldsymbol{r}) = e^{i\boldsymbol{kr}}u_{\boldsymbol{k}}(\boldsymbol{r}).$$

The function $u_{\boldsymbol{k}}(\boldsymbol{r})$ adopts the periodicity of the lattice, therefore, $u_{\boldsymbol{k}}(\boldsymbol{r}) = u_{\boldsymbol{k}}(\boldsymbol{r}+\boldsymbol{R})$. In an ideal infinite crystal the momentum $\boldsymbol{k}$ must be real [45] and the energy eigenvalues E that correspond to the wave function describe dispersing bands $\epsilon(\boldsymbol{k})$. All possible bands in their entirety yield the electronic structure of the crystal.

For the electronic structure the symmetries of the system are crucial. An infinite crystalline solid can be time inversion symmetric as well as spatial inversion

symmetric:

(2.4)
$$\text{time inversion symmetry:}\quad E(\boldsymbol{k},\uparrow) = E(-\boldsymbol{k},\downarrow)$$
$$\text{spatial inversion symmetry:}\quad E(\boldsymbol{k},\uparrow) = E(-\boldsymbol{k},\uparrow),$$

where the electron spin is expressed as $(\uparrow,\downarrow)$. If both symmetries are present, the existence of a solution $E(\boldsymbol{k},\uparrow)$ with an energy E at the wave vector $\boldsymbol{k}$ and with a spin $(\uparrow)$ requires the existence of a second state $E(\boldsymbol{k},\downarrow)$ at the same energy but with opposite spin since $E(\boldsymbol{k},\uparrow) = E(-\boldsymbol{k},\downarrow) = E(-\boldsymbol{k},\uparrow)$. Therefore, the electronic bands are at least twofold degenerate. If one of the symmetries is broken, however, the spin degeneracy – also termed Kramers degeneracy – can be lifted by spin-orbit coupling and spin polarized electronic states can exist.

A breaking of inversion symmetry occurs for instance, if the crystal is semi-infinite and the periodicity of the potential is perturbed along the direction $\boldsymbol{e}_z$ perpendicular to the boundary between crystal and vacuum. In a simple approximation, a step function can be assumed to account for the potential change at the transition between the crystal, where $V = 0$, and the vacuum level V_{vac}. The resulting wave functions decrease exponentially into the vacuum. As a consequence, the wave vector $k_\perp$ perpendicular to the boundary, which is real in the infinite case, can now adopt complex values, in which case the wave function decays exponentially not only into the vacuum but also into the bulk of the crystal [45]. In such a case the wave function describes surface or boundary states, since the electrons are strongly confined in the direction $\boldsymbol{e}_z$ perpendicular to the boundary between crystal and vacuum, whereas they can move freely within the boundary plane. The energy eigenvalues of surface states are located in the energy gap of the bulk band structure. In the presence of spin-orbit coupling they can obtain different values depending on the spin character, owing to the broken inversion symmetry at the surface.

To correctly describe spin polarized states, the wave function must be written as a linear combination of Bloch wave functions $\psi_{\boldsymbol{k}}(\boldsymbol{r})$ coupled to opposite spinors with spin-up $\chi_\uparrow$ or spin-down $\chi_\downarrow$ [46]:

(2.5)
$$\Psi_{\boldsymbol{k}}(\boldsymbol{r}) = \psi_{\boldsymbol{k},1}(\boldsymbol{r}) \cdot \chi_\uparrow + \psi_{\boldsymbol{k},2}(\boldsymbol{r}) \cdot \chi_\downarrow.$$

The quantization axis can in principle be chosen arbitrarily, ideally in a way that simplifies the treatment of the particular spin configuration. The wave functions $\psi_{\boldsymbol{k},1}(\boldsymbol{r})$ and $\psi_{\boldsymbol{k},2}(\boldsymbol{r})$, however, depend on the choice of the quantization axis [46]. If a different quantization axis is chosen, the new wave functions can be expressed in terms of linear combinations of the original ones [46].

2.3 The Rashba effect

If a free electron gas is influenced by an electric field, which confines the propagation of the electron along one direction, a two-dimensional electron gas (2DEG) emerges. In this case, the spin-orbit coupling Hamiltonian is reduced to the Rashba-Hamiltonian H_R, which is given by [39, 47]:

$$(2.6) \qquad H_R = \alpha_R \boldsymbol{\sigma} \cdot (\boldsymbol{e}_z \times \boldsymbol{k}).$$

The electric field is for instance induced by the potential barrier $V(z)$ at the surface of a material. The resulting $\boldsymbol{k}_{||}$-dependent energy splitting of a two-dimensional electron gas was first described by Rashba and Bychkov [39] and is termed Rashba-Bychkov effect. If inversion symmetry is broken in the bulk of the material, a similar effect occurs, called Dresselhaus effect [48] or bulk-Rashba effect. The Rashba parameter α_R, which is a constant in case of an ideal 2DEG, is proportional to the expectation value of the potential gradient $\alpha_R \propto \langle \Psi | \nabla V(z) | \Psi \rangle$, where Ψ is the Bloch wave function of an electron moving freely along the $x - y$-plane [49]. The Rashba-Hamiltonian results in the splitting of the characteristic parabolic band of a 2DEG into two branches E^+ and E^-:

$$(2.7) \qquad E^{\pm}(\boldsymbol{k}_{||}) = E_B + \frac{\hbar^2 \boldsymbol{k}_{||}^2}{2m^*} \pm |\alpha_R| |\boldsymbol{k}_{||}|.$$

The size of the splitting scales with the Rashba parameter α_R and is proportional to the wave vector $|\boldsymbol{k}_{||}|$. The effective mass of the Rashba-split electronic state is given by m^*.

The spin polarization $\boldsymbol{P}$ of a Rashba-split 2DEG can be calculated from the expectation values $\boldsymbol{P}^{\pm} = \langle \Psi^{\pm} | \boldsymbol{\sigma} | \Psi^{\pm} \rangle$ of the Pauli matrices $\boldsymbol{\sigma}$ with the eigenfunctions $\Psi^{\pm}$ of the Rashba Hamiltonian H_R. The resulting spin polarization is:

$$(2.8) \qquad \boldsymbol{P}_{\pm}(\boldsymbol{k}_{||}) = \pm \frac{\alpha_R}{|\alpha_R|} (-k_y, k_x, 0) / |\boldsymbol{k}_{||}|.$$

The spin in the Rashba model for an ideal 2DEG is, therefore, aligned perpendicular to the wave vector $\boldsymbol{k}_{||}$ as well as the surface normal $\boldsymbol{e}_z$. The spin direction is defined by the sign of the Rashba parameter α_R.

The Rashba-splitting of a two-dimensional electron gas is schematically depicted in Fig. 2.1 (a). The upper panel shows the band structure in the $\boldsymbol{k}_{||}$-plane at the Fermi energy E_F, while the lower panel illustrates the dispersion $E(\boldsymbol{k}_{||})$. The two branches of the state are displayed in blue for the lower branch E^- and yellow for the upper branch E^+. An important parameter that quantifies the size of the splitting is the momentum offset $k_0 = \alpha_R m^*/\hbar^2$. The branches E^+ and E^- are separated by a value of
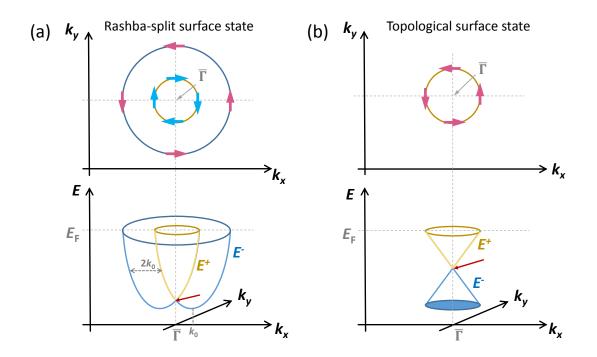
FIGURE 2.1. **Schematic of spin polarized surface states** (a) shows the dispersion of a two-dimensional electron gas, which is split into an upper (+) branch (yellow) and a lower (−) branch (blue) by the Rashba-effect. The two branches are termed E^+ and E^-, respectively. The size of the splitting can be defined by the momentum offset k_0. In the upper panel the Fermi surface of the state is displayed. The spin polarization as deduced from the Rashba-Bychkov model is indicated by arrows and has opposite chirality for the upper and lower branch E^+ and E^-. (b) shows a schematical illustration of a topological surface state with a linear dispersion. The lower panel shows the dispersion $E(\boldsymbol{k}_{\parallel})$. Correspondingly to the Rashba case, the state can be described by an upper and lower branch E^+ and E^-, which exhibit opposite spin chirality in the model description. The chiral spin structure of the surface state is displayed in the upper panel by arrows. Both types of surface states exhibit Kramers degenerate points at the high symmetry point $\bar{\Gamma}$, indicated by red arrows.

$2k_0$, which does not depend on $\boldsymbol{k}_{\parallel}$ in the Rashba model for an ideal 2DEG. The spin polarization as described in the Rashba-Bychkov model is depicted in the upper panel, which shows the opposite spin chirality of the two branches.

The concept of energy splittings of electronic bands that emerge in inversion asymmetric environments under the influence of spin-orbit coupling was first introduced by Dresselhaus [48] and Rashba [38]. In 1984, Bychkov and Rashba developed their simple model of the effect for two-dimensional electron gases in semiconductor het-

erostructures [39]. The first experimental observation of a Rashba-type spin-splitting was reported for the surface state of Au(111) [50] in an angle-resolved photoelectron spectroscopy study, quickly followed by several subsequent studies of the effect [28, 51–53]. Spin-splittings governed by spin-orbit coupling were soon found in other heavy elements as for example in the surface electronic structure of Bi(111), Bi(110), Bi(100) [54–56], Sb(111) [57], Ir(111) [58] and Cu(111) [59]. The spin-splitting is strongly enhanced in surface alloys that form on nobel metal surfaces by incorporation of the heavy elements Bi or Pb. Large splittings were for instance observed in the surface electronic structure of Pb/Ag(111), Bi/Ag(111) and Bi/Cu(111) [60–63]. In the bulk and surface electronic structure of polar semiconductors, which exhibit an inversion asymmetric crystal structure, namely BiTeI, BiTeCl and BiTeBr, giant Rashba-type splittings appear [64–68].

2.4 Topological Insulators

Topological order allows to classify different states of matter by specific topological properties which are robust under smooth changes of material parameters. A topological phase transition requires a change of the topological property which can for instance be the number of gapless boundary states in the band structure of a material, the quantized Hall conductance in a Hall insulator, or in a more general example the number of holes in a geometrical object [9]. For example, a trivial insulator or semiconductor exhibits a bulk band gap and its Hamiltonian can be smoothly transformed into that of the vacuum without requiring a closing of the gap. Therefore, in terms of topological order, a trivial insulator is in the same class as the vacuum.

There are, however, topologically non-trivial insulators, which likewise exhibit a bulk band gap. Thereby, unlike a trivial insulator, the bulk bands neighboring the energy gap are inverted, due to a sizable spin-orbit interaction [8]. This immediately implies that in order to transform the topologically non-trivial bulk band structure into that of a normal insulator, the band-gap must close [9].

Since the band gap vanishes during the topological phase transition, gapless edge or surface states with an intrinsic spin polarization emerge at the interface between a topological insulator and a topologically trivial one [7, 9]. The connection between the topology of the bulk band structure and the existence of such topological surface states is often termed bulk-boundary correspondence [69]. The topological surface states exhibit interesting properties as a consequence of their non-trivial origin. They obey time-reversal symmetry and the spin is locked perpendicular to the momentum [30]. States of a particular spin character are thus limited to one propagation direction [9], which immediately implies that backscattering is strongly suppressed since no

adequate states are available [9]. As a consequence, the topological states are robust against perturbations which obey time reversal symmetry, a clear distinction from surface states of a topologically trivial origin. Moreover, the wave function that describes the topological surface states is distinguishable from Rashba-type materials by the number of eigenstates along one direction of the crystal momentum $\boldsymbol{k}_{\parallel}$ at a given energy E, which is always odd for a topological state, whereas it is even in case of Rashba-Bychkov materials [49]. In other words, the number of surface states that cross the Fermi energy E_F between two boundary Kramers degenerate points is always odd in a topological insulator, whereas it is even for a Rashba-type state [9].

Topological insulators can be classified in terms of topological invariants ν, so called $\mathbb{Z}_2$ invariants, which can be either even, when the material is topologically trivial, or odd, otherwise. Therefore, only two possible values $\nu_0 = 0, 1$ are needed to distinguish between the material classes. In three-dimensional materials, four topological invariants exist. Whereas the first one ν_0 classifies a strong topological insulator, the others $\nu_{1,2,3}$ characterize a weak topological insulator [7].

There are different approaches to calculate the topological invariant ν_0 [7, 70–72]. In an inversion symmetric crystal it is convenient to consider time reversal invariant momenta (TRIM) Γ_i, where all electronic states are required to be Kramers degenerate as an immediate consequence of time reversal symmetry [7]. Away from the TRIM, spin-orbit coupling lifts the degeneracy and the topological states are spin polarized. To quantify the topological invariant, the parity eigenvalues $\xi_{2m}(\Gamma_i) = \pm 1$ of the $2m$th occupied Bloch states at all TRIM Γ_i are multiplied [7]:

$$(2.9) \qquad \delta_i = \prod_{m=1}^{N} \xi_{2m}(\Gamma_i).$$

The product involves the $2N$ occupied bands at the N TRIM. For a three-dimensional system the Number of TRIM is eight, therefore $N = 8$. The invariant ν_0 can then be deduced from the product over all δ_i [7]:

$$(2.10) \qquad (-1)^{\nu_0} = \prod_{i=1}^{N=8} \delta_i.$$

An ideal topological surface state of a three-dimensional topological insulator exhibits a characteristic cone-like dispersion, where the tips of the cone are located at the twofold degenerate projections Λ_j of the eight bulk TRIM to the surface Brillouin zone. The linear topological surface states are often termed Dirac-cones and the twofold degenerate crossing points are named Dirac points. A schematic illustration of the helical surface states and their intrinsic spin texture is displayed in Fig. 2.1 (b). The lower panel shows the linear cone-like dispersion $E(\boldsymbol{k}_{\parallel})$ of the state. The Kramers degenerate Dirac point is marked by a red arrow. To compare the band structure of

the topological surface state to the Rashba-type state shown in (a) it is convenient to describe it by an upper and lower cone (E^+ and E^-), which are indicated by yellow and blue, respectively, and which in a simple model exhibit opposite spin directions. The upper panel illustrates the intrinsic helical spin structure of the surface state at the Fermi energy E_F. Light red arrows mark the spin, which is in an ideal linear case oriented in the $k_x - k_y$-plane and rotates around the Fermi surface with $\boldsymbol{S} \perp \boldsymbol{k}_{\parallel}$.

The first experimental verification of a topological state was reported 2007 for CdTe/HgTe quantum wells, which realize a two-dimensional topological insulator above a critical thickness of a HgTe layer between CdTe layers [73]. The s- and p-like bands in the band structure of the layered CdTe/HgTe system exhibit the expected band inversion as a result of strong spin-orbit coupling and the system was shown to be topologically non-trivial [74]. The first realization of a three-dimensional topological insulator was reported for $Bi_{1-x}Sb_x$ [30, 75]. Here, with increasing percentage of Sb, a topological phase transition occurs and topological surface states emerge. Other prominent examples for three-dimensional topological insulators are the chalcogenides Bi_2Te_3, Bi_2Se_3, as well as Sb_2Te_3 and related materials [8, 76].

2.5 Spin polarization in photoelectron spectroscopy

The Rashba-Bychkov effect and topological insulators exhibit spin polarized electronic states, which are induced by spin-orbit coupling. Their investigation in terms of the spin character often relies on spin-sensitive photoemission experiments, which became possible with the exploitation of Mott scattering [77] in the first Mott detector developed in 1943 [78]. Since these early experiments measurements of the photoelectron spin, as well as their correct interpretation, still remain challenging. Spin detection by Mott scattering is now a well established method [79–81] but also different mechanisms soon became feasible. A milestone in the development of spin detection was doubtless the first successful record of spin-dependent scattering in a specular LEED experiment [82] and its implementation in a spin-, angle- and energy-resolving photoemission experiment [32]. A different approach utilizes spin-dependent scattering processes on a magnetized scattering target [83].

Hand in hand with the emergence of spin polarization detection, theoretical and experimental efforts were made to understand the origin of the spin polarization of electrons emitted from solids or atoms by photoemission. Thereby, many of the early experiments already revealed that symmetries, which are present in the photoemission experiment given by the material itself or the experimental setup, are of high relevance for the photoelectron spin polarization. A short summary of the

developments in these early investigations of the photoelectron spin will be given in the following.

One of the first predictions of spin polarized photoelectrons was given in 1969 by U. Fano [84], who showed that when circular polarized light is used to photoionize vaporized Cs atoms, the emitted photoelectrons are spin polarized. The reason can be found in a splitting of the total momentum j into $j = l \pm s$ resulting in two unequal p continuum states with $j = 3/2$ or $1/2$, due to spin-orbit coupling in the Cs atoms. Therefore, two possible transitions from the $6s$ ground state, which is not affected by spin-orbit coupling, to the continuum states $p_{1/2}$ and $p_{3/2}$ with different photoemission cross sections can occur. The superposition of the respective transition matrix elements leads to a spin polarization of the photoemitted electrons. The spin polarization of photoelectrons emitted from Cs atoms by circularly polarized light and the predicted photon wavelength dependence of the Fano-effect were soon experimentally verified [85, 86].

Many of the following early spin-resolved photoemission experiments were performed with circularly polarized light in a maximal symmetric environment, where the incidence of light was normal to the material and electrons emitted normal to the surface of solid state materials [87, 88] or from atomic targets, for example atoms absorbed on the surfaces of nobel metals [89, 90], were detected. It turned out that the emission of spin polarized photoelectrons is not limited to magnetic materials [25], but can in fact also be observed for non-magnetic targets [87]. In non-magnetic materials the underlying mechanism can be traced back to dipole selection rules for circularly polarized light, which allows only certain transitions depending on whether right or left handed circular polarized light is used.

Circular polarized light with either left or right handed circularity can yield different photoemission intensities due to optical selection rules and can thus give information about the symmetry properties of the electronic bands of a material without the use of a spin-resolving detector [91]. This circular dichroism in the angular distribution of photoelectrons (CDAD) was — and still is — frequently used in order to analyze the electronic states involved in a transition [92–95].

The experimental alignment was revealed to be a crucial factor for the observed photoelectron spin polarization. An asymmetry can for example be introduced, when photoelectrons emitted off-normal with respect to the sample surface are detected [96–98] revealing an angular dependence of the spin polarization. But also the direction of light incidence can induce changes of the photoelectron spin polarization. For light incidence normal to the surface of Ag(100) for example, the measured spin polarization was shown to be always parallel to the surface normal. For oblique light incidence, however, deviations from the spin polarization alignment normal to the surface were

observed [35].

Also linear or even unpolarized light was found to yield spin polarized photo-electrons. For linear light incident normal to the surface of a solid state material, this was first discussed for crystals of C_{3v} symmetry [33]. It was predicted that the photoelectrons excited by linearly polarized light can in principle be polarized along the direction perpendicular to a mirror plane as a result of spin-orbit coupling in the initial state [33]. The existence of a photoelectron spin polarization of electrons excited by linearly polarized light was soon experimentally confirmed [99]. Similarly, spin polarized photoelectrons ejected by unpolarized light were experimentally observed on Xe atoms [100] in accordance to theoretical predictions [101, 102]. These results represent only a few examples of the early advances in the investigation of the spin polarization in photoemission which already reveal that photoelectrons are in many cases spin polarized.

The measurement of the spin polarization of photoemitted electrons is now a well established method, applied frequently to gain insight into the electronic structure of different materials with respect to their spin properties. Especially in the investigation of the Rashba-effect, where spin-orbit coupling leads to an intrinsic spin-polarization but also in experimental studies of topological insulators spin-resolved photoemission experiments play an important role.

3

3.1   Photoelectron Spectroscopy

A lot of current solid state research is aimed at unraveling the electronic configuration in solid state materials — in particular with regard to the spin polarization. The photoelectric effect, observed 1887 by Heinrich Hertz [103] and explained 1905 by Albert Einstein [104], describes the photoexcitation of an electron from a bound state in a solid. It is the basis of spin- and angle-resolved photoelectron spectroscopy, the primary method to probe the electronic structure of a material. The energetics of the photoemission process can be expressed as [105]:

$$(3.1) \qquad E'_{kin} = h\nu - |E_{bind}| - \Phi_S,$$

where E'_{kin} is the kinetic energy of the electron, $h\nu$ is the energy of the incoming light, Φ_S is the work function of the material, and $|E_{bind}|$ is the binding energy of the electron inside the solid relative to the Fermi energy E_F. In practice, the sample is electrically connected to the same potential as the analyzer so that their chemical potential is equal. Therefore, it is not necessary to determine the work function Φ_S of the material, merely the work function Φ_A of the analyzer needs to be known and the binding energy can be determined by:

$$(3.2) \qquad E_{kin} = h\nu - |E_{bind}| - \Phi_A.$$

The retarded energy E_{kin} is detected in the photoemission experiment.

Photoelectron spectroscopy is a surface sensitive method, since the information depth depends on the inelastic mean free path λ of the electrons. λ is a material

specific quantity that in addition depends on the kinetic energy of the electrons. An empirical description of the dependence of the inelastic mean free path on the kinetic energy of the electron is given by the so called universal curve, which roughly follows the formula [106]:

$$(3.3) \qquad\qquad \lambda = 0.41a^{3/2}\sqrt{E_{kin}},$$

with the lattice constant a of the material in nm and the kinetic energy E_{kin} in eV. Typically, the value for λ at energies between 10 eV and 2000 eV is in the range of a few Å [105]. Photoelectron spectroscopy is thus ideally suited to investigate the electronic structure at the surface of a material.

Depending on the photon energy $h\nu$ and the exact configuration of the experimental setup, photoelectron spectroscopy can be used to gather information about the chemical composition, the band structure of the material, its orbital configuration, and the spin polarization of the emitted photoelectrons. In **x**-ray **p**hotoelectron **s**pectroscopy (XPS) photon energies above $h\nu \approx 100$ eV are used to excite electrons from deeply bound core level states. The core level binding energies yield information about the chemical environment of the atom in the sample and allow an analysis of the chemical composition of the material. In this work XPS is solely used for a preliminary sample characterization. The actual experiments were performed using **a**ngle-**r**esolved **p**hoto**e**lectron **s**pectroscopy (ARPES), where typically photon energies between $h\nu \approx 5$ eV and 100 eV are applied to map the valence band structure of a material. In addition, **s**pin- and **a**ngle-**r**esolved **p**hoto**e**lectron **s**pectroscopy (SARPES) was employed, which allows to access the photoelectron spin polarization.

3.2 Angle-resolved photoelectron spectroscopy

In ARPES the emission angle (φ,ϑ) of the photoemitted electrons is measured in addition to their kinetic energy E_{kin} in order to gain information about the momentum $\boldsymbol{k}_{crys}$ of the electrons inside the crystal. If an electron is excited by an incoming photon and travels to the surface without being scattered, its momentum is conserved under the condition that the photon wave vector can be neglected. This is an adequate assumption for photon energies below ≈ 100 eV as typically used in ARPES [105]. As a result, the optical transition between the bulk initial and final state, with $\boldsymbol{k}_i$ and $\boldsymbol{k}_f$, respectively, is a transition between points in momentum space which are related to each other by the reciprocal lattice vector $\boldsymbol{G}$ with $\boldsymbol{k}_f - \boldsymbol{k}_i = \boldsymbol{G}$ [107]. An equivalent description employs a reduced-zone scheme, where the transition is a vertical one and the relation between the momentum in the initial and final state can be simplified to $\boldsymbol{k}_f - \boldsymbol{k}_i = 0$ [107]. At the surface, however, the photoelectron gets

refracted and the momentum is changed. Since translational symmetry is broken along the surface normal, only the momentum component parallel to the surface is preserved and $\boldsymbol{k}_{crys,||} = \boldsymbol{k}_{vac,||} = \boldsymbol{k}_{||}$. The photoelectron leaves the sample under an angle ϑ relative to the surface normal and under an azimuthal angle φ (compare Fig. 3.1). From a simple geometrical analysis of the relation between the wave vector $|\boldsymbol{k}_{||}| = \sqrt{k_x^2 + k_y^2}$ and the emission angle one obtains:

(3.4)
$$k_x = \sqrt{\frac{2m_e}{\hbar^2} E_{kin}} \sin\vartheta \cos\varphi,$$

$$k_y = \sqrt{\frac{2m_e}{\hbar^2} E_{kin}} \sin\vartheta \sin\varphi,$$

where m_e is the mass of the electron and $\hbar = \frac{h}{2\pi}$ the reduced Planck constant. The momentum component $k_{crys,\perp} = k_\perp$ perpendicular to the surface, however, is changed and

(3.5)
$$k_\perp = \frac{1}{\hbar}\sqrt{2m_e(E_{kin}cos^2\vartheta + V_0)},$$

where V_0 is the inner potential, which can for instance be determined with the help of band structure calculations [107]. Another approach to retrieve V_0 and consequently $k_\perp$ are systematic photon energy dependent measurements, where photoelectrons at normal emission are detected. In order to determine the $k_\perp$ dispersion in the initial state, the structure of the photoemission final state must be known. Hereby, band structure calculations can once more be of use. In many cases, on the other hand, the photoemission final state is simply assumed to be a free electron parabola [107]. Two-dimensional electronic states do not show a dispersion along $k_\perp$, which can in such a case be neglected.

3.3 The photoemission process

The total photocurrent $I(\boldsymbol{k}, E_{kin})$ at a momentum $\boldsymbol{k}$ as a function of the kinetic energy E_{kin} of the electron is proportional to the transition probability $w_{f,i}$ for an optical excitation from the initial state Ψ_i to the final state Ψ_f: $I(\boldsymbol{k}, E_{kin}) \propto w_{f,i}$ [105, 108, 109]. In a non-relativistic Schrödinger approach the interaction between the electron and the electromagnetic vector potential **A** of the incoming light can formally be described by Fermi's golden rule, with [105]:

(3.6)
$$w_{f,i} \propto \frac{2\pi}{\hbar} |\langle \Psi_f | H_{int} | \Psi_i \rangle|^2 \delta(E_f - E_i - h\nu),$$

where the δ-function describes the energy conservation with the initial and final state energies E_i and E_f. The interaction Hamiltonian H_{int}, which describes the

perturbation of the system by the incident radiation, can be developed by replacing the momentum operator $\mathbf{p}$ of a free electron by $\mathbf{p} - (e/c)\mathbf{A}$ for an electron with charge e and mass m_e in an electromagnetic field, yielding [108, 110]:

$$(3.7) \qquad H_{int} = \frac{e}{2m_e c}(\mathbf{A} \cdot \mathbf{p} + \mathbf{p} \cdot \mathbf{A}).$$

In the Hamiltonian H_{int} above, a gauge is chosen in such a way that the scalar potential is zero: $V(\boldsymbol{r}) = 0$. Furthermore, the quadratic term $\mathbf{A}^2$ is neglected as it does only contribute at very high photon fluxes [110]. If additionally the commutation relation $[\mathbf{A}, \mathbf{p}] = i\hbar\nabla\mathbf{A}$ is used, and a constant vector field $\boldsymbol{A}$ is assumed, which holds for wavelengths in the ultraviolet regime when surface photoemission contributions can be neglected, then $\nabla\mathbf{A} = 0$ and H_{int} can be simplified to [107, 108]:

$$(3.8) \qquad H_{int} = \frac{e}{m_e c}\mathbf{A} \cdot \mathbf{p}.$$

For spin polarized electrons in external fields a more general expression is the Dirac equation, a relativistic generalization of the Schrödinger equation, where the electron is treated as a particle carrying spin [111]. The Dirac Hamiltonian H_{Dirac} in its nonlinearized form, and with the approximation that the kinetic and potential energies are small compared to $m_e c^2$, can be expressed as [111]:

$$(3.9) \quad H_{Dirac} = \frac{1}{2m_e}(\mathbf{p} - \frac{e}{c}\mathbf{A})^2 + eV(\boldsymbol{r}) - \frac{e\hbar}{2m_e c}\boldsymbol{\sigma} \cdot \mathbf{B} + i\frac{e\hbar}{4m_e^2 c^2}\mathbf{E} \cdot \mathbf{p} - \frac{e\hbar}{4m_e^2 c^2}\boldsymbol{\sigma} \cdot (\mathbf{E} \times \mathbf{p}).$$

The first two terms are equal to the Schrödinger equation for an electron in an external field with the potential $V(\boldsymbol{r})$. The additional terms depend on the spin, which is expressed by the Pauli matrices $\boldsymbol{\sigma}$. The $\boldsymbol{\sigma} \cdot \mathbf{B}$ term describes the interaction of the spin with an external magnetic field $\mathbf{B}$. The fourth term is a relativistic energy correction, where $\mathbf{E}$ is an electric field and the last term is the spin-orbit interaction H_{SOC}.

The spin dependent terms in the Dirac Hamiltonian induce a spin polarization of the photoelectrons. The spin-orbit term can lead to a spin polarization of the initial state, whereas the $\boldsymbol{\sigma} \cdot \mathbf{B}$-term can trigger spin-flip transitions [112]. At energies typically used in ARPES the probability of a spin-flip transition, however, is about two orders of magnitude smaller than transitions, where the spin is conserved [113]. Therefore, it is appropriate to assume, that the optical excitation process preserves the spin.

The matrix element $M_{f,i} = \langle \Psi_f | H_{int} | \Psi_i \rangle$ introduces dipole selection rules, which are expressed as $\Delta l = \pm 1$ and $\Delta m_l = 0$ for linearly polarized light and $\Delta m_l = \pm 1$ for circularly polarized light in a non-relativistic approach [112]. The dipole selection rules can yield information about the symmetries of the initial and final state, when the geometry of the experiment is taken into account.

3.4 One-step photoemission theory and inverse-LEED formalism

The photoemission process is often described in a three-step model [114], where the complete process is divided into the optical excitation of a photoelectron, its travel to the surface of the solid, and its transmission through the surface into the vacuum where it is measured [105, 108]. This phenomenological model constitutes a comprehensible approach and adequately approximates the photoemission process. A more realistic model, however, is the one-step theory, where an excitation from an initial state into a damped final state near the surface is described in a single step [105]. The following descriptive summary of the one-step formalism closely follows the approach in reference [105].

In principle, Fermi's Golden Rule in equation 3.6 is a suitable expression for the one-step photoemission process, if the correct initial and final state Ψ_i and Ψ_f are used and multiple-scattering processes are included. The final state in the one-step model is described as an inverse LEED (**l**ow-**e**nergy **e**lectron **d**iffraction) state, which takes into account the short mean free path of the photoexcited electrons. In a LEED process a beam of electrons with low energies and a velocity $\boldsymbol{v}$ is partly reflected at the surface of a solid, and partly it penetrates into the solid. To describe the photoemission experiment based on the LEED process, one has to neglect the reflected beam, reverse the direction of the incoming and penetrating electron beam and add an incoming photon [105].

The photocurrent in the one-step formalism can, therefore, be described by [105]:

$$(3.10) \qquad \omega_{f,i} \propto \boldsymbol{v} \cdot \sum_{occupied,i} (|\langle \Psi_f^L | H_{int} | \Psi_i \rangle|^2) \cdot \delta(E_f - E_i - h\nu),$$

where the final state $|\Psi_f\rangle$ is given by the wave function $\left|\Psi_f^L\right\rangle$ of the electron in the inverse LEED state in the solid.

The wave functions of the initial and final state are expanded in terms of two-dimensional Bloch waves $u_m(\boldsymbol{r}, \boldsymbol{k}_{\|,f}, E_{kin})$ to account for the two-dimensional character of the surface, with $\boldsymbol{r} = \boldsymbol{e}_x x + \boldsymbol{e}_y y + \boldsymbol{e}_z z$, the wave vector $\boldsymbol{k}_{\|,f}$ of the final state wave function, and the kinetic energy E_{kin} of the electron. An additional imaginary part of the potential in the Schrödinger equation characterizes the damping of the electrons in the solid. The amount of damping determines how far the initial or final state expand into the solid, given by the wave vector component $k_\perp = k_\perp^{(1)} + i k_\perp^{(2)}$ perpendicular to the surface. In general, if the imaginary part of $k_\perp$ is zero, no damping takes place and the wave function describes a propagating electron. If on the other hand the imaginary part is predominant, the damping is large leading to an evanescent wave. As a result, the final state in the inverse LEED formalism can be written as a combination of a

free electron wave in the vacuum and propagating as well as evanescent waves in the solid [105]:

$$(3.11) \qquad \left|\Psi_f^L\right\rangle \propto exp(i\boldsymbol{k}_{||,\boldsymbol{f}} \cdot \boldsymbol{r}_{||}) \sum_m t_m exp(ik_{\perp,m}z) u_m(\boldsymbol{r}, \boldsymbol{k}_{||,\boldsymbol{f}}, E_{kin}),$$

where $u_m(\boldsymbol{r}, \boldsymbol{k}_{||,\boldsymbol{f}}, E_{kin})$ are the Bloch wave functions, t_m is the transmission coefficient for the low-energy electron transmitted into the solid, $\boldsymbol{r}_{||} = \mathbf{e}_x x + \mathbf{e}_y y$, and the sum runs over the m different possible states.

The final state can for example be a combination of a free electron wave in the vacuum and a propagating Bloch wave with only small damping in the bulk. If the mean free path of the electron is small, on the other hand, the Bloch wave in the crystal is strongly damped. A more special case occurs for energies E_{kin} in the bulk band gap of the solid. The free electron is in that case combined with an evanescent wave, which is strongly damped inside the crystal, and the final state describes a surface state.

Similarly, also the initial state wave function can be expressed as a combination of bulk states, which propagate freely into the bulk, as well as surface states, which are strongly damped along the direction parallel to the surface normal into the vacuum as well as inside the solid.

3.5 Spin polarization detection in photoelectron spectroscopy

Spin-resolved photoelectron spectroscopy utilizes scattering processes which depend on the spin polarization of the electrons. Electrons with a certain spin direction are more likely to be scattered into the same direction, which introduces a commensurable scattering asymmetry A. The underlying principle that generates this asymmetry in the intensities of the scattered electrons is either spin-orbit coupling, which is employed in Mott spin detectors as well as detectors based on low-energy electron diffraction, or spin-exchange coupling, which is the relevant mechanism in spin-dependent scattering from magnetized targets [115]. The spin polarization $P(E_{bind}, \boldsymbol{k}_{||})$ can be determined from the measured asymmetry A, where:

$$(3.12) \qquad P(E_{bind}, \boldsymbol{k}_{||}) = \frac{1}{S_{eff}} \frac{I_\uparrow(E_{bind}, \boldsymbol{k}_{||}) - I_\downarrow(E_{bind}, \boldsymbol{k}_{||})}{I_\uparrow(E_{bind}, \boldsymbol{k}_{||}) + I_\downarrow(E_{bind}, \boldsymbol{k}_{||})},$$

with the Sherman function S_{eff} defined by $A = P(E_{bind}, \boldsymbol{k}_{||}) \cdot S_{eff}$ and the measured intensities $I_\uparrow(E_{bind}, \boldsymbol{k}_{||})$ and $I_\downarrow(E_{bind}, \boldsymbol{k}_{||})$ of electrons scattered to opposite directions in the detection plane [116, 117]. The Sherman function S_{eff} can be determined by scattering experiments with an electron beam of a known spin polarization. It

constitutes an approximate measure of the efficiency of the spin selection by the spin detector.

In order to investigate the spin polarization of the electronic states, three different types of spin detectors were employed within this work. Their basic functionality as well as the underlying physics of the spin dependent scattering processes will be shortly explained in the following.

Mott scattering

Mott scattering describes the elastic scattering of a spin polarized electron beam on a heavy element target. The cause of the resulting asymmetry in the scattering process is spin-orbit coupling between the electron and the nuclei of the target atoms. The electron, which is accelerated towards the target, perceives a current in its rest frame — the moving charged nucleus of the scattering center — and, therefore, a magnetic field $\mathbf{B}$ [111, 118]. The interaction $V_{LS} = \mu_e \cdot \mathbf{B}$ between the magnetic field $\mathbf{B}$ and the magnetic moment μ_e of the electron leads to a higher scattering amplitude along a particular direction for a spin polarized electron beam [118]. The resulting scattering asymmetry is proportional to the atomic number Z of the nucleus and the kinetic energy of the scattered electron. Therefore, photoelectrons are accelerated to about 15 keV or higher in standard Mott detectors and typically heavy elements as Au or Th are utilized as targets.

Spin-dependent electron diffraction from a magnetized target

Spin detection by **v**ery-**l**ow-**e**nergy **e**lectron **d**iffraction (VLEED) was first reported for spin polarized electron reflection from a magnetized Fe(001) target [119]. The reflectivity of an electron primarily depends on the **d**ensity **o**f **s**tates (DOS) of the target material and, therefore, on the energy of the electron. At energies, at which the target material exhibits a band gap and the DOS becomes zero, the reflectivity of the material is high, since electrons cannot be absorbed. For certain energies the reflectivity becomes strongly spin-dependent for a magnetized target, when the majority or minority-spin DOS is dominating and the probability to be absorbed is significantly higher for electrons with majority or minority spin, respectively [119, 120]. The disadvantage of a magnetized Fe(001) target is its quick degradation, which was soon overcome by the use of a pre-oxidized Fe(001)-p(1×1)O target [121]. Spin detection based on spin-exchange scattering is now a frequently used concept in spin detectors [83, 122, 123].

Spin-detection based on low-energy electron diffraction

The diffraction of low-energy electrons (LEED) on a non-magnetic target can also show a spin-dependence, when instead of the exchange mechanism, spin-orbit coupling

21

mediates the interaction between electron and solid [115]. The first spin-dependent LEED scattering experiment, establishing spin-dependent reflection, was performed on a W(001) target [82]. The LEED based spin filter, which was used in the experiments presented in this thesis, employs a Au passivated Ir(100) crystal as scattering target and allows to measure the in-plane spin projection to the y-axis (compare Fig. 3.2) [124, 125]. The target crystal is aligned in specular geometry and electrons are deflected by $90°$. The scattering asymmetry varies with the scattering energy E_{scatt} of the electrons resulting in a dependence of the spin sensitivity on scattering energy. By performing two subsequent measurements with different scattering energies information about the spin polarization of the photoelectrons is gained. For the Au/Ir(100) crystal the spin sensitivity is highest for scattering energies of $E_{scatt} = 10.25\,\mathrm{eV}$ and $E_{scatt} = 11.50\,\mathrm{eV}$ for spin-down and spin-up, respectively.

One advantage of the LEED based spin detection, as implemented in the detector setup employed in this work, is the capability to gain information about the spin polarization over a two-dimensional area, since the spatial information is conserved upon specular reflection of an electron beam [126, 127] making spin-resolved two-dimensional imaging possible.

3.6 Experimental setups

The photoelectron spectroscopy experiments were performed in **u**ltra **h**igh **v**acuum (UHV) to prevent the sample from contamination. The setups all consist of a minimum of three UHV-chambers, which are connected with each other by valves. The samples are introduced into a small chamber, generally termed load lock, where after venting a pressure of about 1×10^{-7} mbar can be reached in a rather short time frame of only a few hours. The sample can then be transferred into the adjoining preparation chamber, where sample preparation takes place at a base pressure below 5×10^{-10} mbar. An ion bombardment gun serves for cleaning the sample surface by sputtering with Ar^+-ions. With a filament, the sample can be heated up to $500 - 1500°C$ by electron bombardment. In some of the setups an additional heating stage for heating the sample to temperatures between room temperature and $T \approx 500°C$ was installed. The preparation chamber is usually equipped with a LEED experiment, which allows to monitor the surface quality of the sample, as well as with evaporators to introduce adatoms to the sample surface.

The photoemission experiment takes place in the analyzer chamber, with a base pressure below 5×10^{-10} mbar in all experimental setups. The sample can be placed on a manipulator, which allows movement of the sample within up to six degrees of freedom. All setups allow translational movement along x, y and z. In addition, the
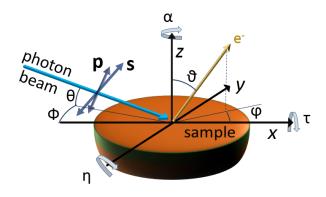
FIGURE 3.1. **Sample alignment with regard to incoming light beam and detector.** The x, y and z axis are fixed with respect to the analyzer and the experimental chamber. The x-axis is parallel to the analyzer entrance slit in all experiments presented throughout this work. The incoming light beam is incident at an azimuthal angle Φ and an angle Θ between incoming light beam and sample surface, the emission angles for an outgoing electron are ϑ with respect to the z-axis and φ in the $x-y$-plane. Sample rotation is defined by the angles α for rotation around the surface normal, τ for tilting with the rotational axis x and η for rotating around the y-axis. The arrows labeled with s and p indicate the polarization direction of a linear polarized light beam.

sample can be rotated around the azimuthal angle (α in Fig. 3.1), and tilted with the x–axis or the y–axis as rotational axis. In most setups, rotation is only possible along one axis, whereas some of the experimental setups employed here allow all three possible rotation directions. The analyzer chamber is equipped with at least one photon source as well as an electron analyzer. Emitted photoelectrons pass through the analyzer, which has an entrance slit of variable size, and are detected with the help of a multichannel plate installed behind the exit slit of the analyzer. The analyzer can be set to transition mode, often applied for XPS measurements, or angular mode, which allows to resolve the electrons emission angle and is, therefore, used for ARPES measurements. In addition, different pass energies can be utilized, which determine the energy window that is detected simultaneously. High pass energies increase the number of transmitted electrons but decrease the energy resolution of the experiment.

The principle geometry of the setup with regard to the sample surface is depicted in Fig. 3.1. The sample is oriented with the surface normal for an untilted sample along the z–axis. The incoming light (blue arrow) is incident at an azimuthal angle Φ and an angle Θ between sample surface and light beam. The incoming light excites electrons from the sample which can be detected by the electron analyzer if the emission angle ϑ at which they leave the surface is smaller than the maximum acceptance angle of the

analyzer.

The different setups in this work can be categorized in laboratory setups (the laboratory in Würzburg and at the Max Planck institute in Halle) and synchrotron setups (beamline i3 at Max-laboratories and beamlines BL 9A and BL 9B at the Hiroshima Synchrotron Radiation center). A laboratory setup often has the advantage of easy accessibility and is in many cases best suited for experiments, which need special adjustments in the experimental setup, a time-consuming optimization of the sample preparation or preliminary experiments for sample characterization. Synchrotron light sources on the other hand provide the opportunity to tune the photon energy as well as light polarization, which allows to adjust these parameters according to the experimental requirements. With synchrotron light sources a systematic analysis of photon energy and light polarization dependencies becomes possible.

The setups, which will be described in more detail below, differ in their specific qualifications, given by analyzer type, sample geometry, available light sources, and availability as well as type of a spin detector.

3.6.1   UHV laboratory at the university of Würzburg

In the laboratory in Würzburg the UHV setup is equipped with a chromatized He discharge lamp ($h\nu$(He I$_\alpha$) = 21.2 eV) (Gammadata) and a non-monochromatized x-ray gun (Specs) with $h\nu$(Al K$_\alpha$)= 1486.7 eV and $h\nu$(Mg K$_\alpha$)= 1286.6 eV. Light incidence is at $\Phi = 0°$ and $\Theta = 45°$ for the x-ray source and $\Phi = 180°$ and $\Theta = 45°$ for the He discharge lamp. The sample manipulator in the analyzer chamber allows translational movement along x, y and z and rotation around the x-axis. The manipulator can be cooled by a He flow cryostat and sample temperature during the experiments presented in this work was about T≈ 45 K.

The electron detector is a VG Scienta SES 200 hemispherical analyzer, which allows the detection of electrons up to an acceptance angle of $\pm 7°$. For all presented ARPES data sets the pass energy of the analyzer was set to 5 eV, for XPS measurements a pass energy of 150 eV was chosen. The energy resolution of the ARPES and XPS measurements performed employing this setup was determined to $\Delta E_{ARPES} \approx 10$ meV and $\Delta E_{XPS} \approx 1$ eV, respectively.

3.6.2   Max-laboratory in Lund, Sweden

The beamline i3, situated at the accelerator ring at Max III of Max-laboratories in Lund, is optimized for spin- and angle-resolved photoelectron spectroscopy. It is equipped with a VG Scienta R4000 hemispherical analyzer with an adjacent Mott-type spin-detector also fabricated by VG Scienta [80]. In order to mount the Mott spin-

detector, the standard multichannel plate detector of the R4000 analyzer is replaced by a smaller one (25 mm diameter) and positioned off center to make room for a circular aperture where the spin transfer lens is mounted. The Mott detector is operated at 25 keV and the target is made of Th with a Sherman function of $S_{eff} = 0.17$.

The synchrotron light at beamline i3 can be tuned in a range from 5 eV to 50 eV and between circular and linear p- and s-polarization. Sample, photon beam and analyzer are aligned in such a way that the light beam lies in the detection plane with $\Theta = 17°$ and $\Phi = 0°$. In all spin-integrated measurements the pass energy was set to 5 eV with an acceptance angle of $\pm 15°$. For spin-integrated measurements the energy resolution of the analyzer was about $\Delta E = 15$ meV. For the spin-resolved measurements the pass energy was set to 20 eV with an aperture of 2 mm for the spin transfer lens and the acceptance angle was set to $\pm 15°$, therefore, energy resolution was about $\Delta E \approx 50$ meV and angular resolution about $\Delta\theta \approx 3°$. The Mott detector allows the detection of the spin-component S_x along the x–axis as well as the out-of-plane component S_z. Sample movement is possible along all six degrees of freedom, though rotation around the azimuthal angle α as well as around the y–axis (η) are only possible in a rough manner by an *in-situ* screwdriver.

3.6.3 Hiroshima synchrotron radiation center, Japan

Beamlines 9A and 9B at the Hiroshima synchrotron radiation center (HiSOR) and subsequent end stations are optimized for high resolution angle-resolved photoemission experiments (BL 9A) and spin- and angle-resolved photoelectron spectroscopy (BL 9B, ESPRESSO end station). Both beamlines are equipped with a hemispherical analyzer R4000 (VG Scienta).

At BL 9A the synchrotron light is incident at an angle $\Theta = 40°$ and $\Phi = 0°$ and energies from 4 eV to 40 eV can be reached. In addition a Xe discharge lamp with $h\nu = 8.4$ eV is attached to the analyzer chamber. The sample manipulator in the analyzer chamber allows movement along the three translational directions, x, y and z as well as rotation around the x-axis. The data was acquired with a pass energy of 10 eV and an acceptance angle of $\pm 15°$ of the analyzer in angular mode. The energy resolution of all data measured at BL 9A is $\Delta E < 15$ meV. The sample was cooled by a He flow cryostat and the temperature during the measurements was approximately $T \approx 30$ K.

At BL 9B (ESPRESSO: Efficient SPin REsolved SpectroScopy Observation, [83]) the synchrotron light is incident at $\Theta = 40°$ and $\Phi = 0°$ and photon energies from 16 eV to 50 eV can be used. The chamber is additionally equipped with a He-discharge lamp. The end station has a VLEED based spin-detector adjacent to the electron analyzer, which allows detection of all three spin-components by target magnetization
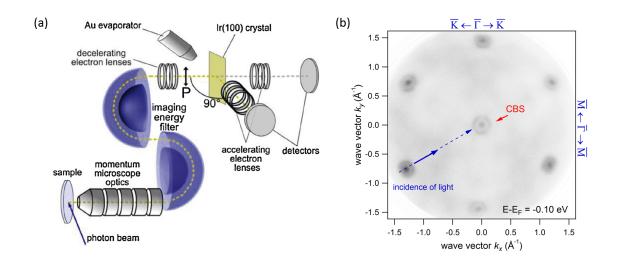
25

FIGURE 3.2. **Momentum microscopy** (a) shows a schematic of the momentum microscope as adopted from reference [125]. Electrons emitted from a sample are collected by the optical lens system and analyzed with respect to their spatial or $\boldsymbol{k}$-distribution. An adjacent spin-filter realized by a Au passivated Ir(100) crystal allows to measure the projected spin polarization along P (black arrow). (b) shows an example of a momentum map of BiTeI(0001) measured with the He I_α-line (21.2 eV) of a He discharge lamp at an energy $E - E_F = -0.10$ eV. The direction of light incidence is marked by a blue arrow, which points to the $\bar{\Gamma}$-point of the first Brillouin zone. The conduction band derived surface state CBS is marked by a red arrow.

along x,y,z. The detector target is a Fe(001)-p(1x1)-O film grown on Mg(001) and the Sherman function is $S_{eff} = 0.3$. The spin detector is mounted in the same manner as described for the Mott detector at beamline i3 in Lund. The sample manipulator allows translational movement of the sample along x, y, and z and rotation around the azimuth α, as well as rotation around the y-axis. The experiments were performed with a pass energy of 10 eV yielding a resolution at BL 9B of $\Delta E \approx 15$ meV for spin-integrated measurements and $\Delta E < 50$ meV and $\Delta \vartheta \approx 3°$ for spin-resolved measurements. The sample was cooled by He and the temperature was approximately T ≈ 20 K.

3.6.4   Max Planck institute of microstructure physics, Halle

Some of the experiments of this work, mainly shown in section 5, were performed at the Max Planck institute in Halle, employing a momentum-resolving photoemission microscope ($\boldsymbol{k}$-PEEM) [124], which was installed and operated under the direction of Prof. J. Kirschner. A schematic (adapted from [125]) of the momentum microscope is

depicted in Fig. 3.2 (a). All electrons which leave the sample surface in a photoemission experiment are collected by an accelerating field between the sample, which serves as cathode, and an anode lens. They are guided into the analyzing system by a complex lens system, which is described in detail in reference [124]. The $\boldsymbol{k}$-resolving PEEM allows to simultaneously measure the complete momentum half space above the sample. To correctly align the sample in the optical axis and with regard to the anode lens, the sample stage is movable by a hexapod manipulator, which allows to adjust the sample position along six degrees of freedom. The sample can be cooled down by a He flow cryostat to a minimum of 18 K [124]. The analyzing apparatus consists of two hemispherical analyzers (modified PHOIBOS 150, Specs GmbH), which minimizes the aberration characteristic for a single one of this type of analyzers [124].

A spin-filter, based on low-energy electron diffraction on a Au passivated Ir(100) target, is integrated in the analyzing system behind the energy filter. It allows to measure the projection of the photoelectron spin to one direction, namely parallel to the y-axis as indicated by the black arrow P in Fig. 3.2 (a).

The best resolution achieved in the setup is $\Delta E = 12$ meV and $\Delta k = 0.0049 \text{Å}^{-1}$ [124]. In the measurements shown in this work the resolution is $\Delta E \approx 20$ meV for spin-integrated measurements and $\Delta E \approx 80$ meV for the spin-resolved measurements.

A typical momentum-resolved image is displayed in Fig. 3.2 (b) using the example of BiTeI measured with the He I$_\alpha$-line of a He discharge lamp. Unlike standard ARPES systems, a single measurement with the momentum microscope allows to image the $\boldsymbol{k}_{||}$ dispersion at a particular binding energy. By varying the probed binding energy in the experiment, the complete band structure can be mapped. The center in Fig. 3.2 (b) is the $\bar{\Gamma}$-point and the circular structure around the $\bar{\Gamma}$-point stems from the Rashba-split conduction band surface state (CBS) of BiTeI. In addition, at higher wave vectors $\boldsymbol{k}_{||}$ along the $\bar{\Gamma}\bar{M}$-direction further structures are visible, which again stem from the Rashba-split surface state CBS of BiTeI at higher order $\bar{\Gamma}$-points. The image thus demonstrates the capability of the momentum microscope to simultaneously capture the complete $\boldsymbol{k}_{||}$-space including higher order Brillouin zones.

The available light sources at the momentum microscope in Halle are a non-monochromatized He discharge lamp (modified SPECS) which allows to use the He I$_\alpha$ line with $h\nu = 21.2$ eV, a Hg as well as a Ne discharge lamp solely used for real space resolving PEEM imaging, and a Ti:Sa Laser light source with tunable light polarization and a photon energy of 6 eV. Light incidence is at $\Theta = 22°$ and $\Phi = -30°$ for the He lamp, also indicated by the blue arrow in Fig. 3.2 (b) and $\Theta = 8°$ and $\Phi = 0°$ for the laser light source (compare also Fig. 3.1).

3.7 Sample Preparation

Due to the surface sensitivity of the methods used in this work, namely photoelectron spectroscopy, atomically clean and well ordered surfaces are essential to obtain high quality data. Based on their crystal structure the different samples can be classified into three groups: layered crystals, thin films and surface alloys. All of them were grown differently and their surfaces were prepared in different ways. In the following the various sample preparation methods will be described.

Layered crystals

Samples with a layered atomic structure, as for example Bi_2Te_3 and BiTeI, were prepared by cleaving in UHV at pressures below $1{\times}10^{-7}$ mbar. The atomic layers form repeating sequences, so called quintuple or triple layers for Bi_2Te_3 and BiTeI, respectively, which are bound between each other by Van-der-Waals forces. The interaction between the atomic layers within the quintuple or triple layers is significantly stronger. Therefore, cleaving will preferably occur between top atomic layers of two multilayer units and the preparation results in clean and well ordered surfaces.

The cleaving procedure was preferably performed with the help of adhesive tape, which is fixed to the sample surface, and which, by removal inside the vacuum, removes the topmost multilayer units from the sample. In some cases, the samples were prepared by utilizing a cleaving post, which was attached to the sample surface with two component Ag-based glue. The cleaving post can be pushed off the sample inside the vacuum and likewise removes the top multilayer units from the sample. Both methods result in a comparable quality of the photoemission data.

Thin film samples

Thin films of the layered material Bi_2Te_2Se were grown on Si(111) using molecular beam epitaxy (MBE) in the group of Professor Molenkamp at the university of Würzburg. The film thickness of the samples presented in this work is about 70 nm. In order to protect the samples from surface contamination during transport through air from the growth chamber to the surface analyzing setups, they were covered by an amorphous Se film with a thickness of approximately 200 nm. Prior to the photoemission experiments, the Se cap was removed by heating the sample up to 160°C at pressures below 1×10^{-8} mbar. To verify the successful preparation, XPS was performed before and after the decapping procedure. An example for such an XPS measurement of the Se 3d core levels is shown in Fig. 3.3 (a), where the photoemission intensity of the amorphous Se of the cap is shown in black and the signal from the successfully prepared film is shown in blue. Whereas the Se 3d binding energy lies at $E_B = 55.8(2)$ eV (black line) for the amorphous film, the signal is shifted to smaller
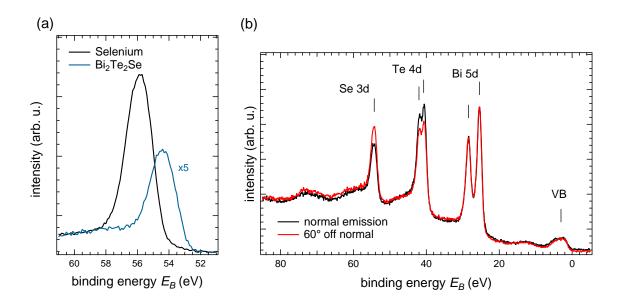
FIGURE 3.3. **Se-capped topological insulator films** (a) XPS measurement of the Se 3d core level before (black line) and after (blue line) the decapping procedure revealing a shift of 1.5 eV between the amorphous Se-cap and the Bi_2Te_2Se sample. (b) shows a comparison of XPS measurements at normal emission (black line) and at an emission angle of 60° of Bi_2Te_2Se at binding energies below 100 eV. The Se 3d, Te 4d and Bi 5d as well as the valence band (VB) signals are distinguishable. At 60° the Se 3d intensity is enhanced, while the Te 4d intensity is reduced.

binding energies by $\Delta E = 1.5$ eV after the removal of the Se-cap (blue line). The different binding energies are a signature of the different chemical environment of the Se in the amorphous cap and the Se in Bi_2Te_2Se. The core level peak positions can, therefore, already provide evidence for the successful removal of the Se-cap.

Furthermore, XPS can be employed to investigate possible changes in the surface stoichiometry induced by the thermal decapping process by exploiting the limited photoelectron escape depth. Changing the emission angle from normal emission to 60° by sample rotation, as done in the measurements shown in Fig. 3.3 (b), results in a higher surface sensitivity, which permits a depth dependent analysis of the stoichiometry. The spectra show the Se 3d signal at a binding energy of 54.3 eV, Te 4d at 42.0 eV and 40.7 eV and the Bi 5d core-levels at 25.4 eV and 28.5 eV for both, the measurement taken at normal emission (black line) and at 60° (red line). The photoemission intensities of the Se and Te signal change between the two measurements, namely, the Se 3d signal is enhanced, whereas the Te 4d signal is reduced at higher emission angle. The Bi 5d photoemission intensity, on the other hand, remains unchanged. Therefore, one can conclude that the relative amount of Se is higher at the surface

compared to the bulk, while at the same time the amount of Te is reduced. A likely explanation is a substitution of Te by Se atoms in the topmost layer as discussed in reference [36]. Therefore, even though the preparation of capped thin-film samples by heating leads to a successful removal of the amorphous Se on the sample, changes of the stoichiometry at the surface could not be avoided.

Surface alloys

The preparation of BiAg$_2$ and PbAg$_2$ on Ag(111) was carried out by repeated cycles of Ar$^+$-ion sputtering and annealing of Ag(111) with an Ar pressure of $5 \cdot 10^{-5}$ mbar and an annealing temperature of roughly 800°C. To prepare the surface alloys 1/3 of a monolayer of either Bi or Pb was evaporated onto the clean Ag(111) crystal. In case of the preparation of BiAg$_2$ the sample was annealed to roughly 300°C after deposition of Bi, whereas the preparation of PbAg$_2$ turned out to work best, when the Ag(111) crystal was heated to approximately 300°C directly before evaporation of Pb and left to cool down during the evaporation. Both surface alloys form a $(\sqrt{3} \times \sqrt{3})R30°$-reconstruction, accessible by a LEED experiment. LEED, therefore, served as a verification of the formation of the surface alloys.

3.8 Data processing

ARPES

The analyzing systems allow to detect the photocurrent $I(E_{kin}, \vartheta, \varphi)$ as a function of the kinetic energy E_{kin} of the photoelectron and its emission angle ϑ and φ. A single measurement with a conventional hemispherical analyzer yields information about the kinetic energy E_{kin} and the emission angle ϑ, whereas the sample has to be rotated around the axis parallel to the analyzer entrance slit in order to obtain the photocurrent in dependence of the angle φ. The momentum microscope, on the other hand, allows the simultaneous measurement of the angles φ and ϑ, whereas the probed binding energy is tuned via the lens system.

In order to obtain the photocurrent in dependence of the binding energy with respect to the Fermi level $E - E_F$ and the wave vector $\boldsymbol{k}_{||}$ a few simple data processing steps have to be performed. All presented ARPES data from standard hemispherical analyzers were measured with a straight analyzer entrance slit, which results in a curved image of the electrons at the multichannel plate. In order to correct this experimentally caused distortion, a reference data set is fitted by a Fermi-Dirac distribution at each emission angle ϑ. An ideal reference measurement is performed with a polycrystalline sample, which exhibits no band dispersion, and under the same

experimental conditions as the actual experiment. The position of the Fermi edge at each emission angle allows to deduce and correct the curvature. In the same data evaluation step the energy is set to zero at the Fermi level, yielding an energy axis $E - E_F$. The translation from emission angles to wave vector is done via equation 3.4.

In order to calibrate the momentum in the data measured at the momentum microscope in Halle, the maximum wave vector $\boldsymbol{k}_{\parallel}^{max}$ can be deduced from the vacuum cut-off in the experimental data. Its value is determined by the dispersion relation of a free electron $\boldsymbol{k}_{\parallel}^{max} = \beta\sqrt{E}$ with $\beta = \sqrt{2m_e/\hbar^2}$ for a given energy E.

SARPES

Spin resolved energy distribution curves from all single channel spin detectors are evaluated according to equation 3.12 from the measured intensities of the electrons scattered to the left (I_L) or right (I_R) hand, respectively.

The data evaluation of spin-resolved momentum maps acquired with the momentum microscope is outlined in detail in references [124, 128]. From two data sets measured with two different spin sensitivities S_h and S_l the spin polarization P can be calculated by [124]:

$$(3.13) \qquad P(x,y) = \frac{I_l(x,y)/R_l - I_h(x,y)/R_h}{S_l \cdot I_h(x,y)/R_h - S_h \cdot I_l(x,y)/R_l},$$

and the spin-integrated intensity $I_0(x,y)$ is given by [124]:

$$(3.14) \qquad I_0(x,y) = \frac{S_l \cdot I_h(x,y)/R_h - S_h \cdot I_l(x,y)/R_l}{S_l - S_h}.$$

Here x and y are the coordinates of the image, which correspond to k_x and k_y in case of a momentum-resolved PEEM image. $I_{l,h}(x,y)/R_{l,h}$ is the measured intensity I normalized to the reflectivity R for the high (h) or low (l) scattering energy E_{scatt}. In the presented experiments $E_{scatt,l} = 10.25$ eV and $E_{scatt,h} = 11.50$ eV were used. The spin sensitivities $S_h = 0.6$ and $S_l = -0.6$ as well as the reflectivities $R_h = 2.3\%$ and $R_l = 1.3\%$ were obtained prior to our experiments as described in reference [124].

General data evaluation

In order to quantitatively evaluate the measured photoemission intensities, **e**nergy **d**istribution **c**urves (EDC), which show the intensity distribution at one particular wave vector ($I(\boldsymbol{k}_{\parallel} = const., E_{bind})$), or **m**omentum **d**istribution **c**urves (MDC), which allow to evaluate the intensity distribution at a constant energy ($I(\boldsymbol{k}_{\parallel}, E_{bind} = const.)$), can be extracted from the data. All quantitative analyses from MDCs or EDCs in this work were done by fitting Voigt line profiles to the intensity maxima, allowing a determination of intensities from peak areas as well as peak positions and widths. The background intensity for the fits was approximated to be linear.

MATERIAL PROPERTIES

Investigating the spin polarization of electronic states and effects in the spin polarization that arise during the photoemission process is the main focus of this work. To this end, it is imperative to find materials with a strong intrinsic spin polarization in their electronic structure. An intrinsic spin polarization does for example emerge as a result of the Rashba effect at the surface of noble metals [50, 129] as well as in surface alloys, where the spin-splittings have been found to be particularly large [60, 62]. Large Rashba-type spin-splittings can also occur in materials with a broken inversion symmetry in their crystal structure. This is for example the case in BiTeI, where large splittings appear in the bulk and surface band structure [64]. A different material class which shows a spin polarized electronic structure are topological insulators. Prominent examples are Bi_2Se_3 and related materials, which exhibit topological surface states as a result of the non-trivial bulk band structure, where the order between p_z-like bands of Bi and Se is inverted, owing to strong spin-orbit coupling [8].

The experiments in this work address the spin polarized surface electronic structure of different material types. In particular layered topological insulators, in this case Bi_2Te_3 and Bi_2Te_2Se, layered polar semiconductors with giant-Rashba splitting, represented by BiTeI, and the surface alloys $BiAg_2/Ag(111)$ and $PbAg_2/Ag(111)$ were investigated. This chapter presents an introduction to the electronic structure of these materials. It concentrates on important details that allow the reader to follow the subsequent discussions, however, it doesn't aim at a complete and elaborate summary of all properties known so far. In particular, the crystal structure of each material will be presented and the electronic bands which will be the focus of the following chapters are introduced. Finally, their advantage as model systems for the investigation of the photoelectron spin polarization is shortly discussed.

4.1 Layered topological insulators

Bi_2Te_3 as well as Bi_2Te_2Se belong to the group V-VI chalcogenides, which have a rhombohedral crystal structure as depicted in Fig. 4.1 (a). The crystal is symmetric under threefold rotation around the trigonal axis (z) and has a mirror-plane, which lies parallel to the $\bar{\Gamma}\bar{M}$-direction, in other words, the crystal space group is $R3\bar{m}$ [8, 130]. For the [111]-surface the symmetry is reduced to C_{3v}. Along the z-axis the crystal has a layered structure with a repeating sequence of group VI(i) - V - VI(ii) - V - VI(i) atomic layers, where the group V atom is Bi and VI(i) represents Te, whereas VI(ii) stands for either Te or Se for Bi_2Te_3 and Bi_2Te_2Se, respectively. Two subsequent quintuple layers are coupled by Van-der-Waals forces, which are much weaker than the coupling within the quintuple layers [8, 130]. The data presented in this work was acquired on Bi_2Te_2Se samples, grown by molecular beam epitaxy on a Si(111) crystal, whereas the Bi_2Te_3 samples are single crystals, grown by a modified Bridgman method [131].

The band structures measured along $\bar{\Gamma}\bar{K}$ of both materials are displayed in Fig. 4.1 (b) and (c). The lower panels show the dispersion for $Bi_2Te_2Se(0001)$ in (b) and $Bi_2Te_3(0001)$ in (c), the upper panels their respective Fermi surfaces. The light source was He I$_\alpha$ with $h\nu = 21.2\,\text{eV}$ in (b) and a synchrotron light source with 21 eV in (c).

For Bi_2Te_2Se two features can be clearly distinguished. The topological surface state (TSS) is emphasized by dashed lines that serve as guides to the eyes. The second feature, which lies below approximately $E - E_F = -0.3\,\text{eV}$, can be assigned to the bulk valence band (BVB). The group velocity of the topological surface state, which can be determined from its slope, is $v_G = (1/\hbar) \cdot (\partial E/\partial k) = 4.4(8) \times 10^5$ m/s. This is consistent with the group velocity of $v_G = 4.2(4) \times 10^5$ m/s determined in proximity of the Dirac point in an earlier study [133]. At the Dirac point the photoemission intensity is enhanced and the topological surface state and bulk conduction band overlap. Therefore, an exact determination of the energetic position of the Dirac point is not possible. From linear extrapolation it can be deduced to approximately $E - E_F \approx -0.35$ eV.

At close examination a third structure, which can be attributed to the bulk conduction band (BCB), is visible at the Fermi level. It should be noted that the electronic structure shows a significant aging due to the adsorption of residual gases [36, 134–137]. Therefore, the electronic states shift to higher binding energies with time after sample preparation and the bulk conduction band can only be observed after some time.

The Fermi surface in the upper panel of (b) shows enhanced intensity at the $\bar{\Gamma}$-point, which stems from the bulk conduction band. The topological surface state lies at higher wave vectors and exhibits a hexagonal deformation highlighted by the dashed black line. The vertices of the hexagonal structure point along $\bar{\Gamma}\bar{M}$, whereas the edges are oriented towards $\bar{\Gamma}\bar{K}$.
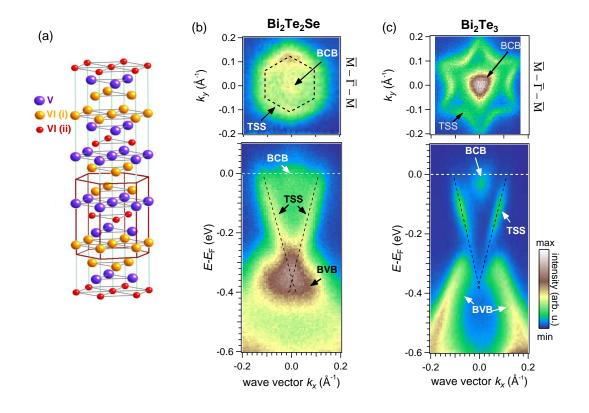
FIGURE 4.1. **Topological insulators Bi_2Te_2Se and Bi_2Te_3.** In (a) the rhombohedral crystal structure of group V-VI topological insulators is displayed. The crystal is built of quintuple layers which consist of alternating atomic layers of group V and group VI elements (graphic adapted from [132]). (b) and (c) show the measured band structures of $Bi_2Te_2Se(0001)$ and $Bi_2Te_3(0001)$, respectively. The experiments were performed with $h\nu = 21.2$ eV in (a) and 21.0 eV in (b). The upper panels show the Fermi surfaces. Black dashed lines serve as guides to the eyes for the topological surface states (TSS) of both materials. Additionally, the bulk conduction bands (BCB), and bulk valence bands (BVB) are labeled.

The band structure of Bi_2Te_3 is in many aspects quite similar to the one of Bi_2Te_2Se. In the ARPES measurement along $\bar{\Gamma}\bar{K}$ shown in Fig. 4.1 (c), analogue to (b) three states can be distinguished: the topological surface state (TSS) with a nearly linear dispersion, the bulk valence band (BVB) below $E - E_F = -0.25$ eV and the bulk conduction band (BCB) at the Fermi energy. The group velocity of the topological surface state at the Fermi level is $v_G = 8.3(8) \times 10^4$ m/s, which is lower than the group velocity in Bi_2Te_2Se. One apparent difference is the intensity at the Dirac point, which goes to zero for Bi_2Te_3, whereas it is enhanced in Bi_2Te_2Se. Another deviation can be found in the line widths of the states. In Bi_2Te_3 the line width of the topological surface state is almost three times smaller than in Bi_2Te_2Se, probably due to the differences in sample preparation. Whereas Bi_2Te_3 is prepared by *in-situ* cleaving, the Bi_2Te_2Se film is prepared by a thermal treatment that removes a protective Se-cap as discussed in chapter 3. This treatment might result in a larger disorder at the surface, in particular, a higher number of stepedges and the integration of additional Se atoms.

In the Fermi surface in the upper panel of Fig. 4.1 (c) the bulk conduction band as well as the topological surface state show distinct and intense features. The conduction band forms a triangular intensity at the $\bar{\Gamma}$-point, whereas the star-like intensity around the $\bar{\Gamma}$-point stems from the topological surface state. Compared to Bi_2Te_2Se the hexagonal deformation is much more pronounced, resulting in the distinct star-like form with the tips of the star pointing along $\bar{\Gamma}\bar{M}$. The deviating magnitude of the anisotropy is very likely due to the different stoichiometries of the two materials and the difference in their intrinsic doping, which shifts the Fermi energy with respect to the Dirac point. Whereas the warping has been repeatedly shown to be very pronounced in Bi_2Te_3 [76, 130], a smaller but significant warping effect was observed in Bi_2Te_2Se [138, 139] and Bi_2Se_3 [140]. Thus, the hexagonal anisotropy of the topological surface states of both materials fits well to previous observations.

4.2 Giant-Rashba splitting in BiTeI

BiTeI has a trigonal non-centrosymmetric layered structure with space group $P3m1$. It exhibits a mirror plane parallel to the crystal direction $\bar{\Gamma}\bar{M}$. Three atomic layers with the sequence Te – Bi – I form one triple layer bound by covalent (Bi – Te) and ionic (Bi – I) bonds, which induces a polarity along the stacking direction z [65]. Between the triple layers the coupling is of Van-der-Waals type and, therefore, considerably weaker than the coupling within a triple layer. The terminating atomic layer consists of either Te or I due to domains that are caused by stacking faults in the crystal bulk as illustrated in Fig. 4.2 (c). In all investigated crystals both possible surface terminations
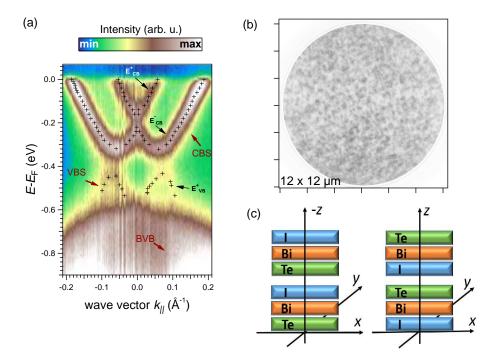
FIGURE 4.2. **Giant-Rashba-split surface electronic structure of BiTeI.** (a) shows the electronic structure of BiTeI(0001) measured with $hv = 24.0$ eV [141]. Black markers indicate intensity maxima of the upper branch E_{CB}^+ and lower branch E_{CB}^- of the conduction band surface state (CBS) as well as the upper branch E_{VB}^+ of the valence band surface state (VBS). (b) shows a PEEM data set of the cleaved BiTeI(0001) surface with gray and white indicating areas of different surface terminations Te or I, which are a result of stacking faults as schematically shown in (c).

coexisted on the same sample surface. In Fig. 4.2 (b) a PEEM measurement of a cleaved BiTeI surface, which is sensible to the materials work function, is shown. The darker and brighter areas correspond to the different work functions of the two possible surface terminations [142]. The terraces are distributed evenly between Te and I surface layers and have an approximate terrace width of 50 − 150 nm as shown in previous STM experiments [143]. The BiTeI samples investigated in this work were grown by a modified Bridgman method as described in [131].

Due to the broken inversion symmetry in the crystal bulk, the band structure of BiTeI exhibits a Rashba-type spin-splitting in its bulk as well as its surface electronic structure [144, 145]. In Fig. 4.2 (a) the surface states, which develop from the valence and conduction band, are labeled valence band state (VBS) and conduction band state (CBS), respectively, and are highlighted with black markers that are positioned at the intensity maxima as obtained from momentum distribution curves. The spin-splitting in the band structure of BiTeI is among the largest Rashba-type spin-splittings

observed so far. The upper and lower branch E_{CB}^+ and E_{CB}^- of the conduction band state are thus well separated in energy and momentum. The same can be said for the valence band state, where only the upper branch E_{VB}^+ can be distinguished, whereas the lower branch E_{VB}^- is not visible, due to the rather high intensity of bulk valence band (BVB) states. A quantitative evaluation of the Rashba-splitting yielded $\alpha_R^{CB} = 3.85\,\mathrm{eV\text{\AA}}^{-1}$ for the conduction band state [64].

The conduction band state and valence band state have been shown to be located on the Te and I terminated surfaces, respectively [143]. As a consequence the two states behave differently in terms of aging, which leads to by far stronger energy shifts on a similar timescale for the valence band state, due to the higher reactivity of the I-surface [66, 143]. It is also important to keep in mind that the reversed stacking order results in a reversal of the intrinsic electric field with respect to the surface. This intrinsic electric field originates from the polarity of the crystal and is the driving force for the giant-Rashba splitting. Taking into account the reversed z-axis due to the inverted crystal stacking order, we were able to show in a previous work that the sign of the Rashba parameter is opposite between valence band top and conduction band bottom [37] as suggested in a theoretical evaluation of the origin of the Rashba-splitting in BiTeI [65].

4.3 Surface alloys

BiAg$_2$ and PbAg$_2$ are examples for surface alloys which form on noble metal surfaces after deposition of one third of a monolayer of Bi or Pb and subsequent annealing. In the surface layer every third atom is replaced by an adatom as illustrated in the schematic in Fig. 4.3 (a). The surface alloys form $(\sqrt{3} \times \sqrt{3})R30°$ reconstructions, which implies that the surface unit cell is rotated by $30°$ and increased by a factor of $\sqrt{3}$ compared to the Ag(111) substrate [146]. In momentum space the $\bar{\Gamma}\bar{K}$-direction of the surface alloy coincidences with the $\bar{\Gamma}\bar{M}$-direction of the Ag(111) substrate and the size of the surface Brillouin zone is reduced. The surface alloys exhibit a mirror plane, which is oriented parallel to the $\bar{\Gamma}\bar{K}$-direction [147]. The crystal directions given throughout this work correspond to the orientation of the surface alloys.

The substitution of the substrate atoms by heavy element atoms is limited to the surface atomic layer, therefore, the system can be regarded as nearly two-dimensional. Due to a size mismatch between adatoms and the Ag atoms, an additional out-of-plane relaxation Δz is present. It has been discussed in previous works that this out-of-plane relaxation might be one of the factors that lead to the large sized Rashba-splittings in surface alloys [61]. Moreover, it has a strong influence on the energetic position of the surface states as deduced from band structure calculations [61, 62].
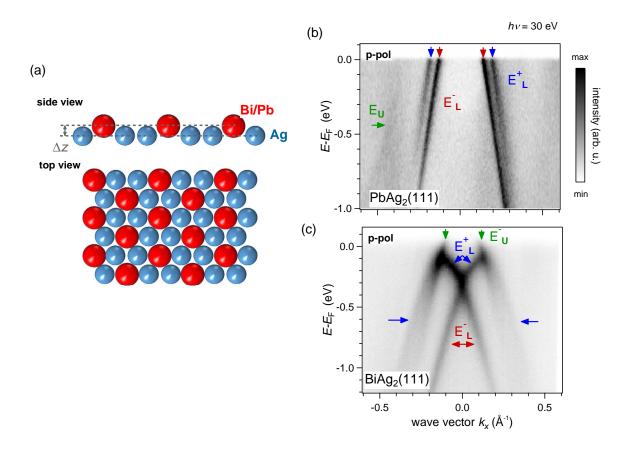
FIGURE 4.3. **Electronic structure of the surface alloys PbAg$_2$/Ag(111) and BiAg$_2$/Ag(111).** (a) shows a schematic of the atomic structure of the surface alloys. The upper part shows a side view illustrating the out-of-plane relaxation Δz, which is a result of the size mismatch between Ag atoms (blue spheres) and adatoms Bi or Pb (red spheres). The lower panel shows the top view of the surface alloys. (b) and (c) display ARPES intensity plots of the PbAg$_2$/Ag(111) and the BiAg$_2$/Ag(111) band structure, respectively. The different bands are labeled with $E_{L/U}^{+/-}$ for the (+) and (-) branch of the upper (U) and lower (L) state and marked with colored arrows. The data was acquired at beamline BL 9A at HiSOR (b) and at beamline i3 at Max-laboratories (c) with a photon energy of $h\nu = 30\,\text{eV}$ and p-polarized light.

Fig. 4.3 shows ARPES measurements of the electronic structure of PbAg$_2$/Ag(111) in (b) and BiAg$_2$/Ag(111) in (c). The light source in both cases was tuned to p-polarized light with a photon energy of $h\nu = 30$ eV. The surface alloys exhibit two Rashba-split bands. The band that lies lower in energy is termed E_L (L for lower) and is fully occupied in BiAg$_2$, whereas its maxima lie above the Fermi level in the case of PbAg$_2$. In Fig. 4.3 (b) and (c) this mainly occupied state is labeled E_L^+ and E_L^- for the upper and lower Rashba branch, respectively. The two branches are additionally marked by blue and red arrows.

A second surface state can be observed at higher energies $E - E_F$ and is, therefore, labeled E_U (U for upper) for both surface alloys. It lies at wave vectors $|k_x| > 0.3\,\text{Å}^{-1}$ in the band structure of PbAg$_2$ in Fig. 4.3 (b) and is almost indistinguishable. Furthermore, in the occupied part of the band structure of PbAg$_2$ the states $E_U^{\pm}$ are degenerate. In case of BiAg$_2$ in Fig 4.3 (c) the lower branch E_U^- of the upper state crosses the occupied surface state E_L. The surface state E_U is marked by green arrows in Fig. 4.3.

The occupied surface state E_L has been predicted to consist of mainly sp_z-orbitals in early works, whereas the upper surface state E_U was assumed to have predominantly $p_{x,y}$ character [61, 148]. The actual orbital composition turns out to be more complicated as will be discussed within this work.

The magnitude of the Rashba-splitting differs significantly between BiAg$_2$ and PbAg$_2$. Whereas the occupied surface state of PbAg$_2$ exhibits a Rashba-parameter of $\alpha_{R,Pb} = 1.42\,\text{eVÅ}^{-1}$ [148], the Rashba-parameter of $\alpha_{R,Bi}$ of the equivalent surface state of BiAg$_2$ is $\alpha_{R,Bi} = 3.05\,\text{eVÅ}^{-1}$ [60, 149] and is thus approximately two times larger.

Discussion

The materials investigated in this work have one common aspect, they all comprise of heavy elements, which introduce a large spin-orbit coupling (SOC) to the system. The resulting characteristics in the band structure are either topologically non-trivial surface states (TSS), as in Bi$_2$Te$_3$(0001) and Bi$_2$Te$_2$Se films, or the emergence of large Rashba-type spin-splittings (RSS) in the electronic structure, as observed for BiTeI and the surface alloys BiAg$_2$/Ag(111) and PbAg$_2$/Ag(111). In both cases a large spin polarization of the surface states can be expected. For the materials introduced above, the spin polarized states are well separated in energy and momentum — an ideal prerequisite for the investigation of the spin polarization, which is the central subject in this work. They are thus ideal model systems to understand the intricate spin polarization effects in the photoemission process.

An ideal surface state is two-dimensional and independent of the bulk of the material. In case of topological insulators, though, the band inversion leading to the

topologically nontrivial nature is a bulk property. More precisely, the bulk topological invariant ν_0 is related to the number of gapless edge states, a relation which is often termed bulk-boundary correspondence [7, 69]. Moreover, it has been shown for Bi_2Se_3 that the topological surface states on both sides of a thin film overlap up to a film thickness of six quintuple layers, indicating a considerable expansion of the surface states into the bulk [150]. Similarly for BiTeI the surface states develop from the bulk valence and conduction band and inherit their large spin-splittings [65, 145]. Thus, both types of materials are influenced by bulk properties. In addition, the layered structure of Bi_2Te_3, Bi_2Te_2Se, and BiTeI introduces a complicated orbital composition that differs between atomic layers [151]. The surface alloys, on the other hand, can be considered nearly two-dimensional and are thus model cases for a two-dimensional surface state, where the bulk properties play a secondary role, only.

The combination of the different types of materials, with topological as well as Rashba-type surface states, and layered as well as surface confined structures, allow to develop a comprehensive picture of the spin polarization effects in SOC materials.

SPIN AND ORBITAL TEXTURE GENERATED BY STRONG SPIN-ORBIT COUPLING

The surface states of topological insulators as well as of materials which show Rashba-type splittings in their surface electronic structure are often described in a simplified picture, where the surface state exhibits a single chiral spin-texture. This description is incomplete, as the wave functions of the states are generally composed of different orbital components. Due to strong spin-orbit coupling, the orbital and spin degree of freedom are not independent from each other, but the orbital parts of the wave function are coupled to different spin structures. Therefore, in order to understand the structure of the wave function as well as its inherent complex spin-texture it is helpful to first decipher the orbital composition.

For a surface state composed of p_x-, p_y- and p_z-orbitals, the initial state wave function $|\Psi_i\rangle$ of the states can in a simple way be expressed as:

$$(5.1) \qquad |\Psi_i\rangle = c_1 |p_z\rangle |\chi_1\rangle + c_2 |p_r\rangle |\chi_2\rangle + c_3 |p_t\rangle |\chi_3\rangle,$$

where $|p_r\rangle$ and $|p_t\rangle$ are p-orbitals aligned radially or tangentially to the state, respectively, and $|p_z\rangle$ describes the out-of-plane orbitals. The orbital structures are coupled to different spin structures $|\chi_{1-3}\rangle$ [29, 152] and the coefficients c_{1-3} quantify the relative contribution of the different orbital parts to the overall wave function. The alignment of the different p-orbitals is illustrated in Fig. 5.1, where the orbitals are depicted as gray lobes. In (a), (b) and (c) the p_y-orbital, aligned along the y-axis, the p_x-orbital aligned along x and the p_z-orbital, which lies parallel to the surface normal are shown. The tangential $|p_t\rangle$, radial $|p_r\rangle$ and out-of-plane $|p_z\rangle$ structure of
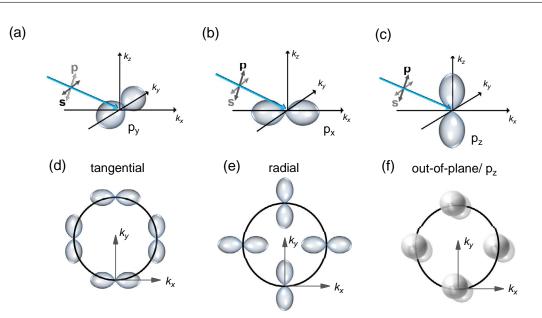
FIGURE 5.1. **Schematic of dipole selection rules.** (a) illustrates, how the p_y-orbital can be probed by s-polarized light, whereas the p_x- (b), and p_z-orbitals (c) can be addressed by p-polarized light. (d)-(f) shows a schematic presentation of the orbital composition of electronic bands at a constant binding energy. The band dispersion is illustrated by a simple circle and orbitals are depicted as blue lobes. Here, the orbital composition is composed of p-orbitals which are oriented tangential (d) or radial (e) to the band as well as of p_z-orbitals (f).

the orbitals is illustrated in (d) to (e), respectively. Black circles are simple schematics, which represent the surface state dispersion at a constant binding energy.

It has been demonstrated for instance for the topological insulator $Bi_2Se_3(0001)$ that photoelectron spectroscopy can serve as a probe of the orbital composition, when linear p- or s-polarized light is used [153]. The light polarization is termed s, if the polarization direction of the vector field $\boldsymbol{A}$ of the incoming radiation, given by the unit vector $\hat{\boldsymbol{\epsilon}}$, is oriented perpendicular to the plane of incidence given by the direction of the incoming light beam (blue arrow in Fig. 5.1) and the surface normal (k_z-axis). For p-polarization the polarization direction of $\boldsymbol{A}$ lies in the plane of incidence but perpendicular to the direction of the light beam as shown in the schematic in Fig. 5.1 (a)-(c). The schematic illustrates, how for light incidence in the $x - z$-plane s-polarized light allows to probe the p_y-orbital, only (Fig. 5.1(a)), whereas with p-polarized light electrons from p_x- as well as p_z-orbitals can be excited (Fig. 5.1(b) and (c)). This can be understood, when considering the photoemission matrix element $D = \langle \Psi_f | \boldsymbol{A} \cdot \boldsymbol{p} | \Psi_{i,\sigma} \rangle \propto \langle \Psi_f | \hat{\boldsymbol{\epsilon}} \cdot \boldsymbol{r} | \Psi_{i,\sigma} \rangle = \int d^3 r \Psi_f^* \hat{\boldsymbol{\epsilon}} \cdot \boldsymbol{r} \Psi_{i,\sigma}$, with the initial and final state wave functions $|\Psi_{i,\sigma}\rangle$ and $|\Psi_f\rangle$, the momentum operator $\boldsymbol{p}$ and $\boldsymbol{r} = (x, y, z)$. For the least complicated case of an isotropic or mirror symmetric crystal, where the detection

plane lies in a mirror plane, the photoemission intensity is non-zero only, when the integrand of the overlap integral is an overall even function with respect to the mirror plane. The final state must be an even function [108], therefore, an initial state with either even or odd symmetry with respect to the mirror plane yields a non-zero photocurrent, if the operator $\boldsymbol{A} \cdot \boldsymbol{p}$ has even or odd symmetry, respectively. Concretely, for p-polarized light $\boldsymbol{A} \cdot \boldsymbol{p}$ has even symmetry with respect to the detection plane and allows to probe even, that is p_x- and p_z-orbitals, whereas for s-polarized light $\boldsymbol{A} \cdot \boldsymbol{p}$ has odd symmetry and can only excite electrons from p_y-orbitals.

A variety of works addresses the spin-orbital texture in $Bi_2Se_3(0001)$. Using photo-electron spectroscopy, the orbital texture of the topological surface state of $Bi_2Se_3(0001)$ has been shown to consist of a combination of p_z-orbitals and radially and tangentially aligned in-plane p-orbitals, where the orbital wave function of the upper part of the Dirac cone contains mainly tangentially aligned in-plane orbitals, whereas the lower part of the Dirac cone is constructed of mainly radially aligned in-plane orbitals [153]. The same method was employed to analyze the spin-orbital texture of the topological surface state of $Bi_2Se_3(0001)$, demonstrating that spin structures of opposite chirality are coupled to different orbital parts of the wave function [154]. Similar investigations on different material classes or even different topological insulators, however, remain scarce up to now. It is, therefore, of much interest to disentangle the spin-orbital texture in a variety of materials to gain a deeper understanding of the orbital structure in different materials and the relation between orbital and spin degree of freedom. What role does for example topology play for the spin character of an electronic state and is a complex spin-texture as found in the surface electronic structure of $Bi_2Se_3(0001)$ specific for this material class or rather a general property, inherent to all materials which exhibit strong spin-orbit coupling?

This chapter is dedicated to gaining a broader understanding of the intricate interplay between the spin and orbital degree of freedom and the associated role of topology as well as spin-orbit coupling. In the first part a thorough analysis of the orbital texture in the topological surface state of $Bi_2Te_2Se(0001)$ as well as in the Rashba-type surface states of BiTeI(0001), $PbAg_2$/Ag(111)and $BiAg_2$/Ag(111) is presented. The second part of this chapter addresses the spin-texture of the materials and gives insight into the coupling between spin and orbitals.

5.1 Orbital composition

Fig. 5.2 (a) and (b) show constant energy maps of the band structure of Bi_2Te_2Se at $E - E_F = -50$ meV. The measurement was performed at the momentum microscope
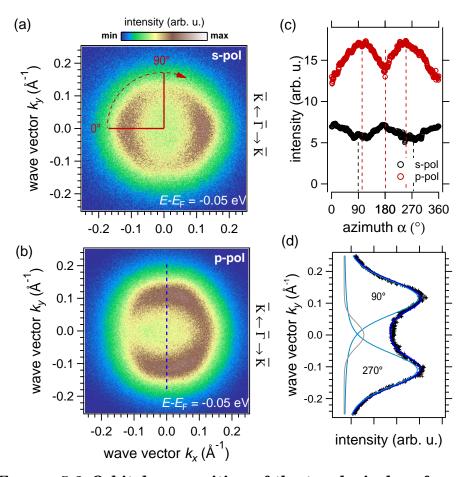
FIGURE 5.2. **Orbital composition of the topological surface state of
Bi$_2$Te$_2$Se films.** (a) and (b) show photoemission intensity plots at a
constant energy $E - E_F = -0.05$ eV that were measured with linearly s-
and p-polarized light, respectively, and with a photon energy of $h\nu = 6$ eV.
Light incidence was along k_x and at an incidence angle $\Theta = 8°$ between the
sample surface and the incoming light. The sample was oriented such that
the mirror plane along $\bar{\Gamma}\bar{M}$ coincides with the direction of light incidence.
The intensity around the state from $\alpha = 0°$ to $360°$ as indicated by the red
dotted line in (a) is plotted for s-polarized (red markers) and p-polarized
(black markers) light in (c). (d) shows a momentum distribution curve
(black) extracted along the blue dotted line in (b) and the corresponding
Voigt line profiles, which were fitted to the experimental data (blue and
gray lines).

setup in Halle, which allows to capture the complete momentum half space at variable energies $E - E_F$. The 4th harmonic of a Ti:Sa oscillator with an energy of $h\nu = 6$ eV and tunable light polarization served as light source. In the measurements shown, the light polarization was changed from s-polarized in (a) to p-polarized in (b). The direction of light incidence was along the k_x-axis and at an angle $\Theta = 8°$ between light beam and sample surface (compare also Fig. 3.1 in section 3). The sample was oriented within 5° from $\bar{\Gamma}\bar{M} \| k_x$ as denoted in Fig. 5.2, therefore, light incidence was parallel to the mirror plane of the crystal.

In both, Fig. 5.2 (a) and (b), a circular structure around the $\bar{\Gamma}$-point can be observed with the maximum of the photoemission intensity at roughly $|\boldsymbol{k}_{\|}| = 0.12\,\overset{\circ}{\text{A}}^{-1}$, which stems from the topological surface state of Bi_2Te_2Se. At close examination a slight hexagonal warping with the vertices along k_x is visible, which is in accordance with the measurements shown in section 4.1. Evidently, the photoemission intensity distribution differs significantly between the measurements shown in (a) and (b). The measurement with s-polarized light (a) shows a very symmetric intensity distribution with regard to the k_x- as well as the k_y-axis. The highest intensity is found along k_x at $k_y = 0\,\overset{\circ}{\text{A}}^{-1}$, whereas at $k_x = 0\,\overset{\circ}{\text{A}}^{-1}$ the photoemission intensity is considerably weaker. The situation is reversed for the measurements with p-polarized light, where the maxima in intensity are along k_y at $k_x = 0\,\overset{\circ}{\text{A}}^{-1}$, whereas there are minima in intensity along k_x, especially pronounced for negative wave vectors $k_x < 0\,\overset{\circ}{\text{A}}^{-1}$.

Fig. 5.2 (c) shows the integrated photoemission intensities as deduced from Voigt line profiles that were fitted to momentum distribution curves for azimuthal angles from $\alpha = 0°$ to 360°. The positions of the momentum distribution curves are indicated by the red lines, and the angles α by the red dashed arrow in (a). One example for such a momentum distribution curve is shown for p-polarized light in Fig. 5.2 (d). The MDC intersects the state at angles of $\alpha = 90°$ and $\alpha = 270°$, the corresponding cut through the constant energy map is represented by the blue dotted line in (b). The measured intensity (black solid line) shows two intensity maxima at $-0.12\,\overset{\circ}{\text{A}}^{-1}$ and $+0.12\,\overset{\circ}{\text{A}}^{-1}$. Three Voigt profiles were fitted to the momentum distribution curve. The gray peak at $k_y = 0\,\overset{\circ}{\text{A}}^{-1}$ very likely stems from the bulk conduction band, which shows no distinct intensity in the constant energy plots in (a) and (b), but still significantly contributes to the total intensity as evident from the intensity profile in (d). The intensity of the topological surface state is deduced from the light blue Voigt profiles and yields the intensity plotted in Fig. 5.2 (c) for angles of $\alpha = 90°$ and 270°. The sum of the three Voigt line profiles is displayed as dark blue line in (d).

The intensity distribution over 360° in Fig. 5.2 (c) shows dips in intensity at $\alpha = 90°$ and 270°, whereas maxima are at $\alpha = 0°$ and 180° for s-polarized light (black markers). For p-polarized light (red markers) two distinct maxima are at approximately 100° and 250°, while intensity dips can be found at $\alpha = 0°$ and 180°. This

47

confirms the apparent change of the photoemission intensity distribution between measurements with p- and with s-polarized light.

The maxima for measurements with p-polarized light are not at the symmetric positions of $\alpha = 90°$ and $270°$ but slightly shifted towards $\alpha = 180°$. In addition, the intensity at $\alpha = 0°$ is lower than at $180°$, as clearly visible in (c). Such a deviation from a symmetric intensity distribution is in principle not prohibited when p-polarized light is used: Whereas for s-polarization the light polarization $\hat{\epsilon}$ is mirror symmetric with regard to $\pm k_x$, it breaks mirror symmetry for p-polarization, where the polarization direction $\hat{\epsilon}$ of the vector field $\boldsymbol{A}$ consists of a component along x as well as a component along z.

From the s-polarization data it is already possible to gain information about the orbital composition. Since s-polarization exclusively addresses p_y-orbitals, the in-plane orbital composition of the topological surface state must consist of mainly p_x-orbitals along $k_x = 0 \, \mathring{A}^{-1}$, that is at $\alpha = 90°$ and $270°$, where the intensity is strongly decreased for s-polarized light. Along $k_y = 0 \, \mathring{A}^{-1}$ on the other hand, that is at $\alpha = 0°$ and $180°$, the intensity is at a maximum, indicating a strong contribution of p_y-orbitals. Therefore, from the data measured with s-polarized light one can derive that the in-plane orbital structure consists of predominantly tangentially aligned p-like orbitals. This is supported by the data sets in Fig. 5.2 (b) obtained with p-polarized light, which addresses the p_z- and p_x-orbitals. The data indicates a stronger contribution of p_x-orbitals along $k_x = 0 \, \mathring{A}^{-1}$, based on the increased intensity along $k_x = 0 \, \mathring{A}^{-1}$ as compared to $k_y = 0 \, \mathring{A}^{-1}$. It must be noted though, that since a mixture of p_x- as well as p_z-like states contribute to the overall photoemission intensity, the interpretation can become less straightforward, as will be addressed in detail later in this work.

Similar analysis of the orbital composition have been performed theoretically and experimentally on the topological surface state of $Bi_2Se_3(0001)$ [153, 154], finding a likewise tangentially aligned in-plane orbital composition for the upper part of the Dirac cone. This is in line with the results shown here on Bi_2Te_2Se, which belongs to the Bi_2Se_3 family of topological insulators. Therefore, in terms of the orbital composition, topological surface states of the group V_2VI_3 layered topological insulators seem to exhibit a similar orbital composition at least in the upper part of the topological surface state. For $Bi_2Se_3(0001)$ the lower part of the Dirac cone was shown to consist of a different, namely radially aligned orbital texture [153, 154]. The lower part of the topological state of Bi_2Te_2Se was not probed within this work, since it is not clearly distinguishable by ARPES, due to an overlap with bulk states.

The analysis of the in-plane orbital composition of the topological surface state of Bi_2Te_2Se is a nice example of how information about the composition of the wave function can be extracted from photoemission data. The result is not unexpected, since
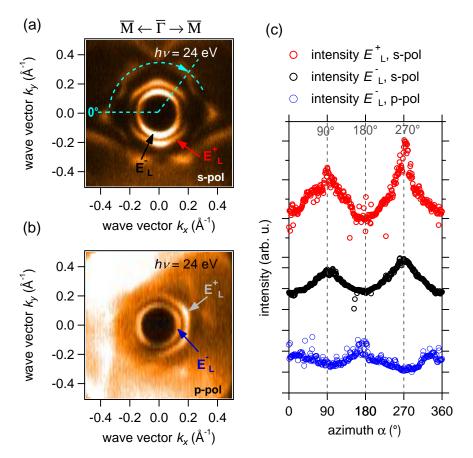
FIGURE 5.3. **Orbital character of the surface states of PbAg$_2$/Ag(111).** (a) and (b) show ARPES data sets measured with a photon energy of $h\nu = 24$ eV and s- and p-polarized light, respectively. The light incidence was along the k_x-axis and at an angle of $\Theta = 40°$. The sample was oriented with $\bar{\Gamma}\bar{M}$ parallel to k_x, as labeled in (a). The two innermost structures, which are indicated by arrows, belong to the lower (-) and upper (+) branch of the surface state E_L and are labeled accordingly. (c) shows the intensity distribution determined from Voigt line profiles that were fitted to momentum distribution curves from $\alpha = 0°$ to $360°$ as schematically illustrated by blue dashed lines in (a).

49

it mirrors the orbital structure of the Dirac-cone of $Bi_2Se_3(0001)$. It is, furthermore, interesting to investigate, whether a similar situation can be found for surface states of a different origin, namely topologically trivial surface states which exhibit a Rashba type spin-splitting. The analysis of the orbital composition will, therefore, be extended to the surface states of $PbAg_2$/Ag(111) and $BiAg_2$/Ag(111). Both materials show large Rashba-type splittings in their surface electronic structure, due to strong spin-orbit coupling. Owing to the large sized spin-splittings, it is possible to access the two Rashba-split branches separately by photoelectron spectroscopy, making the materials ideal model systems to probe the orbital texture of a Rashba-type state.

The Fermi surface of $PbAg_2$/Ag(111) is presented in Fig. 5.3 (a) and (b) for measurements with s-polarized and p-polarized light, respectively. The measurements were carried out at beamline BL 9A at the Hiroshima synchrotron radiation center. The photon energy was $h\nu = 24$ eV and the measurements were performed with light incidence along k_x and at an angle of $\Theta = 40°$ between sample surface and light beam. The sample was aligned with $\bar{\Gamma}\bar{M}$ along k_x.

The most prominent features in the Fermi surfaces are two structures around $\bar{\Gamma}$ which can be assigned to the lower Rashba surface state E_L. The inner circular structure is the lower branch E_L^- of the state, while the outer hexagonally deformed structure stems from the upper branch E_L^+. The hexagonal deformation is oriented with the tips of the hexagon along $\bar{\Gamma}\bar{K}$. There are further states at higher wave vectors $\boldsymbol{k}_{||}$, which again show a strong hexagonal deformation with a 30° rotated orientation compared to the state E_L. The following discussion will be concentrated on the upper and lower branch E_L^+ and E_L^- of the lower surface state.

Similar to the topological surface state of Bi_2Te_2Se the photoemission intensity distribution of the Rashba surface state E_L in $PbAg_2$ as measured with s-polarized light in (a) is highly symmetric with regard to k_x as well as k_y, whereas mirror symmetry with regard to $\pm k_x$ is broken for p-polarized light, which in principle allows asymmetries in the photoemission intensity distribution.

When measured with s-polarized light, the intensity is highest along the k_y-axis at $k_x = 0\,\text{Å}^{-1}$ for both branches of the state E_L. This is demonstrated in detail by the intensity plots in Fig. 5.3 (c), which were determined from Voigt line profiles fitted to momentum distribution curves in the same manner as described before in the case of Bi_2Te_2Se. The momentum distribution curves were extracted along lines at azimuthal angles from $\alpha = 0°$ to 360° as indicated by the blue dashed line in (a). The resulting intensity distribution in (c) for the inner (black markers) as well as the outer (red markers) structure shows the same overall modulation around the Fermi surface. The maxima in intensity lie at approximately $\alpha = 90°$ and 270°, while the minima are at $\alpha = 0°$ and 180°. Interestingly this is in contrast to the case of Bi_2Te_2Se where the maxima lie along k_x at 0° and 180°, a clear indication for a different orbital

composition of the surface states of the two materials.

For measurements performed with p-polarized light, shown in Fig 5.3 (b), the inner branch of the state has intensity dips along the k_y-axis, whereas along the k_x-axis the photoemission intensity is considerably higher. For the outer structure the contour can be clearly distinguished only for $k_x > 0$, since the intensity at $k_x < 0$ is too low to be traced against the high intensity background. Therefore, an analysis of the photoemission intensity by Voigt line profiles fitted to the state for azimuthal angles from $\alpha = 0°$ to $360°$ could only be performed for the inner structure (blue markers in (c)). Here again minima in intensity lie at approximately $90°$ and $270°$, whereas the most prominent maximum is at $\alpha = 180°$ opposite to the measurements with s-polarized light.

A likewise analysis as performed for Bi_2Te_2Se yields a radially aligned in-plane orbital composition for both branches of the state E_L. More precisely, from the s-polarization measurement it is obvious that there is almost no contribution of p_y-orbitals along k_x at $k_y = 0\,\mathring{A}^{-1}$, since the photoemission intensity is zero for the upper branch E_L^+ and only small for the inner branch E_L^-. At $k_x = 0\,\mathring{A}^{-1}$, on the other hand, the photoemission intensity is high, indicating a considerable portion of p_y- that is radially aligned orbitals. Thus, the contributing p-orbitals are aligned radially to the lower surface state of $PbAg_2/Ag(111)$. This is supported by the fact that for p-polarization the intensity of the inner branch E_L^- is lower along $k_x = 0\,\mathring{A}^{-1}$, albeit not completely zero, indicating a possibly higher p_y contribution along k_x at $k_y = 0\,\mathring{A}^{-1}$.

Unlike the case of the topological surface state of $Bi_2Se_3(0001)$, where the in-plane orbital structure consists of tangential orbitals in the upper and radial orbitals in the lower branch of the Dirac cone [153, 154], the orbital composition of the two branches of the Rashba-split surface state E_L in $PbAg_2/Ag(111)$ is the same. Similar to the upper part of the Dirac cone in Bi_2Te_2Se, the in-plane orbital composition of the surface state E_L of $BiAg_2$ is mainly constructed of one type of orbital alignment, not a mixture. Nevertheless, the alignment is opposite — tangential in Bi_2Te_2Se and radial in $PbAg_2$. This observation reveals a difference in the orbital texture of the Rashba-split surface state and the topological surface state.

Early theoretical works on $PbAg_2$ calculated an orbital composition of mainly sp_z-character for the lower surface state E_L [148]. A different analysis likewise predicted mainly p_z-character for the equivalent surface state of the surface alloy $BiAg_2$, albeit with increasing contributions from $p_{x,y}$-orbitals for an increasing outward relaxation of the surface atoms leading at the same time to a larger spin-splitting [61]. The results shown above demonstrate that the orbital composition is not primarily p_z-like, but has a large contribution of $p_{x,y}$-orbitals in contrast to the early theoretical works.

A newer study on $PbAg_2$/Ag(111) [155] claims that the lower occupied state consists of mainly radially aligned orbitals in agreement with the results shown here. Only for small wave vectors $\boldsymbol{k}_{\|}$ the contribution of tangentially aligned orbitals to the surface state seems to be predominant in reference [155]. An indication for such a $\boldsymbol{k}_{\|}$-dependence can also be observed in the experimental data in Fig. 5.3 (a), where the upper branch E_L^+ of the state has no visible p_y contribution, whereas the lower branch E_L^- yields some photoemission intensity at wave vectors along $k_y = 0\,\mathring{A}^{-1}$. This might suggests an increasing contribution of tangentially aligned orbitals for decreasing $\boldsymbol{k}_{\|}$ in accordance to the proposed orbital structure in reference [155].

In the theoretical analysis in reference [155] a $\boldsymbol{k}_{\|}$-dependence of the orbital character is predicted to be even more pronounced in the upper state E_U. Here, for small wave vectors $|\boldsymbol{k}_{\|}|$ the state consists of predominantly radially aligned orbitals, whereas for increasing $|\boldsymbol{k}_{\|}|$ tangentially aligned orbitals dominate [155]. However, in the case of the surface alloy $PbAg_2$ the upper state E_U lies mainly in the unoccupied part of the band structure. In the occupied range, it shows no splitting but is degenerate, making an analysis of the orbital character by photoelectron spectroscopy difficult. In order to analyze the orbital composition of the upper surface state E_U, a promising approach is to analyze the surface electronic structure of $BiAg_2$/Ag(111), which has a similar structure and can, therefore, be assumed to have a similar orbital composition of the surface states, which are shifted to lower energies compared to $PbAg_2$/Ag(111). The upper state E_U of the surface band structure of $BiAg_2$/Ag(111) still largely lies in the unoccupied part of the bands, but shows a larger splitting and is shifted to smaller wave vectors $|\boldsymbol{k}_{\|}|$ (compare section 4). It can thus partly be investigated by photoelectron spectroscopy.

Fig. 5.4 (a) and (b) show the Fermi surface of $BiAg_2$/Ag(111) measured at the beamline i3 at Max Laboratories in Lund. Both data sets were acquired with s-polarized light with a photon energy of $h\nu = 22\,\text{eV}$ and $h\nu = 24\,\text{eV}$, respectively. Light incidence was along the k_x-direction and at an angle $\Theta = 17°$ between light beam and sample surface. The innermost structure stems from the maxima of the lower band E_L that lie close to the Fermi level. It is almost circular with only slight hexagonal deformation, where the vertices of the hexagon point along $\bar{\Gamma}\bar{M}$. At slightly higher wave vectors a second hexagonal structure is visible, which can be assigned to the higher branch E_U^+ of the upper state, whose maxima lie in the unoccupied part of the band structure. Again the vertices of the hexagon are oriented along k_x. At even higher wave vectors additional states are visible, which will not be discussed here.

The upper state is marked by red arrows in Fig. 5.4. For both photon energies the photoemission intensity has a minimum along the k_y-axis, whereas it is much higher along the k_x-axis, indicating a large contribution of p_y-orbitals along k_x and no p_y
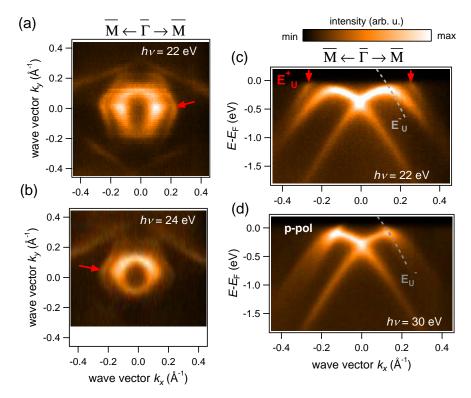
FIGURE 5.4. **Momentum-dependent orbital composition in the surface bands of BiAg$_2$/Ag(111).** (a) and (b) show momentum distribution maps of the electronic structure of BiAg$_2$ at the Fermi energy. They were measured with s-polarized light and a photon energy of $h\nu = 22$ eV in (a) and $h\nu = 24$ eV in (b). The sample was oriented with $\bar{\Gamma}\bar{M}$ in the plane of incidence with an angle between the direction of light incidence and the sample surface of $\Theta = 17°$. An ARPES data plot measured at $h\nu = 22$ eV along k_x ($k_y = 0$) is displayed in (c). Arrows mark the outer branch E_U^+ of the upper state, while the gray dashed line shows the dispersion of the lower branch E_U^- as determined from photoemission data acquired with p-polarized light and a photon energy of $h\nu = 30$ eV, which is shown for comparison in (d).

contributions along k_y. This suggests that the in-plane orbitals are aligned tangential
to the state similar to the case of Bi_2Te_2Se but in contrast to the surface state E_L in
$PbAg_2$. The same observation can be made for the occupied state E_L, which also yields
the highest photoemission intensity along $k_y = 0\,\text{Å}^{-1}$. It should be noted though, that
the intensity dip along the k_y-axis is not as clear — especially for the measurements
with $h\nu = 24\,\text{eV}$ — as for the upper state. The data, therefore, suggests a higher ratio
of tangentially aligned orbitals with a contribution of radial orbitals in the in-plane
orbital composition of the surface state E_L of $BiAg_2/Ag(111)$.

In Fig. 5.4 (c) an ARPES plot of the band structure is presented, which was
measured with s-polarized light and a photon energy of $h\nu = 22\,\text{eV}$ in the same experi-
mental geometry as in (a) and (b). The brightest band is the surface state E_L which
shows large Rashba-type splitting and has maxima at approximately $k_x = \pm 0.15\,\text{Å}^{-1}$.
In addition, the upper branch E_U^+ of the state E_U is visible and marked by red arrows.
The lower branch E_U^-, on the other hand, shows no intensity at all. At positive wave
vectors its expected dispersion is indicated by a dashed gray line. It was deduced from
a measurement with p-polarized light at a photon energy of $h\nu = 30\,\text{eV}$, displayed
for comparison in (d), where the branch E_U^- is clearly visible, whereas the branch
E_U^+ has no intensity. The absence of photoemission intensity from the lower branch
E_U^- in the data measured with s-polarized light indicates that the spectral weight in
(a) and (b) of the inner structure exclusively stems from the state E_L. The fact that
the two branches do not appear simultaneously in the measurements with either s-
or p-polarized light in (c) and (d) can be taken as evidence that the two branches of
the upper state have different orbital compositions. More precisely, the branch E_U^+
has a significant contribution of tangentially aligned p_y-orbitals along the k_x axis,
whereas the lower branch E_U^- most likely has predominantly radial (p_x along k_x) and
p_z-character.

Compared to $PbAg_2$ the measurements on $BiAg_2$ indicate a different, that is
tangentially aligned, in-plane orbital structure. This can on the one hand be caused
by structural differences between the two materials, for instance the amount of out-
of-plane relaxation of the atoms can influence the strength of orbital mixing [61].
On the other hand, due to the different energetic positions of the surface states in
$PbAg_2/Ag(111)$ and $BiAg_2/Ag(111)$, the constant energy cuts at the Fermi energy
shown for $BiAg_2$ in Fig. 5.4 are much closer to the Rashba degeneracy point, where a
larger portion of tangentially aligned orbitals compared to radially aligned orbitals
is expected also for $PbAg_2$ [155]. Such an interpretation is supported by the higher
intensity of the band above $E - E_F = -0.5\,\text{eV}$ and between approximately $\pm 0.2\,\text{Å}^{-1}$ in
Fig. 5.4 (c), which might also point towards a larger contribution of p_y-orbitals at
small wave vectors.

For the surface state E_U of $BiAg_2$ the apparent dominance of radial and p_z-orbitals

in the lower branch is in accordance with theoretical predictions for PbAg$_2$ [155], where for small wave vectors radial orbitals dominate, while at larger $|\boldsymbol{k}_{||}|$ the state consists of tangential orbitals. Theoretical calculations of the band structure of the surface alloy BiAg$_2$ likewise predict a change of orbital character of the upper state E_U with increasing $|\boldsymbol{k}_{||}|$ [156]. A similar orbital structure was also found in the surface alloy BiCu$_2$/Cu(111) [152], which exhibits a surface electronic structure comparable to BiAg$_2$/Ag(111) and PbAg$_2$/Ag(111). Here, mainly radial in-plane orbital contributions for the lower branch E_L^- of the lower band and purely p_z-orbitals in the upper branch E_L^+ were predicted, which at least for the lower branch corresponds to the presented results on PbAg$_2$/Ag(111). For the upper band of BiCu$_2$/Cu(111) on the other hand a mainly tangential character, with an almost completely vanishing radial component below the Fermi level is expected [152], corresponding to the tangential character of the upper branch E_U^+ of the surface state E_U observed in the presented data on BiAg$_2$/Ag(111).

With the tangential in-plane orbital composition of the topological surface state of Bi$_2$Te$_2$Se and the radial alignment of the p-orbitals in the lower surface state E_L in the surface electronic structure of PbAg$_2$/Ag(111) two different possible in-plane orbital distributions and their signature in the spectral weight distribution were already discussed. In both cases the alignment of the p-orbitals is almost purely tangential or radial. Of course, also a mixing of the orbitals is a possible scenario. In the following the orbital composition of the conduction band surface state (CBS) of BiTeI will be analyzed. Here, the data indicates a more complicated situation and a larger mixing of the different in-plane p-orbitals.

The electronic structure of BiTeI was measured at the momentum microscope at the Max Planck institute in Halle with a photon energy of $h\nu = 6$ eV. Momentum maps at $E - E_F = -0.13$ eV are shown in Fig. 5.5 (a) and (b) for s- and p-polarized light, respectively. The direction of light incidence was along the k_x-axis and at an angle of $\Theta = 8°$ with respect to the sample surface. The most pronounced structure is a circular intensity at approximately $|\boldsymbol{k}_{||}| = 0.15\,\text{Å}^{-1}$, which is highlighted by a dashed circle in (a) that serves as guide to the eyes. This intensity belongs to the lower branch E_{CB}^- of the conduction band induced surface state CBS in BiTeI. The inner branch E_{CB}^+ cannot be distinguished, due to a high intensity in the center with an intensity maximum at $\boldsymbol{k}_{||} = 0\,\text{Å}^{-1}$, which presumably stems from bulk bands. The intensity of the conduction band state, on the other hand, is rather low, making it difficult to analyze the light-polarization dependent intensity distribution from the momentum maps alone.

Fig. 5.5 (c) and (d) show momentum distribution curves obtained from the data displayed in (a) and (b). The exact traces, along which the momentum distribution
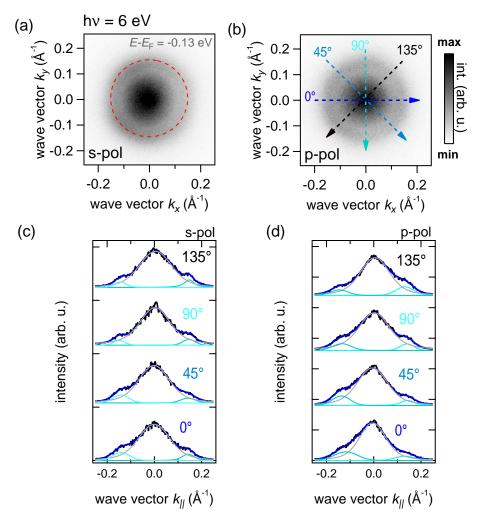
FIGURE 5.5. **Photoemission intensity distribution of the conduction
band surface state of BiTeI.** In (a) and (b) photoemission data ob-
tained with s- and p-polarized light, respectively, and a photon energy of
$h\nu = 6\,\text{eV}$ are presented. The direction of light incidence was along the
k_x-axis and at an incidence angle of $\Theta = 8°$. (c) and (d) show intensity
distribution curves (black lines) obtained from the data sets in (a) and
(b), respectively. The dashed lines in (b) illustrate the cuts through both
momentum maps that are displayed in (c) and (d), with arrows indicat-
ing positive $k_\|$. Blue and gray curves are Voigt line profiles fitted to the
intensity profiles.

curves for both s- and p-polarized light were taken, are indicated by dotted arrows in (b) where the tip of the arrow signifies positive wave vectors $\boldsymbol{k}_{||}$ in (c) and (d). The obtained momentum distribution curves (black lines in (c) and (d)) were fitted with three Voigt profiles, displayed as blue and gray lines. The high intensity in the center at $|\boldsymbol{k}_{||}| = 0\,\mathring{A}^{-1}$ stems from the bulk conduction band. For all angles this intensity peak has a shoulder on both sides which can be attributed to the conduction band surface state. From a comparison of these shoulders, it is possible to determine the distribution of the photoemission intensity around the conduction band state. It is important, however, to take notice of the fact that in this case the sample was not aligned along a high symmetry direction, which might introduce asymmetries to the measured photoemission intensity distribution.

For s-polarized light (Fig. 5.5 (c)) the shoulders (light blue Voigt profiles) of the center peak show a rather symmetric intensity distribution. At closer evaluation the peak at negative wave vectors $|\boldsymbol{k}_{||}| < 0\,\mathring{A}^{-1}$ is slightly more intense for the momentum distribution curves at 0° and 45°, whereas the two shoulders are almost equal at 90°. At 135° the shoulder at positive wave vectors seems slightly more intense. If we take the traces along which the cuts were taken into account, it seems that there might be a small intensity asymmetry with higher intensity for $k_x < 0\,\mathring{A}^{-1}$.

For p-polarized light the intensity distribution is slightly more asymmetric. For momentum distribution curves at 0° and 45° the intensity of the shoulder at negative wave vectors $|\boldsymbol{k}_{||}| < 0\,\mathring{A}^{-1}$ is significantly higher compared to the shoulder at positive wave vectors $|\boldsymbol{k}_{||}| > 0\,\mathring{A}^{-1}$. At 90° the intensity distribution is equal within experimental accuracy, whereas at 135° the intensity at positive wave vectors is significantly higher. Here, an enhanced intensity for $k_x < 0\,\mathring{A}^{-1}$ is more evident than in the case of s-polarization.

The absence of clear minima in the photoemission intensity distribution measured with either p- or s-polarized light indicates that there is no pure tangential or radial p-orbital distribution but rather a mixing of both. There are p_y-orbital contributions along k_y (radial) as well as along k_x (tangential), therefore, no clear minimum in photoemission intensity can be observed for measurements with s-polarized light.

Up to now, the role of the out-of-plane orbital p_z was neglected in the discussion. For p-polarized light however, the contribution of electrons photoemitted from p_z-orbitals is significant, at small angles of light incidence Θ it can even be considered predominant. Therefore, the conclusions about the in-plane orbital composition were carefully drawn from measurements with s-polarization, only, whereas the measurements with p-polarization were only considered as additional support.

All in all the presented analysis in this section is a demonstration of the capability of photoelectron spectroscopy to disentangle the in-plane orbital composition of the sur-

face electronic structure of different types of materials. The photoemission signatures
of the topological surface state of Bi_2Te_2Se as well as the Rashba-type surface state
of $BiAg_2$/Ag(111) and $PbAg_2$/Ag(111) demonstrate that the wave functions contain
in-plane orbitals, which are aligned either tangentially or radially to the state. The
conduction band surface state of BiTeI, however, has a mixed in-plane orbital structure.
In the following the same approach will be utilized to gain additional understanding
of the locking between spin and orbital degree of freedom.

5.2   Spin-orbital texture

The results presented in the previous section constitute a striking example of the
possibility to probe the in-plane orbital composition by photoelectron spectroscopy
using linearly polarized light. This method can be extended to a spin-resolved experi-
ment, which then allows to disentangle the spin- and orbital texture of the electronic
states. For a given quantization axis along y the spin-up and spin-down part of the
wave function is coupled to the even and uneven spatial wave function, respectively,
and the initial state can be expressed as $|\Psi_i\rangle = |p_x, \uparrow (\downarrow)\rangle + |p_y, \downarrow (\uparrow)\rangle + |sp_z, \uparrow (\downarrow)\rangle$ as
already stated in a more general fashion at the beginning of the chapter [152]. Since
the uneven and even spatial part of the wave function — in the present example the
p_y and $p_{x,z}$ part — are probed by s- and p-polarized light, respectively, a spin-resolved
photoemission experiment performed with linearly polarized light can give access to
the coupling between spin and orbital degree of freedom. For BiTeI the tangentially
and radially aligned in-plane p-orbital structure, which consist of p_y- or p_x-orbitals
along k_x, were shown above to have similar cross sections and, therefore, contribute
equally to the overall photoemission intensity. As a result, the spin structure coupled
to the different orbital structures can efficiently be probed for BiTeI, as will be shown
in the following. Furthermore, the spin-orbital texture of the topological surface state
of Bi_2Te_2Se will be investigated in the next section. Parts of the data presented in this
section are already published [37].

Fig. 5.6 (a) and (b) show spin-resolved photoemission data of the BiTeI(0001)
conduction band surface state (CBS), measured with the momentum microscope at the
Max Planck institute in Halle. The photon energy was $h\nu = 6\,\text{eV}$ and the sample was
aligned in such a way that the direction of light incidence lies in the mirror plane along
$\bar{\Gamma}\bar{M}$ and at an angle of $\Theta = 8°$ with regard to the sample surface. The binding energy
with respect to the Fermi energy is $E - E_F = -0.11\,\text{eV}$ and the data was measured
with s-polarized light in (a) and p-polarized light in (b). Red color denotes positive spin
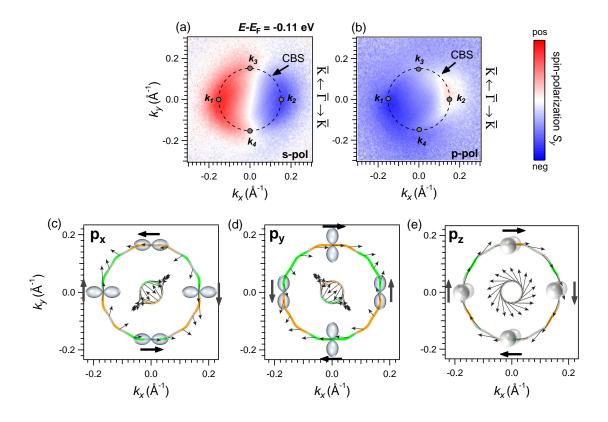polarization $S_y > 0$, where $S_y || k_y$, whereas blue signifies a negative spin polarization

FIGURE 5.6. **Orbital resolved spin-texture of the conduction band surface state of BiTeI.** In (a) and (b) spin-resolved intensity plots of the conduction band state (CBS) of BiTeI at $E - E_F = -110$ meV measured with s- (a) and p- (b) polarized light are displayed. Light incidence was along the k_x-axis and at an angle of $\Theta = 8°$, the photon energy was $h\nu = 6$ eV. Red and blue color signifies the spin polarization S_y along the positive/negative y-axis. Dashed circles serve as guides to the eyes for the surface state and gray dots mark points k_{1-4} in $\boldsymbol{k}$-space that are discussed in the main text. (c) - (e) show calculated projections of the spin polarization on the p_x-, p_y- and p_z-orbitals. The in-plane spin polarization is indicated by gray arrows, while the out-of-plane spin component is encoded with green for negative and orange for positive spin polarization $\pm S_z$.

59

$S_y < 0$. Dashed circles serve as guides to the eyes for the conduction band state and gray dots mark points k_{1-4} in $\boldsymbol{k}$-space that will be discussed in the following.

The differences with changing light polarization in Fig. 5.7 (a) and (b) are significant. The most prominent observation is the almost symmetric distribution between $+S_y$ and $-S_y$ for s-polarized light, whereas a rather large asymmetry occurs for p-polarized light. When considering the points k_1 and k_2, there is also an apparent spin reversal. For s-polarized light we measure positive spin polarization at k_1 and negative polarization at k_2, while the opposite is the case when p-polarized light is used. Since with different light polarization different orbitals are probed, these observations in itself are evidence for a coupling between the spin and orbital degree of freedom.

An interpretation of these observations becomes possible with the help of DFT ground state calculations which were performed by Sergey Eremeev and published in reference [37]. They are displayed in Fig. 5.6 (c) to (e). The calculations show the projection of the total spin polarization $\boldsymbol{S}$ onto the p_x-, p_y- and p_z-orbital in (c), (d) and (e), respectively. The in-plane spin polarization $S_{x,y}$ is displayed as gray arrows, while the out-of-plane spin polarization is indicated by green and orange color for negative and positive spin polarization along z. At the points k_1 and k_2 the projected spin polarization S_y is opposite for the $p_{x,z}$- and the p_y-orbital. This is in accordance with our measurements since $p_{x,z}$- and p_y-orbitals can be addressed by p- and s-polarized light, respectively.

At the points k_3 and k_4 the photoelectron spin polarization is zero for measurements with s-polarized light. The calculated projection of the spin polarization on the p_y-orbital predicts an in-plane spin polarization $\pm S_x$ along x at k_3 and k_4. Since our experiment is only sensitive to the spin polarization S_y along y this implies an agreement between the measurement performed with s-polarization and the calculated in-plane spin polarization. On the contrary, for p-polarization the measurement yields a significant spin polarization S_y at k_3 and k_4. Since the calculated in-plane spin polarization is parallel to k_x for the projections on the p_x- and p_z-orbitals at k_3 and k_4, there is a sharp contrast between ground state calculations and spin polarization measurements when p-polarized light is used.

The calculated projections to in-plane orbitals can also be examined in terms of tangentially and radially oriented p-orbitals. The radial p-orbitals, that is the p_x-orbital at points k_1 and k_2 and the p_y-orbital at k_3 and k_4 show a clockwise spin chirality, while the tangentially aligned orbitals, namely p_y at points k_1 and k_2 and p_x at k_3 and k_4 are coupled to an anticlockwise spin-chirality as depicted in Fig. 5.6 (c)-(e).

The same spin- and orbital-resolved experiment was performed on the topological surface state of $Bi_2Te_2Se(0001)$. The results are presented in Fig. 5.7 (a) and (b). The corresponding spin-integrated measurements were already discussed in connection
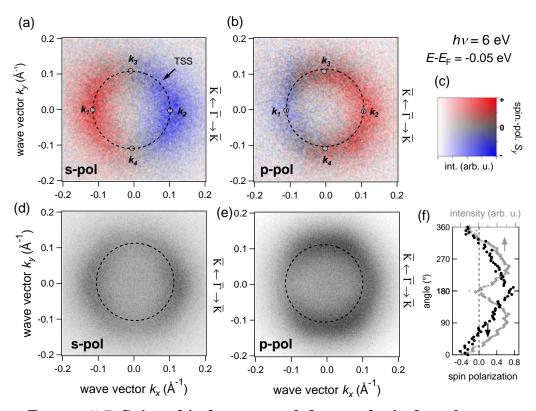
FIGURE 5.7. **Spin-orbital texture of the topological surface state of Bi$_2$Te$_2$Se.** In (a) and (b) Spin-resolved momentum distribution maps measured at an energy $E - E_F = -0.05$ eV are presented. Red and blue color indicate the spin polarization S_y along the positive/negative y-axis and color strength denotes the photoemission intensity as indicated in the 2D color scheme in (c). (d) and (e) show corresponding spin-integrated data sets. The data was obtained with linearly s-polarized (a),(c) and p-polarized (b),(d) light and a photon energy of $h\nu = 6$ eV. Light incidence was parallel to the k_x-axis and at an angle of $\Theta = 8°$. Dashed circles serve as guides to the eyes for the TSS and gray dots indicate points in **k**-space which are discussed in detail in the main text. A comparison of the spin-integrated photoemission intensity (gray markers) and the spin polarization (black markers) for the data acquired with p-polarized light is displayed in (f).

61

with Fig. 5.2 but are shown once more in Fig. 5.7 (d) and (e) for better comparability but in a different color scheme. The photon energy was $h\nu = 6\,\mathrm{eV}$ and the direction of light incidence was along k_x, which is in the mirror plane ($\bar{\Gamma}\bar{M}$) of the material, and at an angle of $\Theta = 8°$ with regard to the sample surface. The binding energy with respect to the Fermi energy is $E - E_F = -0.05\,\mathrm{eV}$ and the data was measured with s-polarized light in (a) and (d) and p-polarized light in (b) and (e). Red and blue again denotes the positive and negative spin polarization S_y along the y-axis, the color strength additionally stands for the photoemission intensity. This can be seen in detail in the 2D color scheme in (c). Dashed circles serve as guides to the eyes for the topological surface state and gray dots once more mark selected points k_{1-4} in $\boldsymbol{k}$-space.

Analogue to the data on BiTeI presented above, the two most prominent observations concerning a comparison between the spin-resolved measurements with s- and p-polarized light are an evident reversal of the photoelectron spin polarization with regard to points k_1 and k_2 as well as a much higher asymmetry in the data measured with p-polarized light.

At k_1 and k_2 the in-plane orbital composition of the topological surface state consists of mainly tangentially aligned orbitals, as discussed in the previous section. The data presented in Fig. 5.7 (a) reveals a positive (red) spin polarization along S_y at k_1, whereas S_y is negative (blue) at k_2, when measured with s-polarized light. At points k_3 and k_4 on the other hand the spin polarization is zero, therefore, no spin component S_y along y can be measured, suggesting a clockwise spin chirality in the tangentially aligned p-orbitals as expected for a helical spin structure of the surface state. For measurements with p-polarized light on the other hand, the measured spin polarization along y is negative at k_1 and positive at k_2. This can once more be interpreted as the signature of a reversed spin chirality in the p_x- and p_z-orbitals as compared to the p_y-orbital. The presented experimental data suggests that the topological surface state of Bi_2Te_2Se exhibits a clockwise spin chirality in the tangentially aligned orbitals and an anticlockwise chirality in the radial plus out-of-plane p-orbitals.

A coupling between the photoelectron spin polarization and the vector field $\boldsymbol{A}$ of the incoming light is not new, but has already been observed for the case of unpolarized ground states in early works on the photoelectron spin polarization [33, 35]. It is now well known and much studied in connection with the topological surface state of Bi_2Se_3 [31, 153, 154, 157–159], where a similar photoelectron spin reversal was observed, when the light polarization was switched from s- to p-polarized. With the light polarization dependent spin polarization reversal demonstrated here for the topological surface state of Bi_2Te_2Se, which belongs to the same family of topological insulators as Bi_2Se_3, another example of the spin-orbit coupling in topological surface states is added. Also for Rashba-type electronic states a likewise coupling

between spin and orbital was predicted [29, 160]. Interestingly, for the surface state of the model Rashba system Au(111) no coupling between the spin and orbital degree of freedom was found [31, 124], raising the question whether a non trivial topology might be essential for a spin-orbital coupling to evolve [161]. The data presented here on the Rashba-split surface electronic structure of BiTeI demonstrates, that a photoelectron spin-texture inversion can arise in materials with large spin-orbit coupling independent of the topology of the material.

At points k_3 and k_4 in Fig. 5.7 (a) the spin polarization is zero for s-polarized light as expected for a helical spin structure. For measurements with p-polarized light, however, the spin polarization S_y is finite and has positive sign at k_3 as well as at k_4. The resulting asymmetry in the spin-resolved measurements, which was likewise observed for the surface state of BiTeI, is in principle not forbidden, since the electric field of the light breaks symmetry with regard to the k_y-axis for p-polarization. The equal sign of the radial spin component at k_3 and k_4 on the other hand, is enforced by the mirror symmetry of the crystal with the mirror plane parallel to the k_x-axis. The mirror operation $\mathrm{M}: y \rightarrow -y$ can be expressed as $\mathrm{M}: k_+ \leftrightarrow -k_-, \sigma_y \rightarrow \sigma_y, \sigma_{x,z} \rightarrow -\sigma_{x,z}$ [130]. The spin polarization along y thus keeps its sign under mirror transformation, whereas the sign of the spin polarization along x and z must switch.

While the reason for the equal sign of S_y at k_3 and k_4 is comprehensible from symmetry arguments, the actual origin of the asymmetry in the measurements is not immediately clear. A comparison to the spin-integrated data in Fig. 5.7 (d) and (e) shows that the switch of the spin polarization from positive to negative coincides with the distribution of photoemission intensity. For the measurements with s-polarized light the spin polarization goes to zero (Fig. 5.7 (a)) at points k_3 and k_4 where also the spin-integrated photoemission intensity is at a minimum (Fig. 5.7 (d)) as expected for tangentially aligned p-orbitals and a clockwise spin chirality. For measurements with p-polarized light the spin polarization in Fig. 5.7 (b) appears to switch at approximately the same points in $\boldsymbol{k}$-space, where also the largest changes of the photoemission intensities occur in the spin-integrated measurements shown in Fig. 5.7 (e).

A possible correlation is analyzed in more detail for p-polarized light in (f). Here, the azimuthal distribution of photoemission intensity around the state at azimuthal angles from $0°$ (corresponding to point k_1) to $360°$ (k_1) in clockwise direction is plotted with gray markers. The same data was shown before in Fig. 5.2 (c). Black dots additionally signify the measured spin polarization S_y, which was extracted from the spin-resolved data set in (b) by determining the mean spin polarization value between $|\boldsymbol{k}_{||}| = 0.09\,\text{Å}^{-1}$ and $0.12\,\text{Å}^{-1}$ for angles from $0°$ to $360°$. The standard error of the mean spin polarization is below 0.03 for all data points. Arrows in (f) point to the axis of the graph that correspond to the spin polarization and photoemission intensity, respectively, and the dotted line denotes zero spin polarization but not zero

photoemission intensity. The spin polarization is zero at 65° and 315°. The slight
offset from a symmetric position with regard to the k_x-axis might be due to small
experimental errors for example a small mismatch of the camera position for the
spin detector with respect to the electron detector. At approximately 60° and 300° the
spin-integrated data shows large changes of the photoemission intensity, confirming
a possible correlation between photoelectron spin polarization and spin-integrated
photoemission intensity.

The observed asymmetries occur only, when p-polarized light is used, but equally
for spin-integrated as well as spin-resolved measurements. In the present case, with
p-polarized light, transitions from the p_x- as well as the p_z-part of the initial state can
occur at the same photon energies and the two corresponding transition channels can
interact with each other. An interference between the two transitions could effect both,
the spin-integrated as well as spin-resolved photoemission intensity. Effects in the
spin polarization caused by interference effects, were already predicted and observed
in early works [84, 85, 100] and are thus not unknown. An interference model, was
also developed for the topological insulator Bi_2Se_3 [157] for two atomic layers and
contributions from different p-orbitals. A more thorough discussion of the origin of
asymmetries in the photoemission data as well as the relation between spin-resolved
and spin-integrated photocurrent will be given at the end of chapter 6.

Whereas the agreement between the spin-resolved measurements and the ground
state calculations in Fig. 5.6 for s-polarized light seems to justify an interpretation
regarding only the initial state spin polarization, the measurements with p-polarized
light already demonstrate, that the photoemission process must be taken into account
for a complete interpretation of the experimental data. Namely the finite spin polar-
ization $S_y > 0$ at $k_x = 0\,\text{Å}^{-1}$ for both, BiTeI as well as Bi_2Te_2Se, disagrees with ground
state calculations and is thus evidence for a deviation between the spin character
in the initial state and the measured photoelectron spin polarization. An additional
indication for such deviation can be found for the conduction band state of BiTeI as
summarized in Fig. 5.8.

Fig. 5.8 (a) and (b) show the same measurements as already displayed and dis-
cussed before in association with Fig. 5.6 (a) and (b). The measurements were per-
formed with a photon energy of $h\nu = 6\,\text{eV}$ and linearly s- and p-polarized light, where
the light incidence was along k_x and at an angle of $\Theta = 8°$. The result is compared
with a measurement performed with the He I_α-line of a He discharge lamp with
$h\nu = 21.2\,\text{eV}$ and unpolarized light displayed in Fig. 5.8 (c). Here, the light incidence
was at an angle between light beam and sample surface of $\Theta = 22°$ and at $\Phi = 30°$ with
regard to the k_x-axis. The spin polarization S_y along y is displayed in red for positive
and blue for negative spin polarization. In (c) the color scheme additionally encodes the
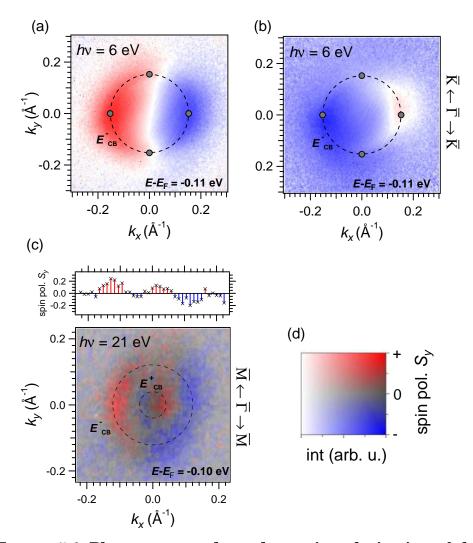
FIGURE 5.8. **Photon energy dependent spin polarization of the conduction band surface state of BiTeI(0001).** (a) and (b) show spin polarization maps at a binding energy of $E - E_F = -110$ meV measured with $h\nu = 6$ eV and s- and p-polarized light, respectively. Light incidence was along k_x at an angle of $\Theta = 8°$ with respect to the sample surface. The data in (c) was measured with $h\nu = 21.2$ eV and unpolarized light at a binding energy $E - E_F = -100$ meV. Here, light incidence was at an angle of $\Theta = 22°$ with respect to the sample surface and at $\Phi = 30°$ with regard to the k_x-axis. In the spin-resolved momentum map the upper and lower branch E_{CB}^+ and E_{CB}^- of the conduction band state are indicated by dashed circles. The upper panel in (c) displays the spin polarization along k_x for $k_y = 0 \overset{\circ}{A}^{-1}$. (d) shows the 2D color scheme for the spin polarization map in (c).

photoemission intensity as described by the 2D color scheme in (d). All measurements in Fig. 5.8 were carried out at the momentum microscope at the Max Planck institute in Halle, the different experimental geometries are due to the different position of the light sources.

One difference between the measurements with $h\nu = 6\,\text{eV}$ and $h\nu = 21.2\,\text{eV}$ is found in the inner branch of the conduction band state E_{CB}^{+}, which is clearly visible for measurements with $h\nu = 21.2\,\text{eV}$ but is not distinguishable for $h\nu = 6\,\text{eV}$. This is very likely due to bulk bands which have a high intensity around the $\bar{\Gamma}$-point at $h\nu = 6\,\text{eV}$ as can be seen for instance in Fig. 5.5. Due to the resulting overlap between bulk and surface state, the upper branch cannot be distinguished and its spin polarization is not detectable. The data measured with $h\nu = 21.2\,\text{eV}$ on the other hand, shows a reversed spin polarization of the lower branch E_{CB}^{-} when compared to the upper branch E_{CB}^{+}. This can be inferred in detail from the spin polarization plot in the upper panel in (c), which shows the spin polarization along k_x at $k_y = 0\,\text{Å}^{-1}$. The spin polarization is reversed at approximately $\pm 0.08\,\text{Å}^{-1}$ and $k_x = 0\,\text{Å}^{-1}$. Whereas the reversal at $k_x = 0\,\text{Å}^{-1}$ is due to the opposite spin polarization of the state at positive and negative k_x, the polarization switch with higher k_x is proof of the opposite spin chirality between upper and lower branch of the Rashba-split state, which is expected for the spin-structure associated with a Rashba-type ground state.

The spin polarization measured with unpolarized light and a photon energy of $h\nu = 21.2\,\text{eV}$ is equal to the spin polarization measured with s-polarized light and $h\nu = 6\,\text{eV}$. A meaningful comparison between the measurements with different photon energies is not straightforward since light polarization as well as the precise experimental geometry differ. However, from Fresnel equations [162], which state that at a metallic surface s-polarized light is predominantly reflected, whereas p-polarized light can be transmitted into the surface, one can assume that inside the sample the light is predominantly p-like for the measurement with $h\nu = 21.2\,\text{eV}$. Under these assumptions, the opposite spin polarization between the measurement with p-polarized light and with unpolarized light is somewhat surprising, since it suggests a possible dependence on the photon energy.

In general a photon energy dependence of the spin polarization is possible, if the photoemission matrix element is taken into account. The up and down spin are coupled to different parts of the spatial wave function, which can have different photon energy dependent photoemission cross sections. A dependence of the spin polarization on photon energy is thus plausible, even if no other parameters of the experimental setup are changed. In fact, modulations of the photoelectron spin polarization have been observed before for circularly polarized light [158] and predicted for layered structures [151, 157]. It must be noted though that here the comparison between different photon

energies is somewhat unclear, due to the changes in the setup. However, the indication of a photon energy dependence raises the question, to what extend the photoelectron spin polarization reflects the initial state spin structure.

In summary, this chapter provides an extensive analysis of the dependence of the photoemission intensity and spin polarization on the polarization direction of the incoming radiation. The first part demonstrates that such dependencies can yield insight into the orbital composition of the electronic states. The in-plane composition of the involved p-orbitals either consists of orbitals aligned mainly tangentially to the electronic state as in case of the upper part of the topological surface state of $Bi_2Te_2Se(0001)$, radially to the electronic state as in the lower Rashba-split band E_L of $PbAg_2$/Ag(111) or of a mixture of both in-plane p-orbitals, as found in the conduction band derived surface state of BiTeI(0001).

The results are used to disentangle the spin-orbital texture of surface states of both, non-topological as well as topological origin. For both cases a strong dependence of the photoelectron spin polarization on the light polarization is observed, indicating a coupling between spin and orbital degree of freedom. Such coupling is, therefore, not characteristic for topological surface states, only, but appears likewise in materials of topologically trivial nature under the influence of strong spin-orbit coupling.

The data additionally reveals a non-negligible influence of the photoemission process. In particular asymmetries in the spectral distribution for p-polarized light occur, which might be caused by an interference between different transition channels during the photoemission process. Finally, the data indicates a photon energy dependence of the photoelectron spin polarization for the case of the layered material BiTeI.

These findings immediately raise the question, how reliable spin-resolved photoemission experiments are and which information on the electronic structure is needed to correctly interpret the measured spin-texture. Is for instance a dependence on photon energy inherent to BiTeI, only, dependent on the layered structure of the material or more generally observable in spin-orbit coupled materials? The following chapter is dedicated to developing a broader picture on the measured spin polarization in different material systems, especially with regard to photon energy dependencies in the photoelectron spin polarization for materials with different characteristics.

6

SPIN-TEXTURE INVERSIONS IN PHOTOEMISSION — THE ROLE OF THE PHOTOEMISSION FINAL STATE

The photoelectron spin in a photoemission experiment can vary considerably and even reverse its sign, when the polarization of the incoming light is changed, as demonstrated in the previous chapter. Such a reversal is induced by the selective excitation of electrons from certain parts — namely the even and odd part in the case of linearly polarized light — of the wave function of the initial state, which are coupled to different spin structures. The photoemission cross sections associated with the individual parts of the wave function generally show a dependence on photon energy. Therefore, also the photoelectron spin polarization can be expected to show variations, when the photon energy is changed. Indications of a photon energy dependence of the photoelectron spin polarization were already discussed for the conduction band surface state of BiTeI(0001), at the end of chapter 5.2.

In order to gain a broader picture of possible changes of the photoelectron spin polarization with photon energy, a detailed study of photon energy dependencies will be presented in the following. In particular, the relation to the material type and its crystal structure will be examined. The first part of this chapter is focused on the topological surface state of Bi_2Te_3(0001), since for the related material Bi_2Se_3(0001) modulations of the photoelectron spin polarization were reported previously [157]. In the second part the Rashba-split surface state of $BiAg_2$/Ag(111) will be analyzed.

The possible photon energy dependence of the photoelectron spin polarization in BiTeI demonstrates the important role of the photoemission process. To understand the spin structure inherent to the initial state wave function, one has to be able to keep apart the initial state spin character and its interplay with the incoming light

and the final state. Only then it becomes possible to unravel the initial state spin-texture. To find possible relations between variations of the spin polarization and the spin-integrated photoemission signal, a thorough analysis of the photoemission cross section, both, experimentally — by a spin-integrated photoemission experiment — and theoretically — in form of a simple model — will be presented. If a clear connection exists, spin-integrated photoemission experiments might already give information on whether the measured spin polarization is robust and mirrors the initial state spin properties.

6.1 Bi_2Te_3 — modulations of the out-of-plane spin polarization

The topological surface state of $Bi_2Te_3(0001)$ exhibits a strong hexagonal deformation as already described briefly in chapter 4. Close to the Dirac point the shape of the state is circular, towards smaller binding energies a hexagonal deformation develops until the shape is star-like with the tips pointing along the $\bar{\Gamma}\bar{M}$-direction [130, 163]. The hexagonal warping can theoretically be described by a third order term in the Hamiltonian $H(\boldsymbol{k})$ as derived from $\boldsymbol{k} \cdot \boldsymbol{p}$ theory with [130]

$$(6.1) \qquad H(\boldsymbol{k}) = E_0 + v_k(k_x \sigma_y - k_y \sigma_x) + \frac{\lambda}{2}(k_+^3 + k_-^3)\sigma_z.$$

Here $E_0 = \boldsymbol{k}^2/(2m^*)$, where m^* is the effective mass and $v_k = v(1 + \alpha \boldsymbol{k}^2)$ is the Dirac velocity. $\sigma_{x,y,z}$ denotes the Pauli matrices and λ is a parameter which scales with the strength of the warping. The third order term $H_w = \frac{\lambda}{2}(k_+^3 + k_-^3)\sigma_z$ is coupled to the out-of-plane spin component via σ_z, therefore, the presence of hexagonal warping is linked to an out-of-plane component $S_z \propto <\sigma_z>$ of the spin polarization in the initial state. Theory predicts this out-of-plane spin polarization to reach up to 60% along $\bar{\Gamma}\bar{K}$, while it is zero along $\bar{\Gamma}\bar{M}$ [130]. If in addition mirror symmetry is taken into account with the mirror plane along $\bar{\Gamma}\bar{M}||k_x$ than the mirror operation $\mathbb{M} : y \to -y$ demands [130]:

$$(6.2) \qquad \mathbb{M} : y \to -y \Longrightarrow k_+ \leftrightarrow -k_-, \sigma_y, \to \sigma_y, \sigma_{x,z} \to -\sigma_{x,z},$$

which results in a reversal of the in-plane spin component S_x, which is oriented perpendicular to the wave vector k_y, as well as the out-of-plane spin component S_z between opposite wave vectors $\pm k_y$ along $\bar{\Gamma}\bar{K}$. Taking into account the threefold rotation symmetry of the crystal, a rotation of the out-of-plane spin polarization from one point along $\bar{\Gamma}\bar{K}$ to the next is required for the ground state spin polarization by symmetry arguments, whereas the in-plane spin component oriented perpendicular to the wave
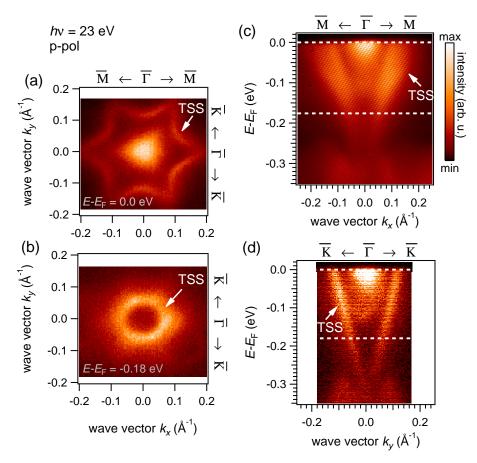
FIGURE 6.1. **Hexagonal deformation in the Fermi surface of Bi$_2$Te$_3$(0001).** (a) and (b) show constant energy cuts of the topological surface state of Bi$_2$Te$_3$(0001) measured with $hv = 23$ eV at $E - E_F = 0$ eV (a) and at $E - E_F = -0.18$ eV (b) with linearly p-polarized light. In (c) and (d) the corresponding ARPES spectra along $\bar{\Gamma}\bar{M}$ and $\bar{\Gamma}\bar{K}$, respectively, are displayed. White arrows highlight the topological surface state (TSS) and white dashed lines mark the energies at which the constant energy maps in (a) and (b) are taken. The direction of light incidence for all measurements was along k_x and at an angle $\Theta = 40°$.

vector has a helical spin structure.

Fig. 6.1 shows ARPES data sets measured at beamline BL 9A of the Hiroshima synchrotron radiation center, which illustrate the hexagonal warping of the topological surface state of Bi$_2$Te$_3$(0001). Fig. (a) and (b) show cuts through the measured band structure at constant energies, namely at the Fermi energy $E - E_F = 0$ eV in (a) and closer to the Dirac point at $E - E_F = -0.18$ eV in (b). The energetic positions of the cuts are additionally highlighted by dashed lines in the photoemission intensity plots of the band structure along $\bar{\Gamma}\bar{M}$ in (c) and along $\bar{\Gamma}\bar{K}$ in (d). The data was measured with

p-polarized light and a photon energy of $hv = 23$ eV. The direction of light incidence
was along $\bar{\Gamma}\bar{M}$ at an angle of $\Theta = 40°$ with regard to the sample surface. The topological
surface state (TSS) is marked by a white arrow. It shows a pronounced star-like struc-
ture at the Fermi energy (a) and exhibits an almost circular shape at lower energies (b).
At the Fermi energy the bulk conduction band is visible and exhibits a high intensity
and a triangular intensity distribution at the $\bar{\Gamma}$ point. The topological surface state
has an almost linear dispersion along $\bar{\Gamma}\bar{K}$ but shows pronounced deformations along
$\bar{\Gamma}\bar{M}$ as evident from Fig. 6.1 (c) and (d). Along $\bar{\Gamma}\bar{M}$ a prominent outward bending of the
state is visible. Furthermore, whereas along $\bar{\Gamma}\bar{K}$ the band is rather distinct, it becomes
increasingly broad towards the Fermi energy along $\bar{\Gamma}\bar{M}$.

Note that, while the shape of the Fermi surface nicely reproduces the expected
shape from the calculation in reference [130], the deformation is an inwards de-
formation along $\bar{\Gamma}\bar{K}$ in the calculation, whereas the experiment shows an outward
deformation along $\bar{\Gamma}\bar{M}$.

Before analyzing possible modulations of the out-of-plane spin component S_z,
measurements of the tangential spin polarization S_y are presented in Fig. 6.2. The
data on $Bi_2Te_3(0001)$ presented here and in the following were obtained at beamlines
BL 9A (c) and BL 9B (a) at the Hiroshima Synchrotron Radiation Center (HiSOR).
At beamline BL 9B the spin polarization of the photoelectrons is detected by a single
channel VLEED-type spin-detector which is sensible to the S_x, S_y and S_z component
depending on target magnetization (compare chapter 3 and reference [83]). In all
spin-resolved measurements on Bi_2Te_3 presented in this section, the direction of light
incidence was along k_x and at an angle $\Theta = 40°$ between photon beam and sample
surface. The setup allows to measure spin-resolved energy distribution curves at a
constant emission angle ϑ, which is regulated by tilting the sample with the rotation
axis parallel to y.

In Fig. 6.2 (a) spin-resolved energy distribution curves measured with p-polarized
light at $hv = 22$ eV in the lower panel and $hv = 28$ eV in the upper panel are displayed.
The left part of (a) shows measurements at negative wave vectors $k_x < 0$ as indicated
by the blue dotted line in the ARPES data plot in (c), whereas the right side presents
the spin polarization at positive wave vectors $k_x > 0$ (orange line in (c)). The ARPES in-
tensity plot in Fig. 6.2 (c) was measured with a photon energy of $hv = 23$ eV and serves
as illustration of the position of the spin-resolved energy distribution curves in (a).
The momentum resolution of the spin-resolved measurement is $\Delta k_x < 0.033\,\mathring{A}^{-1}$ as
represented by the light orange and light blue dotted lines in (c). The spin-resolved
energy distribution curves presented throughout chapter 6.1 have a comparable angu-
lar and accordingly momentum resolution. The curvature of the energy distribution
curve in $\boldsymbol{k}$-space, resulting from the conversion from angles ϑ to $\boldsymbol{k}_{||}$, is neglected in
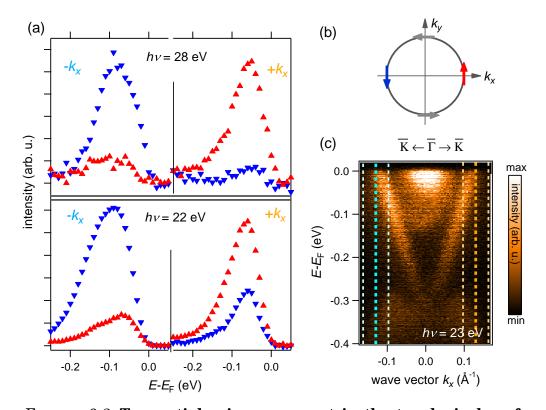Fig. 6.2 (c), since it is not relevant for the probed spin polarization close to the Fermi

FIGURE 6.2. **Tangential spin component in the topological surface state of Bi$_2$Te$_3$(0001).** (a) shows spin-resolved data sets that were obtained at photon energies of $h\nu = 22$ eV (lower panel) and $h\nu = 28$ eV (upper panel). Red and blue color depict the photoemission intensity of electrons with positive and negative spin polarization along the y-axis (tangential spin polarization) as illustrated in the schematic in (b). The spin-resolved energy distribution curves at positive and negative wave vectors are taken along the blue and orange dotted line in the spin-integrated ARPES plot in (c), respectively. Light incidence was along k_x and at an angle of $\Theta = 40°$ between sample surface and light beam. Energy and momentum resolution of the spin-resolved measurements are $\Delta E < 50$ meV and $\Delta k_x < 0.033 \,\mathring{A}^{-1}$, respectively. The momentum resolution is illustrated by thin dashed lines in (c).

energy.

   In the spin-resolved energy distribution curves in Fig. 6.2 (a), red and blue color signify the photoemission intensity of photoelectrons with a spin polarization along the positive or negative y-axis, respectively. For both photon energies at negative wave vectors $k_x < 0$ the blue curve, that is spin-down intensity, shows a much higher intensity than the red curve, therefore, the overall tangential spin polarization S_y of the topological surface state is negative at negative wave vectors. At positive wave vectors, on the other hand, the spin polarization S_y is positive, as can be deduced
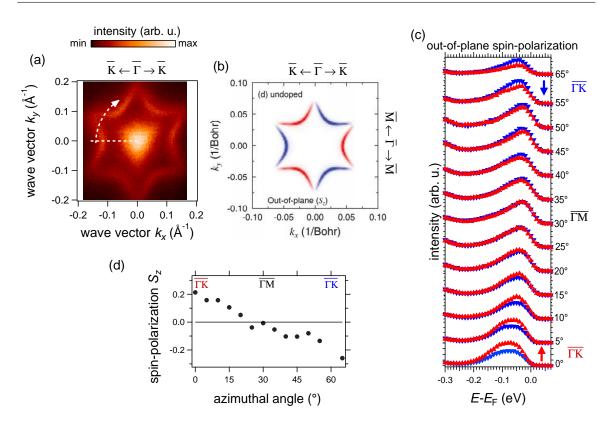
FIGURE 6.3. **Out-of-plane spin polarization in the surface electronic structure of Bi$_2$Te$_3$(0001).** (a) displays the Fermi surface of Bi$_2$Te$_3$ measured with $h\nu = 23$ eV and linearly p-polarized light. A theoretical calculation of the out-of-plane spin polarization in the topological surface state of Bi$_2$Te$_3$(0001) as adapted from [163] is presented in (b). (c) shows spin-resolved energy distribution curves taken at k-points around the Fermi surface from angles of 0° till 65° as indicated by the gray dotted lines in (a). Red and blue denote spin-up and spin-down photoemission intensities. (d) shows a plot of the spin polarization versus azimuthal angle as derived from the measurements in (c). The energy and momentum resolution of the spin-resolved measurements are $\Delta E < 50$ meV and $\Delta k < 0.033 \, \text{\AA}^{-1}$, respectively.

from the larger intensity of the spin-up photoelectrons (red curve). A schematic of the tangential spin component is displayed in Fig. 6.2 (b), where arrows illustrate the spin component aligned tangential to the topological surface state, which is schematically depicted as a circle. The in-plane spin structure, as expected for the ground state from first order $\boldsymbol{k} \cdot \boldsymbol{p}$ theory, is chiral. The measured spin components, which are probed in the experiments, are illustrated by red and blue arrows in (b). The data shown in (a) is, therefore, in agreement with the initial state expectations.

As described before, the strong hexagonal deformation of the topological surface state of Bi$_2$Te$_3$(0001) suggests the existence of an out-of-plane spin component in the initial state [130]. Fig. 6.3 shows a systematic measurement of the out-of-plane spin polarization of the topological surface state of Bi$_2$Te$_3$(0001) at different azimuthal angles, ranging from one point along approximately $\bar{\Gamma}\bar{K}$ to the next. Fig. 6.3 (a) once more shows the Fermi surface, where the star-like feature is the hexagonally deformed topological surface state. The same data was shown before in Fig. 6.1 (a) and described in detail. The measurement was performed with a photon energy of $h\nu = 23$ eV and p-polarized light. The image is turned by 90° compared to Fig. 6.1 (a) for better comparison with the data in Fig. 6.3 (b) and (c). Therefore, light incidence was along the k_y-direction at an angle $\Theta = 40°$ between light beam and sample surface for the constant energy map in Fig. 6.3 (a). The predicted out-of-plane spin component is depicted in Fig. 6.3 (b), where a calculation of the Fermi surface of Bi$_2$Te$_3$(0001) adapted from reference [163] is displayed. Thereby, the out-of-plane spin component S_z pointing along plus and minus z is decoded in red and blue. The shape of the calculated Fermi surface nicely corresponds to the measured one. It also demonstrates the expected switch from positive to negative spin polarization from one to the next point along $\bar{\Gamma}\bar{K}$ as well as a vanishing spin polarization S_z along $\bar{\Gamma}\bar{M}$.

Rotating the sample around its azimuth by angles between 0° and 65°, measurements of the spin polarization in dependence of the crystal direction were performed as indicated by the white dashed line in (a). The resulting spin-resolved energy distribution curves are displayed in Fig. 6.3 (c), where red and blue are the photoemission intensities of photoelectrons that carry spin-up or spin-down projected to S_z, respectively. The respective photon energy was $h\nu = 23$ eV. The azimuthal angle relative to the crystal direction was determined by Fermi surface mapping at 0°, 5° and 55° and additionally monitored by a camera image of the sample after each measurement. Note that the measurements in (a) and (c) were performed at different experimental setups, namely at beamlines BL 9A and BL 9B at HiSOR, respectively, and, therefore, on a different sample surface and experimental geometry.

The relative intensities of the spin-up and spin-down photocurrent vary significantly with the azimuthal angle. At 0°, which is within 5° of the $\bar{\Gamma}\bar{K}$ crystal direction, the spin-up intensity (red) is considerably higher than the spin-down intensity (blue), revealing a positive spin polarization along the z-axis. If the sample is turned by 30°, the spin-resolved measurement is performed at a momentum vector along the $\bar{\Gamma}\bar{M}$-direction. The energy distribution curves at 30° for spin-up and spin-down intensities lie on top of each other, therefore, the spin polarization S_z is zero. At the next momentum vector that lies along $\bar{\Gamma}\bar{K}$ at approximately 60°, there is again a finite spin polarization S_z but here the spin-down intensity has higher intensity, implying an overall negative spin polarization.

The spin polarization S_z as determined from the data in (c) is plotted in Fig. 6.3 (d) for azimuthal angles from $0°$ to $65°$. At approximately $30°$, which corresponds to the $\bar{\Gamma}\bar{M}$-direction, the spin polarization switches sign from positive to negative values. The maximum of the spin polarization is found along the $\bar{\Gamma}\bar{K}$-direction and has values of $|\pm S_z| < 0.3$. The reversal of the out-of-plane spin polarization nicely reproduces the theoretical predictions for the initial state [130, 163] and is comparable to similar measurements performed on $Bi_2Te_3(0001)$ [164]. A similar out-of-plane rotation of the spin polarization was for example also observed along $\bar{\Gamma}\bar{K}$, in the Rashba system Tl/Si(111)-(1×1) [165] as well as in $(\sqrt{3} \times \sqrt{3})$-Au/Ge(111) [166].

At $h\nu = 23\,eV$ the bulk conduction band has a rather high intensity. Therefore, a possible contribution of the bulk conduction band to the measured spin resolved photoemission intensities must be taken into account. If the bulk conduction band is considered to yield photoelectrons that are unpolarized, than a contribution of the bulk might reduce the absolute value of the spin polarization as compared to a measurement without photoemission intensity from the conduction band. In such a scenario the general observation of a spin polarization switch would be trustworthy, while the absolute values of the spin polarization might be decreased. However, if the bulk conduction band yields spin polarized photoelectrons, the situation becomes more complex and the overall observations might be influenced considerably by the bulk state. Therefore, in order to exclude contributions of the bulk state, for each azimuthal angle measured, an additional spin-integrated ARPES experiment was performed to evaluate the exact energy distribution curves along which the spin resolved measurements were performed. This was done for all spin-resolved data shown. From this careful analysis of the data, it is possible to exclude significant contributions of the conduction band to the measured spin polarization.

Up to here, the presented experimental results are in line with theoretical predictions for the initial state of the topological surface state of $Bi_2Te_3(0001)$. The presented data confirms that the state has a rather large tangential spin component, which is robust with varying photon energy, and it exhibits an out-of-plane component that modulates around the Fermi surface. In the following the spin polarization of the topological surface state of Bi_2Te_3 will be analyzed under variation of the light polarization, which, as seen before, can effect the measured spin polarization significantly and can even lead to a reversal of the photoelectron spin as shown in section 5.2.

Fig. 6.4 summarizes the influence of the light polarization on the photoelectron spin polarization of the topological surface state of $Bi_2Te_3(0001)$. In the upper row spin-resolved energy distribution curves of the tangential spin component S_y are presented, whereas the lower row shows measurements of the out-of-plane component S_z. The data was acquired for negative wave vectors along k_x, which corresponds to
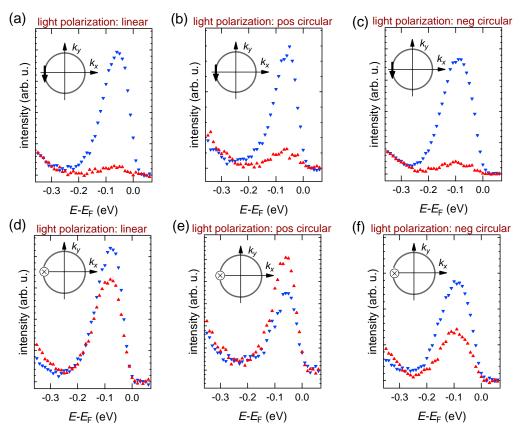
FIGURE 6.4. **Dependence of the spin polarization on light polarization.** The spin-resolved energy distribution curves that are displayed were measured with a photon energy of $h\nu = 26\,\text{eV}$ and different light polarizations. Light incidence was parallel to the k_x-axis and at an angle of $\Theta = 40°$ with respect to the sample surface. The upper row (a)-(c) shows the in-plane tangential spin component, whereas the lower row (d)-(f) illustrates the out-of-plane spin polarization, as depicted in the schematics included in each graph. Red and blue markers signify the respective spin-up and spin-down photoemission intensities. The light polarization was tuned from linear in (a) and (d) to positive circular in (b) and (e) and negative circular in (c) and (f). The energy and momentum resolution of the spin-resolved measurements are $\Delta E < 50\,\text{meV}$ and $\Delta k_x < 0.033\,\text{Å}^{-1}$, respectively.

the $\bar{\Gamma}\bar{K}$-direction, and at an azimuthal angle of $0°$ in correspondence to Fig. 6.3. Red
and blue markers again denote the photoemission intensity of spin-up or spin-down
polarized photoelectrons, respectively. The photon energy was $hv = 26\,\text{eV}$ and the light
polarization was changed from linear p-polarized in (a) and (d) to positive ((b) and (e))
and negative ((c) and (f)) circular polarization. Apart from the light polarization, the
measurement geometry equals that described for Fig. 6.2.

In all three measurements of the tangential spin component, which are displayed
in the upper row of Fig. 6.4, the intensity of spin-down polarized photoelectrons is sig-
nificantly higher than the intensity of spin-up polarized photoelectrons, resulting in an
overall negative tangential spin polarization S_y. More precisely, the spin polarization
is approximately $S_y \approx -0.88$ for linear polarized light, $S_y \approx -0.72$ for positive circular
polarized light and $S_y \approx -0.81$ for negative circular polarization as deduced from the
measurements. The small changes in the absolute spin polarization can result from
experimental uncertainties as for example variations of the precise wave vector k_x at
which the spin resolved energy distribution curve was measured. Furthermore, the
measurements with linear polarized light but different photon energies, which were
shown and discussed in connection with Fig. 6.2, together with the data shown here
demonstrate that for photon energies of $hv = 22\,\text{eV}$, $hv = 23\,\text{eV}$ and $hv = 28\,\text{eV}$, the
photoelectron spin polarization projected to the axis oriented tangential to the surface
state is robust with photon energy as well as light polarization.

In the lower row of Fig. 6.4 measurements of the spin component S_z along the out-
of-plane axis, performed with linear polarized light in (d), positive circular polarized
light in (e) and negative circular polarized light in (f), are presented. Unlike the
tangential spin component, the out-of-plane spin polarization exhibits an apparent
dependence on light polarization. When measured with linear polarized light, it is
negative and its value can be deduced to $S_z \approx -0.15$. The spin polarization switches to
a positive value of approximately $S_z \approx 0.20$, when positive circular light is used, while
it is negative with $S_z \approx -0.35$ for negative circular polarized light.

That the light polarization can have a huge effect on the measured photoelectron
spin polarization was already described in detail for the case of linear p- or s-polarized
light in chapter 5.2 of this work and is in general well known from earlier works
on $Bi_2Se_3(0001)$ [31, 151, 153, 154, 157–159, 167]. The cause can be found in dipole
selection rules that result in a selective excitation of electrons from orbitals of a certain
symmetry, which have particular spin properties, owing to the presence of spin-orbit
coupling. In case of the data shown before, s-polarized light will couple to the uneven
and p-polarized light to the even part of the wave function. Due to this coupling, also
the observed photoelectron spin polarization can vary. Similar dipole selection rules
exist for circular polarized light, which is very likely the reason for the observed switch
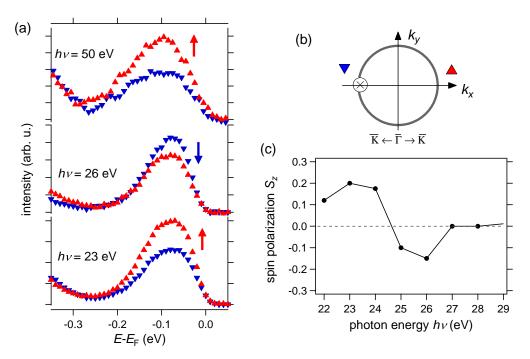of the out-of-plane spin polarization S_z.

FIGURE 6.5. **Photon energy dependent photoelectron spin polarization.** (a) shows spin-resolved energy distribution curves measured with p-polarized light and different photon energies ($h\nu$ = 23 eV, 26 eV and 50 eV). The light was incident along the k_x-axis parallel to $\bar{\Gamma}\bar{K}$ and at an angle of $\Theta = 40°$ with regard to the sample surface. Red and blue markers indicate the spin-up and spin-down photoemission intensity. The measured spin component S_z is oriented along the out-of-plane (z-) axis as indicated in (b). The maximum of the spin polarization as deduced from spin resolved energy distribution curves over a wider range of photon energies is plotted in (c). The resolution of the spin-resolved measurement is $\Delta E < 50$ meV and $\Delta k_x < 0.033$ Å^{-1}.

The out-of-plane spin polarization measured with linear p-polarized light is negative in Fig. 6.4 (d), where the photon energy is $h\nu = 26$ eV and the sample is aligned with $\bar{\Gamma}\bar{K}$ along k_x. Earlier in this chapter, in connection with Fig. 6.3, measurements with a photon energy of $h\nu = 23$ eV were presented, where the spin polarization S_z is positive for azimuthal angles of 0° and, therefore, for the same sample alignment. This suggests a reversal of the out-of-plane spin polarization with photon energy. The spin-resolved energy distribution curves measured with $h\nu = 23$ eV and $h\nu = 26$ eV are displayed once more in Fig. 6.5 (a), together with a spin-resolved data set obtained with $h\nu = 50$ eV. The measurements were performed at negative wave vectors k_x along $\bar{\Gamma}\bar{K}$ as indicated in the schematic in (b).

Evidently, the out-of-plane spin polarization of the measured photoelectrons shows

79

a sign switch between $h\nu = 23\,\text{eV}$ and $h\nu = 26\,\text{eV}$ and is reversed once more for $h\nu = 50\,\text{eV}$. To gain a more detailed understanding of the dependence of the photoelectron spin polarization on photon energy, the measured out-of-plane spin polarization is plotted for photon energies between $h\nu = 22\,\text{eV}$ and $h\nu = 28\,\text{eV}$ in Fig. 6.5 (c). In the measured photon energy range the spin polarization exhibits an almost sinusoidal variation with a sign switch between $h\nu = 24\,\text{eV}$ and $h\nu = 25\,\text{eV}$ and at least one more sign switch at or above $h\nu = 28\,\text{eV}$. The maxima of the absolute spin polarization amount to approximately $|S_z| \approx 0.2$ and can be found for $h\nu = 23\,\text{eV}$ and $h\nu = 26\,\text{eV}$. The photoelectron spin polarization was not measured in the presented experiment for photon energies between $h\nu = 28\,\text{eV}$ and $h\nu = 50\,\text{eV}$, therefore, while there must be at least one more sign switch to positive spin polarization, it is not possible to ascertain, whether the spin polarization continues to modulate or becomes more robust with higher photon energies.

In principle, a photon energy dependence as observed here can occur under the influence of spin-orbit coupling, when the different spin parts of the wave function couple to different spatial parts of the wave function, which have a photon energy dependent photoemission cross section. In order to gain an understanding of the magnitude of variations of the cross sections with different photon energies it can be of interest to investigate possible variations in the spin-integrated photoemission intensities.

The influence of the photon energy on the photoemission cross section is illuminated in Fig. 6.6, which shows a comparison of the Fermi surface of $Bi_2Te_3(0001)$ measured with two different photon energies, namely $h\nu = 23\,\text{eV}$ in (a) and $h\nu = 28\,\text{eV}$ in (b). The data shown in (a) was discussed before in connection with Figs. 6.1 and 6.3, the data in Fig. 6.6 (b) was acquired at the same experimental setup and sample alignment. Light incidence was along the k_x-axis, which is aligned parallel to $\bar{\Gamma}\bar{K}$, and the light was p-polarized. In both measurements the star-like intensity distribution of the topological surface state is clearly visible. It is additionally highlighted by dashed white lines, which serve as guides to the eyes. Furthermore, the tips of the star are marked with dots and labeled k_1 to k_6 to simplify the following discussion.

The intensity distribution is approximately sixfold for $h\nu = 23\,\text{eV}$ in Fig. 6.6 (a), whereas in (b) a threefold modulation of the intensity is predominant. More precisely, at the tips of the star-like structure at points k_1 to k_6 the intensity is always at a minimum in (a). For a photon energy of $h\nu = 28\,\text{eV}$ on the other hand at points k_1, k_3 and k_5 (blue dots) the photoemission intensity is high, at points k_2, k_4 and k_6 (gray dots), however, there is much less intensity and the tips of the star are indistinguishable. Therefore, the symmetry of the intensity distribution switches from sixfold to threefold, when the photon energy is changed.

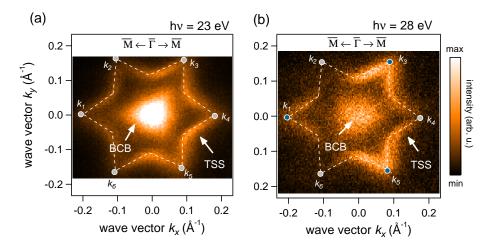The threefold symmetry in Fig. 6.6 (b) mirrors the threefold symmetry of the out-of-

FIGURE 6.6. **Photon energy dependent photoemission intensity distribution.** Fermi surface maps of Bi$_2$Te$_3$(0001) are displayed for a photon energy of $h\nu = 23$ eV in (a) and $h\nu = 28$ eV in (b). In both cases p-polarized light was used. The direction of light incidence was along k_x at an angle of $\Theta = 40°$ between incoming light and sample surface. The topological surface state (TSS) and bulk conduction band (BCB) are labeled and marked by arrows, the TSS is additionally highlighted by dashed lines that serve as guides to the eyes. The vertices of the hexagonally deformed TSS are labeled k_{1-6} and marked by gray and and blue dots to highlight the threefold and sixfold photoemission intensity distribution.

plane spin polarization. The dependence of the intensity distribution on photon energy might, therefore, be closely connected to the changes in the observed spin polarization. If at $h\nu = 23$ eV and $h\nu = 28$ eV different spatial parts of the wave function dominate the photocurrent, leading to a threefold or sixfold symmetry at the two different photon energies, respectively, and these two wave functions are coupled to opposite spin, the observed variations of spin-resolved and spin-integrated photoemission signals might have the same origin.

In the case of the topological insulator Bi$_2$Se$_3$(0001), a detailed investigation of the spin polarization and its photon energy dependence was performed in references [151, 157]. Thereby, for an experimental alignment equal to the presented case, radial components as well as a photon energy dependence of the measured spin polarization were observed when p-polarized light was used. The measured spin polarization variations with photon energy were explained by the layer dependent orbital structure of the material and a consequential interference between electrons from different layers and orbitals [151]. The observed photon energy dependence was explained in the framework of this model by a k_z-dependent term which accounts for the different optical paths for photoelectrons from different atomic layers [151, 157, 168]. This

proposed interference model is, therefore, only valid for materials that exhibit a layered structure with a layer dependent orbital composition as found in the topological insulator Bi_2Se_3, but also in the material Bi_2Te_3 investigated here. It is thus possible that the photon energy dependence of the out-of-plane spin component described in the present chapter has a similar origin.

However, as an immediate implication of a layer dependent interference model as introduced in reference [151, 157, 168], which explains photon energy dependencies of the spin polarization solely by a depth dependence, similar spin polarization effects should not appear in case of a simpler quasi two-dimensional structure. Therefore, to understand the cause of the spin polarization reversal, it is useful, to expand the investigation to different material types. Up to here, the spin polarization was in fact only analyzed for layered materials. In the following, the discussion will be extended to materials with a simpler two-dimensional structure.

6.2 $BiAg_2$/Ag(111) — Photon energy dependence in spin-resolved and spin-integrated photoemission

The presented experiments on the spin-resolved electronic structure of Bi_2Te_3(0001) reveal considerable photon energy dependent variations of the photoelectron spin polarization. According to [157], similar changes appear in the isostructural topological insulator Bi_2Se_3(0001) as a result of the layer-dependent orbital structure, which can lead to interference effects between electrons from different atomic layers and orbitals. The layer-interference model as introduced in reference [157] is exclusively valid, when at least two layers with different spin- and orbital textures take part in the photoemission process. Whether a layered structure is indeed required to observe spin polarization reversals can be investigated, if an interference of the spin-orbital textures from different layers can be excluded, as for instance in a material with strictly two-dimensional electronic states and, ideally, a simple orbital structure. Surface alloys like $BiAg_2$/Ag(111) and $PbAg_2$/Ag(111) fulfill such conditions and are thus ideal materials for a case study of the photon energy dependent photoelectron spin polarization of a quasi two-dimensional electron gas. Consequently, spin-resolved photoemission experiments on the surface states of $BiAg_2$/Ag(111) and $PbAg_2$/Ag(111) will be presented in the following.
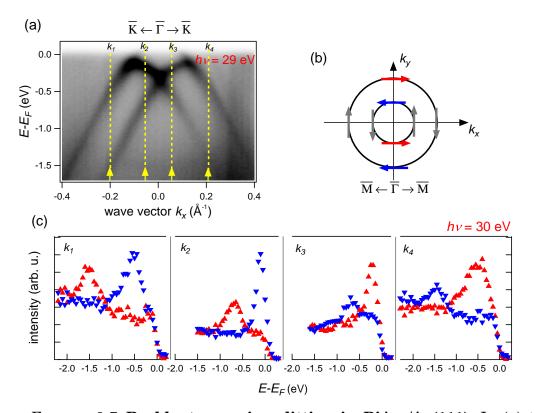
FIGURE 6.7. **Rashba-type spin-splitting in BiAg$_2$/Ag(111).** In (a) the
angle-resolved photoemission intensity along the $\bar{\Gamma}\bar{K}$-direction of the
surface electronic structure of BiAg$_2$/Ag(111) is displayed. It was mea-
sured with p-polarized light and a photon energy of $h\nu = 29$ eV. Yellow
arrows and dashed lines mark the approximate positions k_{1-4}, where
the spin-resolved energy distribution curves shown in (c) were measured.
The spin-resolved data was obtained with a photon energy of $h\nu = 30$ eV
and along k_y as schematically shown in (b). For all measurements the
direction of light incidence was along k_x which corresponds to $\bar{\Gamma}\bar{K}$ for
the spin-integrated data in (a) and to $\bar{\Gamma}\bar{M}$ for the spin-resolved data in
(b) and (c) and at an angle of 17° with respect to the sample surface.
The energy and angular resolution of the spin-resolved measurement is
approximately $\Delta E = 50$ meV and $\Delta\vartheta = 3°$, respectively.

83

Spin-resolved photoelectron spectroscopy on the surface electronic structure of
$BiAg_2/Ag(111)$ was performed at beamline i3 at Max-laboratories in Lund employing
a single channel Mott-type spin detector. As an example, spin-resolved measurements
of the tangential spin component of the surface state E_L of $BiAg_2$ are presented
in Fig. 6.7. The spin-resolved data was acquired with p-polarized light at a photon
energy of $h\nu = 30\,\mathrm{eV}$ and light incidence along k_x and at an angle $\Theta = 17°$ with
respect to the sample surface. The energy and angular resolution of the spin-resolved
experiments shown here and in the following is approximately $\Delta E = 50\,\mathrm{meV}$ and
$\Delta\vartheta = 3°$, respectively. The sample was aligned with $\bar{\Gamma}\bar{M}$ along the x-axis. In order to
investigate the tangential spin polarization at a particular wave vector along $\bar{\Gamma}\bar{K}$, the
sample had to be tilted by up to $5°$ around the rotation axis x and the photoelectron
spin polarization S_x parallel to the k_x-axis was measured. Fig. 6.7 (b) schematically
illustrates the tangentially aligned chiral spin structures (arrows) of the upper and
lower branch $E_L^{+/-}$ of the Rashba-split state as expected from the Rashba-Bychkov
model. The spin components at the approximate positions in $\boldsymbol{k}$-space that were actually
measured in the experiment are especially highlighted by red and blue arrows. The
resulting spin-resolved data is presented in Fig. 6.7 (c) for four different wave vectors
k_{1-4}, which are indicated by yellow arrows and dashed lines in the band structure
along $\bar{\Gamma}\bar{K}$ in Fig. 6.7 (a). The spin-resolved energy distribution curves show two peaks,
which correspond to the upper and lower branch E_L^+ and E_L^-, respectively. For negative
wave vectors k_1 and k_2 the intensity of spin-down electrons (blue markers) dominates
for the upper branch E_L^+, which constitutes the peak closer to the Fermi energy
$E - E_F = 0\,\mathrm{eV}$. For the lower branch E_L^-, on the other hand, the overall photoemission
intensity stems predominately from spin-up electrons (red markers). For positive wave
vectors k_3 and k_4 the situation is reversed and the spin polarization S_x is positive
(spin-up) for the upper branch E_L^+ and negative (spin-down) for the lower branch E_L^-.
The measured spin polarization thus reflects the spin-splitting expected for the surface
state from a simple Rashba model.

When the photon energy is changed, however, the tangential spin polarization
changes significantly. This is demonstrated in Fig 6.8, where spin-resolved energy
distribution curves measured along $\bar{\Gamma}\bar{K}$ are displayed in (a) for positive wave vectors
$k_y < 0$ and photon energies of $h\nu = 20\,\mathrm{eV}$, $22\,\mathrm{eV}$, $24\,\mathrm{eV}$, $26\,\mathrm{eV}$ and $30\,\mathrm{eV}$. As before, the
red and blue markers indicate the intensity of electrons with spin-up or spin-down
projected to the tangential component. Each energy distribution curve shows two
peaks, which correspond to the upper and lower branch of the surface state E_L. The
peak closer to the Fermi energy is the upper branch E_L^+, whereas the one at lower
energies $E - E_F$ stems from the lower branch E_L^-. The data was acquired at slightly
different wave vectors k_y, which leads to varying peak positions for the different
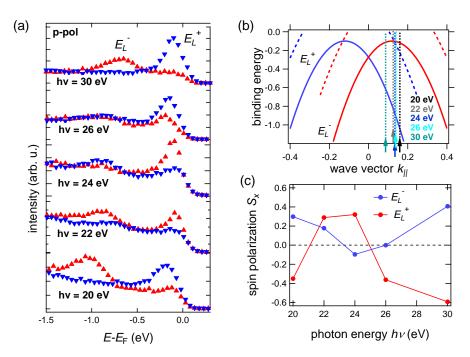energies. The approximate momentum vectors for each measurement are marked in

FIGURE 6.8. **Photon energy dependent spin polarization in BiAg$_2$/Ag(111).** (a) shows spin-resolved energy distribution curves measured at different photon energies and at positive wave vectors as indicated by dotted lines in the schematic in (b). For the spin-resolved measurements the sample was tilted by 2-5° and the spin component S_x at wave vectors k_y was measured. Light incidence was along k_x and at an angle of $\Theta = 17°$ between light beam and sample surface. The measured spin polarization in dependence of the photon energy is summarized in (c) for the upper branch E_L^+ (red markers) and the lower branch E_L^- (blue markers). The resolution of the spin-resolved experiment is approximately $\Delta E = 50\,\mathrm{meV}$ and $\Delta\vartheta = 3°$.

the schematic of the two bands in Fig. 6.8 (b) by colored arrows and dotted lines. Here, blue and red signify the expected opposite spin polarization aligned tangentially to the state.

The photon energy dependence of the spin polarization of the upper branch E_L^+ can be inferred from the peak closer to the Fermi level. At $h\nu = 20\,\mathrm{eV}$ it shows a clear dominance of photoelectrons with a negative spin polarization S_x, as can be deduced from the fact that the blue curve has a significantly higher intensity than the red curve. For $h\nu = 22\,\mathrm{eV}$, however, the tangential spin polarization of the upper branch is positive, since the intensity is higher for the spin-up photoelectron intensity (red). The situation is reversed once more at $h\nu = 26\,\mathrm{eV}$, where the spin polarization S_x is again negative. It remains negative up to $h\nu = 30\,\mathrm{eV}$.

The lower branch E_L^- shows a similar spin polarization reversal, here, however, it

occurs at different photon energies. More precisely, the spin polarization of the lower branch is positive for $h\nu = 20\,\mathrm{eV}$, $h\nu = 22\,\mathrm{eV}$ as well as for $h\nu = 30\,\mathrm{eV}$ and negative for $h\nu = 24\,\mathrm{eV}$. For a photon energy of $h\nu = 26\,\mathrm{eV}$ the overall spin polarization of the photoelectrons from the lower branch is close to zero, since it has the same intensity for both, the photoemission intensity of electrons with spin-down with respect to S_x as well as the photoemission intensity from spin-up electrons.

A quantitative analysis of the photoelectron spin polarization is shown in Fig. 6.8 (c), which summarizes the spin polarization dependence on photon energy. The spin polarization of the upper branch E_L^+ is displayed in red, while the spin polarization of the lower branch E_L^- is shown in blue. Apparently, for both branches a sign switch of the tangential spin polarization occurs, as seen already in (a). The first photoelectron spin reversal takes place between $h\nu = 20\,\mathrm{eV}$ and $22\,\mathrm{eV}$ for the upper branch E_L^+ (red) and between $h\nu = 22\,\mathrm{eV}$ and $h\nu = 24\,\mathrm{eV}$ for the lower branch E_L^-. For both branches the spin polarization switches back between $h\nu = 24\,\mathrm{eV}$ and $h\nu = 26\,\mathrm{eV}$. Thus, the spin polarization reversal occurs at different photon energies for the two branches of the surface state. At $h\nu = 22\,\mathrm{eV}$ they even show an equal sign of the tangential spin polarization of the photoelectrons. At the wave vectors, where the spin polarization was measured, the upper surface state E_U^- could in principle contribute to the measured spin polarization of the branch E_L^+. The spin polarization data from the lower branch E_L^-, however, demonstrates that a spin reversal happens independent of the influence of the second surface state. The spin-resolved experiment, therefore, reveals a significant dependence of the photoelectron spin polarization on photon energy for the surface state E_L.

Unlike the case of the topological surface state of the layered topological insulator $Bi_2Te_3(0001)$, the spin polarization reversal in the band structure of $BiAg_2/Ag(111)$ can not be explained by a layer dependent orbital structure of the material. This immediately implies that a dependence of the photoelectron spin polarization on photon energy is not specific for layered materials or topological insulators but a more general effect. It also demonstrates that the measured spin does not directly mirror the initial state spin polarization, but varies due to the photoemission process, which obviously plays a non-negligible role. In general, a photon energy dependence of the measured spin polarization can be explained by a photon energy dependence of the photoemission cross section. More precisely, if a different spin-structure couples to different parts of the spatial wave function with different photon energy dependent cross sections, also the measured spin polarization can depend on the photon energy. This was already shortly discussed for the topological surface state of $Bi_2Te_3(0001)$, where the spin polarization reversal observed in the out-of-plane spin S_z of the photoelectrons was found to be accompanied by variations of the photoemission intensity. These intensity modulations can be interpreted as direct signature of the photon

energy dependence of the photoemission cross section. Therefore, to understand the
origin of the observed photoelectron spin polarization reversals in both materials, it
can be helpful to investigate the dependence on photon energy of the spin-integrated
photoemission intensity. In the following, a thorough examination of the photocurrent
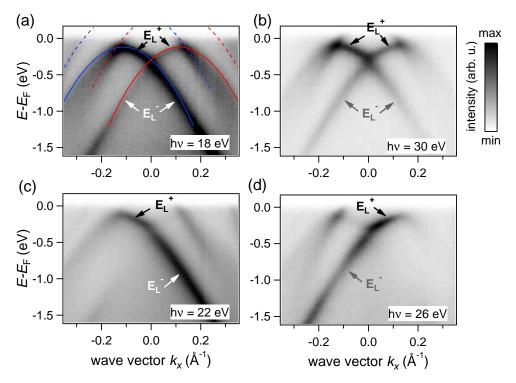from the surface states of BiAg$_2$/Ag(111) will be presented.

FIGURE 6.9. **Photon energy dependent intensity distribution in the
surface bands of BiAg$_2$/Ag(111).** ARPES intensity plots were mea-
sured at different photon energies: $h\nu = 18$ eV in (a), 30 eV in (b), 22 eV
in (c) and 26 eV in (d). The light was p-polarized and light incidence was
along k_x at an angle of $\Theta = 17°$ with respect to the sample surface. The
two branches of the Rashba-split surface state E_L^+ and E_L^- of the occupied
band are marked by arrows. The red and blue parabolic lines in (a) serve
as guides to the eyes and indicate the relative spin polarizations as ex-
pected from a simple Rashba model. Dashed lines indicate the dispersion
of the upper surface state E_U.

In order to investigate the dependence of the photoemission cross section on
photon energy, ARPES was performed for different photon energies. The complete
set of measurements taken along $\bar{\Gamma}\bar{M}$ covers all (integer) photon energies between
$h\nu = 16$ eV and $h\nu = 31$ eV. A subset of the measurements is displayed in Fig. 6.9,
namely for photon energies of $h\nu = 18$ eV in (a), 30 eV in (b), 22 eV in (c) and 26 eV in

(d). These energies cover the complete energy range, in which modulations of the spin polarization were observed. In (a) and (b) the situation for photon energies below and above the photoelectron spin reversal are shown. The main feature in the measured spectral function is the surface state E_L, which is clearly distinguishable in the band structure, indicated by solid lines in (a), and labeled with E_L^+ and E_L^- for the upper and lower branch. In addition, part of the unoccupied band E_U is visible and marked by dashed lines in (a).

Both measurements in (a) and (b), the one below the spin polarization reversal at $h\nu = 18\,\text{eV}$ as well as the one above it with $h\nu = 30\,\text{eV}$, show a more or less symmetric intensity distribution. Close to the photon energies, at which the spin polarization of the photoelectrons undergoes a reversal, however, the photoemission intensity distribution is rather asymmetric as can be seen in the ARPES intensity plots in (c) and (d), where photon energies of $h\nu = 22\,\text{eV}$ and $h\nu = 26\,\text{eV}$ were used. The band E_L can be described as two parabolas, which are shifted in momentum with respect to each other. In Fig. 6.9 (a) this is indicated by the two parabolic lines, which are plotted on top of the ARPES data. Blue and red signify opposite spin character with respect to the tangential spin component as expected from a simple Rashba model. For a photon energy of $h\nu = 22\,\text{eV}$ in (c) the left parabolic band has high intensity, while the right parabola has almost zero photoemission intensity. Interestingly, also for the band above the Fermi energy, the photoemission intensity of the branch E_U^- is high at positive wave vectors but goes to zero at negative wave vectors k_x. For $h\nu = 26\,\text{eV}$ in (d), on the other hand, the photoemission intensity of the band E_L is high for the right parabola but goes to zero for the left one. Again for the upper band E_U, a similar asymmetry of the intensity distribution can be observed, where the left part of the lower branch of E_U is clearly observed, whereas the right part shows no intensity. The photoemission intensity distribution thus varies significantly in the energy range between $h\nu = 18\,\text{eV}$ and $h\nu = 30\,\text{eV}$, where also significant changes of the photoelectron spin polarization arise.

A quantitative analysis of the photon energy dependence of the photoemission intensity is presented in Fig 6.10. From ARPES measurements performed at different photon energies, energy distribution curves at equal wave vectors were extracted. As an example the resulting intensity distributions at $k_x = -0.05\,\text{Å}^{-1}$ are displayed in (a). In Fig. 6.10 (b), which shows an ARPES intensity plot along $\bar{\Gamma}\bar{\text{M}}$ measured with a photon energy of $h\nu = 30\,\text{eV}$ and p-polarized light, the position of the energy distribution curves is indicated by a black dotted line that intersects the two branches of the surface state. The red and blue dashed parabolas serve as guides to the eyes for the two branches of the state with opposite tangentially aligned intrinsic spin character.

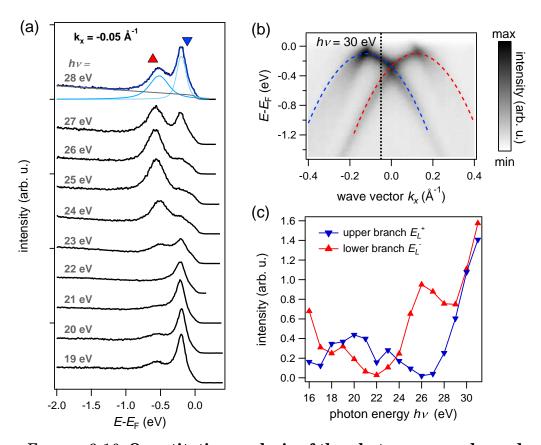The resulting energy distribution curves are shown as black lines in (a) for photon

FIGURE 6.10. **Quantitative analysis of the photon energy dependent photocurrent.** (a) shows energy distribution curves obtained at a constant wave vector $k_x = -0.05\,\text{Å}^{-1}$ for photon energies between $h\nu = 19\,\text{eV}$ and $28\,\text{eV}$. The position of the energy distribution curves is illustrated by the black dotted line in the ARPES intensity plot in (b), which was measured at a photon energy of $h\nu = 30\,\text{eV}$. The light blue curves in (a) shown exemplarily for $h\nu = 28\,\text{eV}$ are Voigt line profiles fitted to the experimental data (black curves), the Fermi-Dirac distribution is shown in gray, the sum of the fits in blue. Intensities extracted from the Voigt line profiles are plotted for the upper (blue markers) and lower (red markers) branch in (c). The data was measured with light incidence along k_x and at an angle $\Theta = 17°$ with respect to the sample surface.

energies between $h\nu = 19\,\text{eV}$ and $h\nu = 28\,\text{eV}$, covering the photon energy range, where the strong intensity modulations take place. Two intensity peaks are distinctively visible for instance for a photon energy of $h\nu = 28\,\text{eV}$. The peak closer to the Fermi energy stems from the upper branch E_L^+, the second peak at approximately $E - E_F = -0.6\,\text{eV}$ stems from the lower branch E_L^- of the Rashba-split band. Since the two branches have opposite spin character, the two peaks are marked by a blue (upper branch E_L^+) and red (lower branch E_L^-) triangle and will for now be termed "'spin-

down"'- and "'spin-up"'- signal for convenience. With decreasing photon energies the intensity distribution of the two peaks changes significantly. At $h\nu = 26\,\text{eV}$, for instance, the upper branch E_L^+ has very low intensity, whereas at $h\nu = 22\,\text{eV}$ the signal from the lower branch E_L^- is indistinguishable. This confirms the intensity variations with photon energy in the ARPES intensity plots, which were described above.

In order to extract the photoemission intensities the energy distribution curves were normalized at energies $E - E_F \approx -1.5\,\text{eV}$, where no significant intensity from the band structure is visible. The curves can be described by two Voigt line profiles and a Fermi-Dirac distribution with linear background. For the data taken with $h\nu = 28\,\text{eV}$ the resulting Voigt line profiles are plotted as light blue lines, the Fermi-Dirac distribution is displayed in gray and the sum of the fit is shown as dark blue line. The peak intensities were extracted from the Voigt peak areas for photon energies between $h\nu = 16\,\text{eV}$ and $h\nu = 30\,\text{eV}$ and are displayed in Fig. 6.10 (c). Two main observations can be made from the photon energy dependence of the intensities. The first one, as already seen and described in connection with the data before, is an apparent shift between the overall behavior of the intensities with photon energy of the "'spin-up"'- and "'spin-down"'-branch. This is primarily visible in the positions of the intensity minima which lie at $h\nu = 22\,\text{eV}$ and $h\nu = 26\,\text{eV}$ for the lower and upper branch, respectively. The second observation is the fact that the intensity actually goes to zero, demonstrating a complete suppression of the photoemission intensity.

The different photoemission intensities at positive and negative wave vectors can be interpreted as a signature of a $\boldsymbol{k}$-dependence of the photoemission cross section. To analyze this dependence more thoroughly, the measured intensity modulations are shown for the lower branch E_L^- of the occupied Rashba-split surface state in Fig. 6.11 for different wave vectors k_x. The intensities were extracted from Voigt line profiles fitted to energy distribution curves in the same manner as described above in connection with Fig. 6.10. The different colors indicate different wave vectors k_x between $|k_x| = 0\,\text{Å}^{-1}$ and $|k_x| = 0.2\,\text{Å}^{-1}$ as labeled above the graph. For each wave vector the analysis of the peak intensities was performed for photon energies between $h\nu = 16\,\text{eV}$ and $h\nu = 30\,\text{eV}$. The resulting intensity vs photon energy curves are plotted separately for negative and positive wave vectors in (a) and (b), respectively.

From a first glance, one can say that the intensity distributions show the overall same trend in the photon energy dependence for all negative wave vectors displayed in (a). The same can be said, considered separately, for all positive wave vectors in (b). For negative wave vectors one local intensity minimum appears at $h\nu \approx 22\,\text{eV}$ as mentioned several times before. But also at $h\nu \approx 29\,\text{eV}$ a second local intensity minimum is found. Whereas the overall trend of the photon energy dependence is the same, small differences appear with varying wave vectors. With decreasing absolute wave vector $|k_x|$ the minimum at $h\nu \approx 29\,\text{eV}$ is positioned at decreasing photon energies $h\nu$. At
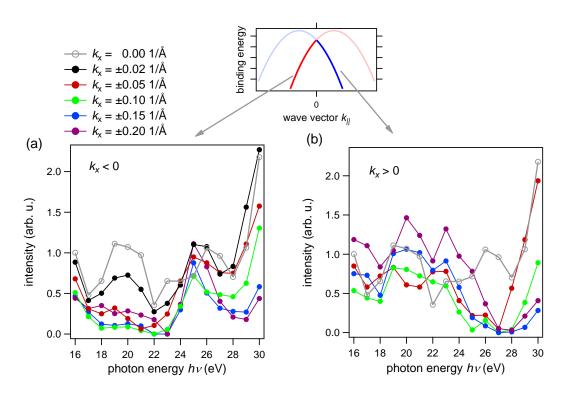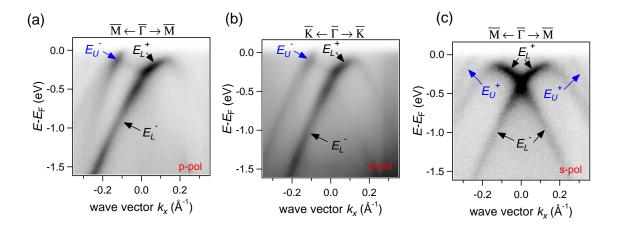
FIGURE 6.11. **Dependence of the photocurrent on the wave vector.** (a) and (b) display photoemission intensity distributions in dependence of the photon energy $h\nu$. The photoemission intensities were extracted from ARPES data sets measured with light incidence parallel to k_x and at an angle $\Theta = 17°$ with respect to the sample surface. The intensities were determined from Voigt line profiles at photon energies from $h\nu = 16$ eV to $h\nu = 30$ eV. The different colors represent different wave vectors k_x between $k_x = \pm 0.20\,\text{Å}^{-1}$. In (a) intensities at negative wave vectors are displayed, while (b) shows the intensities at positive wave vectors. This is illustrated by the inset on top of the graphs.
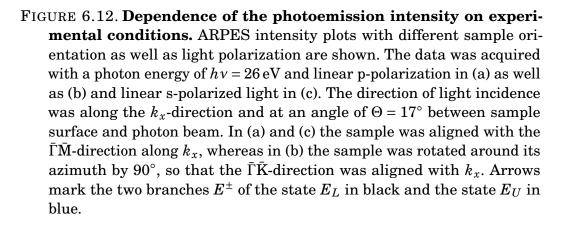
the same time the minimum intensity increases at smaller wave vectors $|k_x|$. The second intensity minimum at $h\nu \approx 22$ eV similarly becomes slightly less pronounced at smaller absolute wave vectors, namely between $k_x > -0.05\,\text{Å}^{-1}$ and $k_x < 0$, but has zero intensity for wave vectors $k_x < -0.05\,\text{Å}^{-1}$.

The photoemission intensities in dependence of photon energy for positive wave vectors show only one distinct minimum, which is found at approximately $h\nu = 27$ eV. For all positive wave vectors $k_x > 0$ that were analyzed the intensity goes to zero, indicating a complete extinction of the branch at certain photon energies. Again, small changes of the overall intensity distribution at different wave vectors can be found, apparent for instance in an increase in intensity with increasing wave vector at $h\nu \approx 20$ eV.

A quite interesting case is the situation at the $\bar{\Gamma}$ point ($k_x = 0$). The intensity distribution at $k_x = 0$ is displayed with gray lines and hollow dots in (a) as well as (b). Clearly the intensity never drops to zero at $k_x = 0$, thus, there is no extinction of both branches at the same photon energy at $\bar{\Gamma}$. Moreover, for photon energies, where either the spin-up or the spin-down branch becomes zero, the intensity at $k_x = 0$ roughly equals the intensity of the respective opposite branch at small absolute wave vectors $|k_x|$. It thus seems that the spin-up or spin-down parabola are extinguished separately. This observation is quite interesting, since at the high symmetry point $k = \bar{\Gamma}$ there is no immediate reason, why the two branches should behave differently. At the $\bar{\Gamma}$ point the surface state is spin degenerate, therefore, the two branches with $E(k_x, \uparrow)$ and $E(-k_x, \downarrow)$ have the same binding energy and wave vector $E(k_x = 0, \uparrow) = E(-k_x = 0, \downarrow)$. They still differ in their intrinsic spin polarization, implying that the spin might play a role in the selective extinction of the two branches.

FIGURE 6.12. **Dependence of the photoemission intensity on experimental conditions.** ARPES intensity plots with different sample orientation as well as light polarization are shown. The data was acquired with a photon energy of $h\nu = 26\,\text{eV}$ and linear p-polarization in (a) as well as (b) and linear s-polarized light in (c). The direction of light incidence was along the k_x-direction and at an angle of $\Theta = 17°$ between sample surface and photon beam. In (a) and (c) the sample was aligned with the $\bar{\Gamma}\bar{M}$-direction along k_x, whereas in (b) the sample was rotated around its azimuth by 90°, so that the $\bar{\Gamma}\bar{K}$-direction was aligned with k_x. Arrows mark the two branches $E^{\pm}$ of the state E_L in black and the state E_U in blue.

Before discussing possible origins of the observed photon energy dependence, it is worthwhile to take a look at the influence of the exact experimental conditions, in particular the light polarization and sample alignment. To this end, three spectra

measured with a photon energy of $h\nu = 26\,\text{eV}$ but slight changes in the measurement geometry are presented in Fig. 6.12. In (a) the same data as already shown in Fig. 6.9 (d) is displayed. For the measurement in (b) the sample was rotated by 90° around its azimuth. Therefore, in (a) the sample was oriented with $\bar{\Gamma}\bar{\text{M}}$ along k_x whereas in (b) the $\bar{\Gamma}\bar{\text{K}}$-direction lies along k_x. The light was p-polarized in both cases.

The photoemission intensity distribution of the two ARPES data sets is nearly the same. Independent of the crystal direction the right parabola shows enhanced intensity compared to the left one. Also for the upper state E_U^- only the left branch is visible. The observed intensity asymmetries are thus independent of the crystal direction and it is valid to assume a more or less isotropic band structure concerning the observed asymmetry effect.

The ARPES data plot shown in (c) was again measured at a crystal oriented with $\bar{\Gamma}\bar{\text{M}}$ along k_x, equal to the data in (a). The light polarization, however, was changed from p-polarized in (a) to s-polarized in (c). Clearly, when measured with s-polarized light, the photoemission intensity distribution is completely symmetric, and the asymmetry effect can only be observed with p-polarized light. In fact, the relation between the orientation of the vector field $\mathbf{A}$ of the incoming radiation and the mirror plane does not allow an asymmetric distribution of the spectral weight for s-polarization, since the overall symmetry is not broken.

In summary, we observe an asymmetric distribution of the photoemission intensity of the surface band structure of BiAg$_2$/Ag(111), which strongly depends on photon energy $h\nu$. The asymmetry seems to favor either bands of nominally spin-up character $+S_y$ or spin-down character $-S_y$, depending on photon energy, but almost disappears for photon energies below $h\nu = 18\,\text{eV}$ and above $h\nu = 29\,\text{eV}$. The different behavior of spin-up and spin-down branch manifests itself in a dependence of the photoemission intensity on the wave vector k_x. The observed asymmetries occur along $\bar{\Gamma}\bar{\text{K}}$ as well as $\bar{\Gamma}\bar{\text{M}}$ albeit for p-polarized light, only. In the same photon energy range a reversal of the photoelectron spin polarization S_x measured at wave vectors $k_y \neq 0$ along $k_x = 0$ can be observed.

A dependence of the photoemission intensity on photon energy is often explained in a hand-waving manner by effects from the photoemission matrix element $D_{f,i}$, given by the relationship $I_{PES} \propto |D_{f,i}|^2 \cdot \delta(E_f - E_i - h\nu)$. Matrix element effects are known to lead to strong variations and possibly even a complete suppression of the photoemission intensity [108, 169–171]. The matrix element depends on the experimental geometry, since it contains the vector field $\boldsymbol{A}$ of the light and the momentum operator $\boldsymbol{p}$, and is responsible for the photon energy dependence of the photocurrent, due to the structure of the final state wave function. Very often, the final state is considered as a simple free electron wave. This, however, is not sufficient to explain

the experimental observations. A more successful theoretical approach is in many
cases the treatment of the photoemission final state as time reversed LEED state
according to the one-step formalism of photoemission [105, 172]. Calculations of the
band structure of Ag(111) by an approach that considers LEED states reveal for
example a structure, which deviates from a free electron state [173]. Interestingly,
the calculated band structure of Ag(111) from such a LEED approach exhibits a band
gap at energies around $E = 21\,\text{eV}$ [173]. A similar energy gap in the final state band
structure might result in a suppression of the intensity as observed in the presented
data on $BiAg_2/Ag(111)$.

The origin of the photon energy dependence of the photoemission data observed
here is, therefore, very likely due to the final state band structure of $BiAg_2/Ag(111)$.
It is desirable, however, to understand the variations in more detail in order to gain
insight into a possible connection to the photoelectron spin. Such a relation is indicated
by the observed photoelectron spin reversals as well as the exclusive extinction of only
one branch at particular photon energies. A likewise suppression of only one branch
of an intrinsically spin polarized electronic state has for instance been reported for
graphene, where it is known as dark corridor [174]. Similar to our observations, the
disappearance of one branch of the Dirac state in graphene is always observed for
p-polarized light, whereas when s-polarized light is used, it appears only for certain
photon energies [174]. The selective suppression in graphene was explained by an
interference effect between the photoemission from the two atoms in each graphene
unit cell [174, 175].

Interference between different photoemission channels can in general lead to
a strong variation of the photoemission intensity. One example is the interference
between the photoexcitation of a core electron into a state higher in energy and subse-
quent emission of an Auger electron, and the direct photoemission from the valence
band. Such an interference between transitions from the same initial to the same final
state can lead to a strong resonant enhancement of the photoemission intensity at pho-
ton energies close to the binding energies of the involved core levels, often accompanied
by a dip in the intensity at slightly lower photon energies [176–178]. Interestingly, the
observed intensity dips for the spin-up and spin-down branch occur close to the core
level binding energies of Bi $5d_{5/2}$ and Bi $5d_{3/2}$, indicating the possibility of a resonance
effect in the present case. To exclude such a scenario, it is convenient to investigate
structurally similar materials, where no Bi is involved. Therefore, a photon energy
dependent study of the photoemission intensity from the surface electronic structure
of $PbAg_2/Ag(111)$ was performed.

In Fig. 6.13 a comparison of the photon energy dependent photoemission intensity
from the surface states of $PbAg_2/Ag(111)$ and $BiAg_2/Ag(111)$ is shown. The two sur-
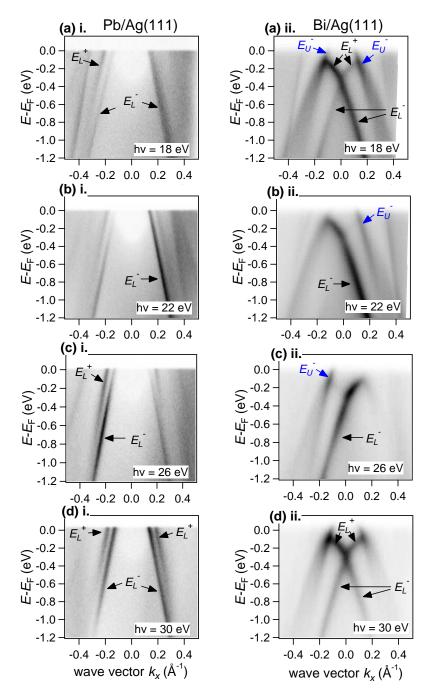
FIGURE 6.13. **Comparison of the band structure of BiAg$_2$/Ag(111) and PbAg$_2$/Ag(111).** (a)-(d) show photon energy dependent ARPES intensity plots of PbAg$_2$/Ag(111) (i.) and BiAg$_2$/Ag(111) (ii.). The photon energies in the measurements shown were $h\nu$ = 18 eV, 22 eV, 26 eV and 30 eV. The data was measured with p-polarized light and light incidence along k_x with the sample aligned with $\bar{\Gamma}\bar{M}$ along k_x. The angle between the incident light and sample surface was $\Theta = 17°$ for BiAg$_2$/Ag(111) and $\Theta = 40°$ for PbAg$_2$/Ag(111). Blue and black arrows mark the upper $E_U^\pm$ and lower $E_L^\pm$ surface states, respectively.

face alloys have a similar crystal structure and develop an equivalent surface band structure, so that a comparison of the surface states is reasonable. On the left part of Fig. 6.13 (i.) ARPES intensity plots measured on PbAg$_2$/Ag(111) are displayed for photon energies of $h\nu = 18$ eV, 22 eV, 26 eV and 30 eV. In order to be able to compare the data to BiAg$_2$, measurements of the surface band structure of BiAg$_2$/Ag(111) are displayed for the same photon energies on the right side (ii.). The ARPES intensity plots were measured with p-polarized light and with the direction of light incidence along k_x. Both samples where aligned with their crystal direction $\bar{\Gamma}\bar{M}$ along k_x. The angle between sample surface and the incoming light was $\Theta = 17°$ for BiAg$_2$ but $\Theta = 40°$ for the measurements on PbAg$_2$ which were performed at beamline BL 9A at HiSOR.

The upper and lower branch of the occupied surface states E_L are marked by arrows and labeled E_L^+ and E_L^-, respectively, for both BiAg$_2$ and PbAg$_2$. Especially for the lower branch E_L^-, the same trends in the photoemission intensity at different photon energies can be observed in the surface states. For a photon energy of $h\nu = 30$ eV (Fig. 6.13 (d)) the photoemission intensity distribution of PbAg$_2$ is quite symmetric, similar to the case of BiAg$_2$. At $h\nu = 26$ eV the left part of the lower branch E_L^- of PbAg$_2$/Ag(111) outweighs the right part. While the photoemission intensity is not completely extinguished, the principle behavior is comparable to the case of BiAg$_2$. The same can be said for a photon energy of $h\nu = 22$ eV, which in both surface alloys shows much higher photoemission intensity for the right part of the branch E_L^- than for the left part. For $h\nu = 18$ eV the intensity asymmetry becomes less pronounced for the surface states of PbAg$_2$ and is negligible in BiAg$_2$.

The observed asymmetries in the photoemission intensity are thus not generic to the surface alloy BiAg$_2$/Ag(111) but occur in a likewise manner in the surface electronic structure of PbAg$_2$/Ag(111). This allows to exclude a resonance effect at the Bi 5d absorption edges. The most likely origin is the shape of the photoemission final state of BiAg$_2$/Ag(111) as well as PbAg$_2$/Ag(111).

The role of the photoemission cross section for the photoelectron spin polarization — a simple model approach

The results presented above reveal that the photoemission intensity from the surface alloys BiAg$_2$/Ag(111) and PbAg$_2$/Ag(111) strongly depends on the wave vector $\boldsymbol{k}_\parallel$ and changes rapidly when the photon energy is varied by only few eV. These dependencies manifest themselves as asymmetries in the spin-integrated angle-resolved photoemission intensity distribution. While such a photon energy and wave vector dependence is most prominent in case of the surface alloys, asymmetric distributions of the angle-resolved photocurrent appear also in Bi$_2$Te$_2$Se and BiTeI. Here, asymme-

tries in the spin-integrated as well as the spin-resolved photoemission signals from the surface electronic structure were shortly discussed in chapter 5. In addition, in the topological surface state of Bi$_2$Te$_3$(0001) as well as in the surface electronic structure of BiAg$_2$/Ag(111) a photon energy dependence of the photoelectron spin polarization was observed. The qualitative discussion given in the following, is aimed at explaining the appearance of asymmetries and photon energy dependencies in a simple model by taking a closer look at the photoemission cross section. In particular, the role of the initial state and final state as well as the interplay between different photoemission transitions will be discussed.

Asymmetries in the angle-resolved photocurrent from the BiAg$_2$/Ag(111) surface alloy clearly depend on the experimental geometry, since they occur along the detection plane $x-z$, given by the incoming light and the analyzer slit, whereas along the direction perpendicular to the detection plane the photoemission intensity distribution is always symmetric as discussed in chapter 5. Symmetries, which are present in the experiment, thus appear to be of some relevance for the appearance of asymmetric intensity distributions and should be considered carefully. The BiAg$_2$ surface alloy exhibits a mirror plane parallel to the $\bar{\Gamma}\bar{K}$ crystal direction, which was in the presented experiments aligned along k_y and, therefore, perpendicular to the detection plane. In case of the surface alloys, only small anisotropies are present in the electronic structure and for the following discussion the crystals will be considered to be approximately isotropic. Therefore, as long as the photon beam is not taken into account, the experiment is mirror symmetric with regard to k_x as well as k_y.

The asymmetry is introduced by the vector field $\boldsymbol{A}$ of the incoming radiation. For s-polarized light the polarization direction $\hat{\boldsymbol{\epsilon}}_s$ of the vector potential $\boldsymbol{A}$ is parallel to the k_y-axis, whereas for p-polarized light the polarization $\hat{\boldsymbol{\epsilon}}_p$ of the vector potential $\boldsymbol{A}$ has a component along the x- as well as along the z-direction with $\hat{\boldsymbol{\epsilon}}_p \cdot \boldsymbol{r} = x + z$. The symmetry of the experiment remains unbroken for s-polarization, since $\hat{\boldsymbol{\epsilon}}_s$ is symmetric with respect to the two in-plane axis. It is, however, broken for p-polarized light. This is easily understood, when imagining the same experiment in a mirror symmetric alignment, where the photon beam is incident from the opposite side along k_x. In such a scenario, the polarization $\hat{\boldsymbol{\epsilon}}_s$ remains the same with regard to the sample surface, whereas for p-polarization the alignment of the polarization $\hat{\boldsymbol{\epsilon}}_p$ of the vector field is changed with respect to the k_x-axis. If the experimental alignment is mirrored with respect to the $x-z$-plane, however, no change of the light electric field occurs for either polarization. Therefore, the symmetry is only broken by p-polarized light along the x-axis allowing the appearance of asymmetric photoemission intensity distributions. For s-polarized light, however, mirror symmetry is always valid.

97

That asymmetric photoemission intensity distributions along certain directions can in principle appear can be understood solely by considering symmetries in the experiment. To gain a detailed understanding of their origin, a closer look at the photoemission current I can yield further insight. It is closely related to the photoemission cross section, which describes the probability that a transition from an initial state Ψ_i to a final state Ψ_f takes place. The cross section can be expressed in terms of photoemission matrix elements $M_{f,i} \propto D = \langle \Psi_f | \hat{\boldsymbol{\epsilon}} \cdot \boldsymbol{r} | \Psi_i \rangle$, where the polarization $\hat{\boldsymbol{\epsilon}}$ of the vector field can generally be written as $\hat{\boldsymbol{\epsilon}} = (\epsilon_x, \epsilon_y, \epsilon_z)$ and $\boldsymbol{r} = (x, y, z)$. The photocurrent I is given by the relation $I \propto |D|^2 \cdot \delta(E_f - E_i - h\nu)$. The delta function $\delta(E_f - E_i - h\nu)$ insures energy conservation and E_f and E_i are the final state and initial state energies, respectively.

Asymmetries in the photoemission current only occur for p-polarized light, therefore, the discussion will primarily cover the case where $\hat{\boldsymbol{\epsilon}} \cdot \boldsymbol{r} = \hat{\boldsymbol{\epsilon}}_p \boldsymbol{r} = \epsilon_x x + \epsilon_z z$ and the photocurrent I_p is:

$$(6.3) \qquad I_p \propto |\langle \Psi_f | \epsilon_x \cdot x | \Psi_i \rangle + \langle \Psi_f | \epsilon_z \cdot z | \Psi_i \rangle|^2 \cdot \delta(E_f - E_i - h\nu).$$

The initial state wave function can, for all surface states which were investigated here, be constructed from p_z-orbitals as well as radially and tangentially aligned p-orbitals. While this constitutes a simplified picture, it is sufficient for a qualitative discussion. The initial state wave function can then be written in a form, already presented in equation 5.1, as:

$$(6.4) \qquad |\Psi\rangle = c_1 |p_z\rangle |\chi_1\rangle + c_2 |p_r\rangle |\chi_2\rangle + c_3 |p_t\rangle |\chi_3\rangle,$$

where $|p_t\rangle = -sin(\alpha) |p_x\rangle + cos(\alpha) |p_y\rangle$ and $|p_r\rangle = cos(\alpha) |p_x\rangle + sin(\alpha) |p_y\rangle$ are the tangentially and radially aligned p-orbitals, respectively, and α is the azimuthal angle ($\alpha = 0$ at $k_x > 0$ and $k_y = 0$, and $\alpha = \pi/2$ at $k_x = 0$ and $k_y > 0$) [159]. The different spatial parts of the wave function are coupled to different spin parts $|\chi_{1-3}\rangle$. To further simplify the discussion, the wave function can be rewritten in terms of p_x- and p_y-orbitals, and the spin part χ will for now be neglected and reconsidered at a later point in the discussion. The initial state wave function becomes:

$$(6.5) \qquad |\Psi_i\rangle = c_1 |p_z\rangle + c_2' e^{-i\alpha} |p_x\rangle + c_3' e^{-i\alpha} |p_y\rangle.$$

If we only consider the photoemission intensity along k_x, along which mirror symmetry is broken by the direction of the vector field of the incident radiation, and using the wave function above, the photocurrent $I_p(\pm k_x)$ can be expressed as:

$$(6.6) \qquad I_p(\pm k_x) \propto \left(|D_x|^2 + |D_z|^2 \pm 2Re D_x^* \cdot D_z \right) \cdot \delta(E_f - E_i - h\nu),$$

with $D_x = \langle \Psi_f | \epsilon_x \cdot x | c_2' p_x \rangle$ and $D_z = \langle \Psi_f | \epsilon_z \cdot z | c_1 p_z \rangle$. The photoemission intensity at positive and negative k_x can differ due to the term $\pm 2 Re D_x^* \cdot D_z$, which has opposite sign for opposite wave vectors k_x. As a result, in the simple approach here, the photocurrent will be at a maximum at positive k_x, when it is at a minimum at negative k_x and vice versa, explaining the asymmetric intensity distributions. Furthermore, asymmetries in the angular distribution of the photoemission intensity only appear, when at least two different transitions take place in the photoemission process — in the present case transitions from the p_x- as well as the p_z-part of the initial state wave function — resulting in a mixed term $Re D_x^* \cdot D_z$ in the photocurrent. For s-polarized light, however, only p_y-orbitals are addressed and no such mixed term appears. The observed photoemission intensity distributions can, therefore, be explained by the simple model introduced here.

Similar investigations of the photoemission intensity can be found in the literature, for instance in reference [179]. Here, the expression $2 Re D_x^* \cdot D_z$ is termed interference term, indicating, that the interplay between the photoemission from different parts of the initial state is responsible for the occurrence of asymmetries in the intensity distribution. Interference between different photoemission channels is also the underlying principle of resonant photoemission, where transitions from the initial state to the same final state occur via an Auger process or via direct photoemission [176–178].

The model wave function that is assumed in the present discussion has a very general and simple form. While it does reflect the observations along k_x, it also results in a similar picture for the situation along k_y, where the symmetry of the experiment as well as the actual observation contradict the emergence of asymmetric photoemission intensity distributions.

In order to understand the dependence of the photocurrent on photon energy, it is not sufficient to consider the operator and initial state alone. Here, the structure of the final state $|\Psi_f\rangle$ must be taken into account as well. The final state $|\Psi_f\rangle$ introduces a photon energy dependence, since it differs depending on photon energy. As a result, also the photoemission cross section depends on photon energy.

The photoemission matrix element $D_{x,y,z}$, which is an imaginary number, can be written as $D_{x,y,z} = |D_{x,y,z}| \cdot e^{i\phi_{x,y,z}}$ with the phase $\phi_{x,y,z}$ of the overlap integral. In this expression the phase $\phi_{x,y,z}$ as well as the absolute value of the matrix element $|D_{x,y,z}|$ are in general photon energy dependent quantities. The photocurrent I_p as measured with p-polarized light becomes:

$$(6.7) \qquad I_p(\pm k_x) \propto |D_x|^2 + |D_z|^2 \pm 2 \cdot |D_x^*| \cdot |D_z| \cdot cos(\phi_x - \phi_z)),$$

where the terms $|D_x|$, $|D_z|$ and the relative phase $\Delta\phi = \phi_x - \phi_z$ depend on photon energy.

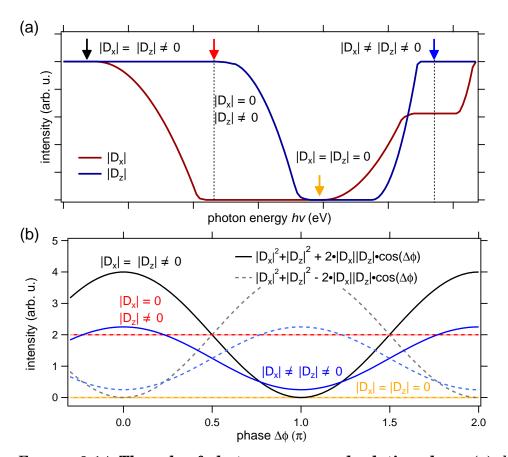FIGURE 6.14. **The role of photon energy and relative phase.** (a) shows
a schematic of a possible photon energy dependence of the absolute val-
ues of the matrix elements $|D_x|$ and $|D_z|$. The intensity distribution is
arbitrary and only serves as a model case scenario. Four different cases
are highlighted by colored arrows: 1. $|D_x| = |D_z| > 0$ (black) 2. $|D_x| = 0$ and
$|D_z| > 0$ (red), 3. $|D_x| = |D_z| = 0$ (yellow) and $|D_x| \neq D_z \neq 0$. (b) shows the
dependence on the relative phase $\Delta\phi$ of the matrix elements for cases 1.
to 4. and for I^+ as well as I^- as solid and dashed lines.

In Fig. 6.14 a schematic illustration of the interplay between D_x and D_z is shown,
which summarizes the influence of the photon energy dependence of the separate
terms in the expression 6.7. In (a) a possible photon energy dependence of the absolute
values of the cross sections $|D_x|$ and $|D_z|$ is displayed. The actual values as well as
the distribution with photon energy are completely arbitrary and only serve as an
illustration. In general, D_x and D_z can behave differently with varying photon energy
and can, therefore, have different values. In the graphic in (a), four cases are especially
highlighted by colored arrows. For all four cases the dependence of the photocurrent
on the relative phase $\Delta\phi$ is shown in (b).

The easiest scenario occurs, when both cross sections become zero at the same

photon energy (yellow). In that case, independent of the relative phase $\Delta\phi$ between D_x and D_z, the overall photoemission intensity is zero. In the simple picture illustrated here this should be valid for the photocurrent I^+ at positive wave vectors as well as for the photocurrent I^- at negative wave vectors. The second possibility is that only one of the two cross sections is zero (red). Again the relative phase plays no role, but the photocurrent is non-zero and yields a constant value of $|D_{x,z}|^2$.

The relative phase becomes relevant when both $|D_x|$ and $|D_z|$ are non-zero. If they are approximately equal $|D_x| \approx |D_z|$ (black), the photocurrent is zero, if the relative phase is an integer multiple of π ($\Delta\phi = n \cdot \pi$ with $n = 0, 1, 2, ...$), even though the separate matrix elements have finite values. The photocurrent I^+ at positive wave vectors and the one at negative wave vectors I^- are never suppressed for the same relative phase but alternate between maximal values and zero. Therefore, this scenario immediately leads to an asymmetric intensity distribution, as observed experimentally for BiAg$_2$/Ag(111). If $|D_x|$ and $|D_z|$ are unequal to zero but have different values (blue), the situation is similar to the case where $|D_x|$ and $|D_z|$ are equal. Once more, minima and maxima occur alternately for I^+ and I^- at the same relative phase values as for $|D_x| \approx |D_z|$. The maxima are, however, much less pronounced, whereas at the minima the intensity is still above zero.

Clearly, there are two scenarios which yield zero photoemission intensity. On the one hand, no photocurrent will be measured if $|D_x| = |D_z| \approx 0$. On the other hand the interference term $ReD_x \cdot D_z$ can induce zero intensity for the case when $|D_x| \approx |D_z|$ and $\Delta\phi = \phi_x - \phi_z = n \cdot \pi$, but only at either positive or negative wave vectors k_x. Since in the presented data zero photoemission intensity does not appear at positive and negative wave vectors k_x at the same photon energies, the second scenario appears to be the case in the photoemission from BiAg$_2$.

The simple model approach introduced above provides an explanation for the strong photon energy dependent variations of the photoemission signal from the surface states of BiAg$_2$/Ag(111). The explanation is based on a photon energy dependence of the cross sections, which results from the structure of the final state wave function, in combination with an interference between the matrix elements D_x and D_z. An elaborate *ab initio* calculation within the one-step photoemission theory was performed by Prof. Eugene Krasovskii to investigate the dependence on photon energy as well as on the wave vector. In the calculation the photoemission current is determined from the transition probability between the initial state and the photoemission final state, likewise to the simple approach employed here. In the theoretical treatment the final state Ψ_f is the time-reversed LEED state, as described by one-step photoemission theory, with the real eigenvalue $E_F = E_i + h\nu$ [180]. The resulting momentum and photon energy dependent photoemission intensities are shown in Fig. 6.15 together
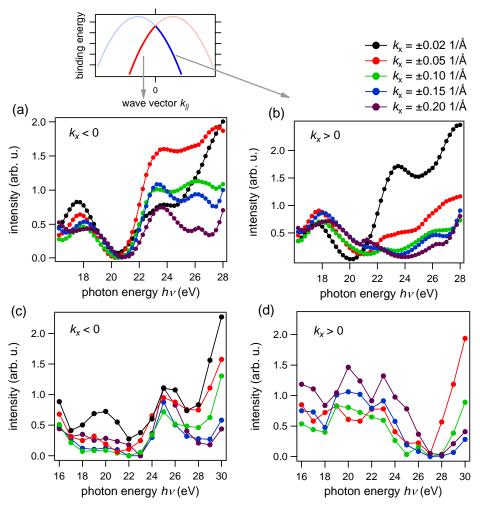
FIGURE 6.15. **Calculated photon energy and wave vector dependent intensities.** The calculated photoemission intensity from the lower branch E_L^- of BiAg$_2$ as indicated in the inset above the graphs is shown in dependence of the photon energy for negative wave vectors between $k_x = -0.20\,\text{Å}^{-1}$ and $k_x = -0.02\,\text{Å}^{-1}$ in (a) and for positive wave vectors with $k_x = 0.02\,\text{Å}^{-1}$ to $k_x = 0.20\,\text{Å}^{-1}$ in (b). The different wave vectors are encoded by colors. (c) and (d) show corresponding experimental data for negative and positive wave vectors, respectively.

with photoemission data to allow a qualitative comparison.

In Fig. 6.15 (a) and (b) the calculated intensities for the lower branch E_L^- in dependence of photon energy are displayed for different wave vectors $k_x = \pm 0.20\,\text{Å}^{-1}$ to $\pm 0.02\,\text{Å}^{-1}$. The left panel (a) shows negative wave vectors, while the intensity distribution at positive wave vectors is displayed in (b). For better comparison with the experimental data, the experimental values are displayed in (c) for negative and in (d) for positive wave vectors. The experimental data was shown and described before in

connection with Fig. 6.11.

The similarities are striking. For negative wave vectors the calculation yields zero intensity at approximately $h\nu = 21$ eV independent of the exact wave vector. A second minimum occurs around approximately $h\nu = 26$ eV. The second minimum, however, strongly depends on the wave vector k_x, as it becomes less pronounced with decreasing value of $|k_x|$. This closely reflects the measured intensities displayed in (c), which also have a zero intensity minimum at approximately $h\nu = 22$ eV and a second local minimum at approximately $h\nu = 29$ eV. The second minimum in the measured photocurrent similarly becomes less pronounced with decreasing $|k_x|$, corresponding to the calculated values. In the experimental data also the minimum at $h\nu \approx 22$ eV becomes less pronounced at small $|k_x|$, at the same time, the exact values of the photon energy are slightly different to the positions of the minima in (a), indicating small deviations between experiment and calculation.

For positive wave vectors, at each wave vector k_x, the calculated intensity shows one distinct minimum. The photon energy at which the minimum occurs varies with the wave vector k_x. For increasing k_x the minimum lies at smaller photon energies $h\nu$, for example at $k_x = 0.20\,\text{Å}^{-1}$ the intensity is minimal at $h\nu = 24$ eV, whereas at $k_x = 0.02\,\text{Å}^{-1}$ the minimum intensity is at $h\nu = 20$ eV. The measured photoemission intensity indeed shows only one distinct minimum at positive wave vectors, which is positioned at approximately $h\nu = 27$ eV. A likewise strong dependence of the position of the minimum regarding photon energy on the wave vector k_x as observed in the theoretical data, does not appear.

Therefore, the calculation nicely reproduces the observed momentum dependent intensity modulations, albeit small deviations between experiment and theoretical calculation occur.

The similarities between calculation and measurement show that the model approach introduced here, which relies on the photon energy dependence of the final state as well as the appearance of an interference term in the photocurrent I_p, is a plausible explanation for the observed asymmetries in the angle resolved photocurrent. The original question, however, deals with the occurrence of photoelectron spin reversals, which were observed in the Rashba spin component S_x of the lower surface state E_L of BiAg$_2$/Ag(111). The above model in the simple framework employed here will, therefore, in the following be extended in order to explain possible origins of a photon energy dependence of the photoelectron spin.

In principal, the strong modulations and sign change in the photoelectron spin polarization of the BiAg$_2$/Ag(111) surface states can be understood as a direct result of the strong photon energy dependence of the photoemission cross section. To understand this in detail, it is helpful to revise the exact experimental geometry, as well as the

results previously discussed in this work. The sample geometry is depicted once more in Fig. 6.16 (a). Light incidence is along the k_x-axis at $\Phi = 0$ and at an angle of $\Theta = 17°$ between sample surface and light beam. The spin polarization in BiAg$_2$ is measured at points along the k_y axis which corresponds to the mirror plane $\bar{\Gamma}\bar{K}$. The measurement is, therefore, performed at wave vectors k_y along the crystal direction perpendicular to the detection plane and in the mirror plane. Strong modulations of the spin polarization occur, when p-polarized light is used and photoelectrons from the p_x- as well as p_z-orbitals are emitted from the sample. For a measurement in the mirror plane and along the k_y-axis, however, the p_x-orbital is odd, whereas the p_z-orbital remains even. In chapter 5 of this work the coupling of different spin structures to the even and odd part of the wave function was discussed in detail. It is, therefore, reasonable to assume that in the present case and sample alignment opposite spin is coupled to the p_x and p_z-orbital, respectively, where the spin quantization axis is parallel to x. The strong modulations of the spin-integrated photoemission intensity in the surface electronic structure of BiAg$_2$, which are a result of the interplay between photoemission from the p_x and p_z-orbital, can, therefore, induce a strong variation of the photoelectron spin at similar photon energies.

A verification of such a scenario is possible in terms of a simple approach, which makes use of the definition of the spin polarization $\boldsymbol{S}$ as the expectation value of the spin matrices $\boldsymbol{\sigma}$:

$$(6.8) \qquad \boldsymbol{S} = \langle f|\boldsymbol{\sigma}|f\rangle,$$

with the final state $|f\rangle$ of the measured photoelectron at the detector. The state $|f\rangle$ can be expressed by the photoemission final state weighted with the respective transition probabilities into final states $\Psi_{f,\chi}$ with a spin $\chi_{\uparrow,\downarrow}$ [181, 182]:

$$(6.9) \qquad |f\rangle = |\Psi_{f,\chi}\rangle\langle\Psi_{f,\chi}|\hat{\boldsymbol{\epsilon}}\cdot\mathbf{r}|\Psi_i\rangle.$$

To simplify this expression, only photoemission from the p_x and p_z part of the initial state wave function will be discussed in the following and the final state $|f_p\rangle$ of an photoelectron emitted by p-polarized light can be written as:

$$(6.10) \qquad |f_p\rangle = |\Psi_{f,\chi_\downarrow}\rangle\langle\Psi_{f,\chi_\downarrow}|\epsilon_x\cdot x|c_2\cdot p_x\cdot\chi_\downarrow\rangle + |\Psi_{f,\chi_\uparrow}\rangle\langle\Psi_{f,\chi_\uparrow}|\epsilon_z\cdot z|c_1\cdot p_z\cdot\chi_\uparrow\rangle.$$

Here, the assumption was made, that the spin part $\chi_{\uparrow,\downarrow}$ of the initial state wave function, which is coupled to the even (p_z) and odd (p_x) part of the spatial wave function, remains unaltered after the photoemission process in the respective final states $|f_{\chi_\uparrow}\rangle$ and $|f_{\chi_\downarrow}\rangle$. This assumption is valid, when spin-flip transitions can be neglected. They are in fact much less likely than spin-conserving transitions in the

photon energy range of the experiment [113, 183]. As a result the state $|f_p\rangle$ can be expressed as combination of final states with either $\chi_\uparrow$ or $\chi_\downarrow$:

(6.11)
$$|f_p\rangle = |f_{z,\chi_\uparrow}\rangle + |f_{x,\chi_\downarrow}\rangle.$$

The initial state spin $\chi_{\uparrow/\downarrow}$, pointing into an arbitrary direction $\hat{\boldsymbol{e}}$ defined by the angles ϑ and φ as illustrated in Fig. 6.16 (a), can, by solving the eigenvalue problem $(\boldsymbol{\sigma}\hat{\boldsymbol{e}})\cdot\chi = \lambda\cdot\chi$, be expressed as $\chi_\uparrow = (\cos(\frac{\vartheta_s}{2}); \sin(\frac{\vartheta_s}{2})\cdot e^{i\varphi_s})$ and $\chi_\downarrow = (\sin(\frac{\vartheta_s}{2}); -\cos(\frac{\vartheta_s}{2})\cdot e^{i\varphi_s})$. The determination of χ is for instance shown in reference [111]. For an initial state spin S_x pointing along x, the spin eigenvalues become $\chi_\uparrow = (\frac{1}{2}\sqrt{2}; \frac{1}{2}\sqrt{2})$ and $\chi_\downarrow = (\frac{1}{2}\sqrt{2}; -\frac{1}{2}\sqrt{2})$.

In the presented spin-resolved experiments on BiAg$_2$/Ag(111) the initial state spin can be assumed to be oriented along x from the Rashba-Bychkov model and the expectation value $\boldsymbol{S} = \langle f|\boldsymbol{\sigma}|f\rangle \propto (\langle f_{z,\uparrow}| + \langle f_{x,\downarrow}|)\boldsymbol{\sigma}(|f_{z,\uparrow}\rangle + |f_{x,\downarrow}\rangle)$ yields the expected spin polarization of the photoelectron in the final state. The calculation of $\boldsymbol{S}$ results in:

(6.12)
$$\boldsymbol{S} \propto \begin{pmatrix} |D_z|^2 - |D_x|^2 \\ 2\cdot|D_z|\cdot|D_x|\cdot\sin(\Delta\phi) \\ 2\cdot|D_z|\cdot|D_x|\cdot\cos(\Delta\phi) \end{pmatrix}$$

As before, the absolute values $|D_{x,z}|$ as well as the relative phase $\Delta\phi$ of the matrix elements D_x and D_z are photon energy dependent values. The spin polarization $\boldsymbol{S}$ is, therefore, closely connected to the spin-integrated photoemission cross section. In case of the spin polarization S_x measured in the photoemission experiment on BiAg$_2$, the expected polarization depends on the relative values of the matrix elements $|D_x|$ and $|D_z|$. If $|D_x|$ is smaller than $|D_z|$, the spin polarization S_x is positive, it is negative, on the other hand, when $|D_x|$ is larger than $|D_z|$. In a photon energy range, where $|D_x|$ and $|D_z|$ vary strongly, as is the case for the photoemission from the BiAg$_2$ surface states, also strong variations of the photoelectron spin polarization S_x can be expected. In particular, when the dominating contribution switches between $|D_x|$ and $|D_z|$ the spin polarization of the photoelectrons changes sign.

The simple approach presented here, therefore, already suffices to explain the strong modulations and asymmetries, as well as photon energy dependencies of the spin-integrated and spin-resolved photoemission current from the surface electronic structure of BiAg$_2$. A more detailed examination is again possible with the help of *ab initio* calculations in the framework of one-step photoemission theory. A calculation of the photon energy dependent spin polarization is presented in Fig. 6.16 (b). The calculation is performed for a similar sample alignment as in the experiment. The light is incident along the k_x axis, therefore, $\Phi = 0°$. In the calculation, however, the angle between incoming light and sample surface is $\Theta = 45°$, which is different to
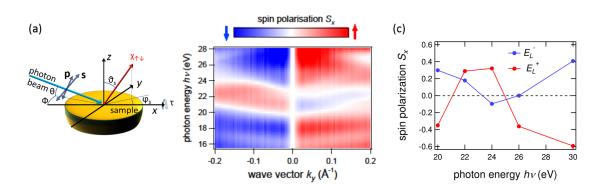
Figure 6.16: **Calculated photon energy dependent spin polarization in
BiAg$_2$/Ag(111).** (a) shows the experimental geometry. The incoming light beam is
depicted as blue arrow. The red arrow illustrates the spin polarization direction χ
along an arbitrary direction defined by the angle ϑ_s and φ_s. For the spin-resolved
photoemission experiment on BiAg$_2$ $\Phi = 0°$, $\Theta = 17°$ and the detection plane is along
k_x. The calculated $h\nu$-dependent photoelectron spin polarization S_x along $\bar{\Gamma}\bar{K}||k_y$ of
the surface state branch E_L^- is depicted in (b), for $\Theta = 45°$. (c) shows the experimental
spin polarization S_x for different photon energies at positive wave vectors k_y.

the experiment, where $\Theta = 17°$. The crystal direction $\bar{\Gamma}\bar{M}$ is assumed to be parallel
to the k_x axis and the spin polarization is calculated along the $\bar{\Gamma}\bar{K}$-direction, which
lies in the mirror plane of the crystal and parallel to k_y, likewise to the experimental
alignment. The sample rotation around the x-axis by a few degrees, which is necessary
in the experiment, is neglected in the calculation, since it can be assumed to have no
significant influence on the outcome.

Clearly, the calculated spin polarization in Fig 6.16 (b) is approximately opposite for
positive and negative wave vectors, as expected for the initial state spin polarization.
If the photon energy is changed, however, reversals of the polarization are predicted
at photon energies of approximately $h\nu \approx 20$ eV and $h\nu \approx 24$ eV. This is quite similar
to the experimental observations, displayed in Fig. 6.16 (c) for comparison, where
spin polarization reversals occur at comparable photon energies. The experimental
data was displayed and discussed before in connection with Fig. 6.8. The theoretical
calculation nicely reproduces the experimental results for BiAg$_2$, where spin reversals
occur between $h\nu = 20$ eV and $h\nu = 22$ eV and between $h\nu = 24$ eV and $h\nu = 26$ eV
for the upper branch E_L^+ and between $h\nu = 22$ eV and $h\nu = 24$ eV as well as between
$h\nu = 24$ eV and $h\nu = 26$ eV for the lower branch E_L^-.

The calculated spin modulations in the surface states of BiAg$_2$ stem from the inter-
play between different parts of the overall photoemission current, which vary strongly
in the photon energy range, where the spin reversal takes place. It, therefore, confirms
the strong connection between the measured spin polarization and the photoemission

cross section as already discussed in the model approach above.

The model description presented above is valid for the case of BiAg$_2$, where the spin polarization S_x was measured at k-points along the mirror plane with p-polarized light. The same approach can be used to explain the photoelectron spin reversal and photon energy dependence observed in the spin component S_z of the topological surface state of Bi$_2$Te$_3$(0001). To interpret the spin-resolved data from Bi$_2$Te$_3$, it is once more beneficial to reconsider the exact alignment of sample and light beam. The sample was aligned with $\bar{\Gamma}\bar{K}$, which is the plane perpendicular to the mirror plane, parallel to the detection plane and the spin-resolved data corresponds to points along $\bar{\Gamma}\bar{K}$. The light polarization was again p-polarized, therefore the p_x- and p_z-like orbitals were probed in the experiment, similar to the situation discussed above. In order to understand the spin polarization reversal observed in the out-of-plane component in the topological surface state of Bi$_2$Te$_3$ in the framework of the model discussed above, one has to take into account, that for a measurement which is not in the mirror plane of the crystal, even and odd as well as the assignment of different spin structures to the even and odd part of the initial state wave function is not well defined [107]. While the anisotropy between the crystal directions can in many cases be neglected, it makes a huge difference, which direction is considered in the surface electronic structure of Bi$_2$Te$_3$, given by the strong warping in the band structure. Therefore, a mixture of $\chi_\uparrow$ and $\chi_\downarrow$ can in principle be coupled to each part p_x and p_z of the initial state wave function in the particular experiment on Bi$_2$Te$_3$. As a result, when the p_x and p_z orbitals are probed, it is indeed possible that initial states coupled to different spin directions appear in the overall matrix elements, leading to the observed modulations of the out-of-plane spin S_z.

The spin polarization modulations observed in the measured band structure of Bi$_2$Te$_3$ in the out-of-plane spin S_z show a sinusoidal variation with photon energy. Indeed, the spin polarization in equation 6.12 calculated in the framework of the simple model implies a similar dependence of the components S_y and S_z on the phase $\Delta\phi$, when the initial state spin is assumed to be along x. While the dependence of the relative phase $\Delta\phi$ on photon energy is not necessarily a linear one, the general behavior of a modulating spin polarization S_z as observed in Bi$_2$Te$_3$ is well described. This shows, that the model approach is able to explain the appearance as well as variations in the out-of-plane spin polarization even without an initial state spin component along z.

In conclusion, a photon energy dependent spin polarization as observed in the surface electronic structure of BiAg$_2$/Ag(111) but also Bi$_2$Te$_3$(0001) can be explained by the interplay between photoemission from different parts of the initial state wave function, which are coupled to different spin structures. The exact coupling of the

spin structures to different parts of the initial state wave function depends a lot on the symmetries which are present in the experiment. In the presented case of BiAg$_2$ transitions from $p_x \cdot \chi_\downarrow$ as well as the $p_z \cdot \chi_\uparrow$ initial state wave function take place. Due to the high anisotropy and different sample alignment in case of Bi$_2$Te$_3$, the coupling of different spin structures to the p_x and p_z is not well defined. Therefore, it can be assumed that different initial state spins take part in the photoemission process, leading to the observed photoelectron spin reversal.

In general, signatures of an interplay between photoemission from different parts of the initial state wave function can already be found in the spin-integrated photoemission data, where strong asymmetries and modulations with photon energy appear at similar photon energies as the photoelectron spin reversal. This indicates a close relation between the spin-integrated photocurrent and the measured photoelectron spin polarization. In fact, the simple model introduced above can be seen as compelling demonstration for the direct connection of the photon energy dependent photoelectron spin polarization and the photoemission cross section.

While the model approach introduced in this chapter is based on simple assumptions for the initial state as well as final state wave function, *ab initio* calculations in the framework of one-step photoemission theory show a high agreement with the experimental results based on a likewise interplay between the matrix elements. The general approach assumed here, therefore, serves as a sufficient model to explain the observed photon energy dependent spin polarization.

CONCLUDING DISCUSSION

Electrons emitted from solids under the influence of spin-orbit coupling are in many cases spin polarized [34]. To what extend the measured spin polarization mirrors the spin properties in the ground state was one of the central questions in this work. In particular, disentangling the role of the experimental geometry and the photoemission process from the spin-orbit coupling in the initial state and the intrinsic spin properties was a goal in the framework of this thesis.

To gain insight into the spin structures inherent to an electronic state, it is first necessary to understand how the spin properties in a bound state can in general be defined. Under the influence of spin-orbit coupling the spin and orbital momentum can not be considered as independent quantum numbers, anymore [184], and the eigenfunctions of the spin S and orbital momentum L separately are no eigenfunctions of the Hamiltonian H that describes the system. As a consequence, the spin in an electronic state in a condensed matter is coupled to the spatial wave function of the state. More precisely, different spin structures $\chi_{1,2}$ are coupled to different parts of the spatial wave function $\Phi_{1,2}$ so that the complete wave function including the spin structure can be expressed as:

$$(7.1) \qquad\qquad \Psi_k = \Phi_1 \cdot \chi_\uparrow + \Phi_2 \cdot \chi_\downarrow.$$

It is, therefore, not possible to sufficiently characterize the spin properties by a single number, as obtained for example in a single measurement of the spin polarization along a particular quantization direction. A more adequate account of the spin structure is given by a vector which depends on the orbital as well as the crystal momentum.

Even though a single measurement of the photoelectron spin polarization can not yield the complete spin structure, the measured spin in a spin-resolved experiment

can be traced back to the spin properties in the initial state. Spin-flip transitions during the photoemission process, which would actively change the spin properties of a photoelectron during the transition, are negligible [112]. To what extend the different parts $\chi_\uparrow$ and $\chi_\downarrow$ contribute to the full measured photoelectron spin polarization is determined by the transition probabilities from the individual initial states Φ_1 and Φ_2 to the final state Ψ_f. The magnitude of the transition probabilities depends on the experimental alignment as well as on the photon energy.

Therefore, if one carefully considers the photoemission cross sections, it is in many cases possible to access the spin properties in the initial state, for example by exclusively probing either Φ_1 or Φ_2. An example for such a scenario is given by the results presented in chapter 5 of this thesis, where it was demonstrated that a switch of the light polarization from linear p-polarized to s-polarized leads to a full reversal of the photoelectron spin polarization in the surface electronic structure of Bi_2Te_2Se as well as BiTeI. Here, the cross section for excitation of electrons from the even or odd orbitals becomes zero when s-polarized light or p-polarized light is used, respectively. In an isotropic crystal or parallel to a mirror plane of a crystal, the even and odd orbitals are coupled to different spin structures and linear polarized light selectively probes either $\Phi_1 \cdot \chi_\uparrow$ or $\Phi_2 \cdot \chi_\downarrow$. The results in chapter 5 thus serve as striking demonstration of the coupling of different spin structures to different parts of the spatial wave function due to spin-orbit coupling. It is also a prime example that a photoemission experiment can yield insight into the spin structure inherent to the initial state wave function, when the experimental geometry is chosen with care. The results in chapter 5 exemplify that the alignment of the electric field of the incoming light and the symmetries of the crystal have to be considered to interpret the measured spin polarization.

Photoemission cross sections determine the spin-integrated photoemission intensities, therefore, they can be probed systematically in dependence of the experimental geometry or the photon energy by photoelectron spectroscopy. The cross section describes the probability of a transition into the final state Ψ_f. It is, therefore, in general a photon energy dependent value, owing to the structure of the photoemission final state. In an experiment, where both spatial parts Φ_1 and Φ_2 of the overall wave function are probed simultaneously given by the experimental alignment, also the relative portion of photoelectrons with $\chi_\uparrow$ and $\chi_\downarrow$ character can vary with photon energy. In such a case, the resulting photoelectron spin polarization depends on photon energy. On one side, this makes a correct deduction of the spin properties of the initial state impossible, when only one photon energy is probed in an experimental alignment that addresses $\Phi_1 \cdot \chi_\uparrow$ and $\Phi_2 \cdot \chi_\downarrow$ at once, if the respective cross sections are unknown. On the other side, systematic photon energy dependent measurements of the spin-integrated as well as spin-resolved photoemission current has the potential to yield

additional information on the intrinsic spin structure. This is for example the case for the surface alloy BiAg$_2$/Ag(111). The results presented in chapter 6.2 of this work demonstrate that a change of the photon energy leads to strong modulations and sign reversals of the photoelectron spin polarization of the surface states of BiAg$_2$. At the same photon energies strong variations and even a complete extinction of the photoemission intensity is observed selectively for different branches of the state at different energies. A thorough analysis allowed to deduce that this extinction occurs when the different parts of the wave function contribute equally to the overall cross section, which leads to a destructive interference. Knowing the contributions of the individual cross sections, it becomes possible to evaluate the initial state spin structure in more detail. The data on the surface electronic structure of BiAg$_2$ reveal that a different spin character is predominant, when either the p_x- or the p_z-orbital part of the initial state wave function dominates the complete photoemission cross section.

In chapter 6.1 similar photon energy dependent modulations of the photoelectron spin polarization were observed for the topological surface state of Bi$_2$Te$_3$(0001). Here, a spin polarization along the direction perpendicular to the surface appears, which changes sign with photon energy. An out-of-plane spin polarization is in fact predicted for the topological surface state of Bi$_2$Te$_3$. However, also a spin polarization oriented in-plane, which can be expected in these kind of states, can yield a nonzero out-of-plane spin polarization as a result of the matrix element effects described above. More precisely, for an initial state spin polarization oriented in plane ($\chi_{\uparrow,\downarrow,\parallel}$), the interference between $\chi_{\uparrow,\parallel}$ and $\chi_{\downarrow,\parallel}$ can generate a spin polarization along the surface normal which depends on the photon energy. Moreover, in the presented experiment on the strongly warped topological surface state of Bi$_2$Te$_3$ it is not possible to selectively probe only one particular spin structure, since the coupling of different spins to the even or odd orbital part is only well defined in the special case of an isotropic environment [107]. The data is, therefore, not sufficient to evaluate, whether the topological surface state does exhibit an intrinsic spin polarization along the surface normal. A thorough investigation over a larger photon energy range might reveal a constant offset in the measured spin polarization, if indeed a significant intrinsic out-of-plane polarization exists. Otherwise, calculations of the photoemission cross sections associated with different orbitals and the related spin polarization could possibly yield additional insight.

Considering the crucial role of the final state for the measured spin polarization, the question arises, whether spin-orbit coupling in the final states has a considerable effect on the measured spin polarization. The strong agreement between the experimental data on BiAg$_2$/Ag(111) presented in this work and the corresponding photoemission calculations, where spin-orbit coupling in the final state was likewise neglected, suggest an only minor role of such effects, at least in the probed surface

alloys. In reference [33], a detailed theoretical study of the role of spin-orbit coupling in the initial and final states for the spin polarization of photoelectrons emitted from Pt(111) similarly yields an only small contribution of spin-orbit coupling in the final state. An influence of such effects might, however, become relevant in other cases, depending on excitation energy and the probed system.

In summary, the measured spin polarization of photoelectrons can be understood as a result of the combination of different initial state spin structures that are probed simultaneously in the experiment. All variations of the photoelectron spin polarization arise due to changes of the cross sections associated with different parts of the spatial wave function that are coupled to opposite spin, owing to spin-orbit coupling. On the one hand, the matrix elements change, when different parts of the initial state wave function are probed for instance as a result of the polarization direction of the incoming radiation. On the other hand, relative values of matrix elements can change with photon energy, owing to the structure of the photoemission final state, and different spin parts can dominate at different photon energies. Therefore, while it is indeed possible to access spin properties in the initial state by spin-resolved photoemission, a careful consideration of the symmetries in the crystal as well as the experimental alignment is required to correctly interpret the results. One can even make use of the photon energy dependence of the cross sections, if it allows to evaluate, which parts of the wave functions are probed at particular photon energies.

The results thus show that despite the challenges in data interpretation, photoelectron spectroscopy is the primary method to address the momentum-resolved spin properties in the electronic bands of a material. The last years much effort was put into the development and implementation of spin detectors of different kinds in various laboratories as well as at synchrotron light sources, not least due to the increasing interest in the spin-texture of novel material classes. Prominent examples are the ESPRESSO setup at the Hiroshima synchrotron radiation center [83], which is based on very low energy electron diffraction on a magnetized target, the Mott-detector based spin-resolving setup at the COPHEE endstation at the Paul Scherrer Institute [185], spin-resolving momentum microscopy setups as well as spin-resolving electron mirrors combined with a time-of-flight detector, which allow multichannel spin detection [124, 127, 186, 187] and the newly proposed i-Mott, which can capture the three-dimensional spin information [188]. The increasing variety of set-ups allows the utilization of different detectors, sample geometries and excitation energies, depending on the particular scientific question.

One can consider a few examples that are in the focus of current research, and discuss concrete possibilities to access the initial state spin polarization based on the findings in this work. Currently much debated are magnetic topological insulators, where magnetic impurities in combination with the large spin-orbit coupling inherent to the materials give rise to a novel topological phase: the quantized anomalous Hall effect [189]. The magnetic moments can induce an overall spin polarization in the electronic structure. To distinguish the spin polarization induced by magnetism from the intrinsic spin structure which can for example in Bi_2Te_3(0001) yield an out-of-plane component of the photoelectron spin, one can change the magnetization direction by an extrinsic magnetic field. In a spin-resolved photoemission experiment the inverted magnetic field leads to a reversal of the magnetism-induced spin polarization and a comparison of the complete out-of-plane spin polarization can yield insight. On the other hand, a systematic photon energy dependent measurement, which was shown here to result in strong modulations of the photoelectron spin polarization, can also give information on the spin polarization of the magnetized ground state, since a significant initial state spin polarization should lead to a constant offset in the measured initial state spin with variable photon energies.

Another material class which attracts much attention are Weyl semimetals, which have only recently been experimentally realized [14, 15]. At particular points, so called Weyl nodes, in their electronic structure quasiparticles reminiscent of Weyl fermions — massless particles with a defined chirality — exist [190]. The bulk band structure of Weyl semimetals has topological properties. Unlike the topological insulators, however, valence and conduction band touch each other at particular energies, forming the Weyl nodes [190]. Weyl nodes of opposite chirality are connected by spin polarized surface states, while in the bulk electronic structure Dirac-cone-like features appear [15]. The spin polarization of the surface states has been experimentally verified [191], studies of the spin character of the bulk Dirac-cones, however, remain scarce. Addressing the spin properties of a bulk state holds some difficulties owing to the k_z dependent band structure. A systematic investigation of the photon energy dependent photoelectron spin polarization can, therefore, be hindered by the varying band dispersion with excitation energy. On the other hand, in photoemission the Weyl nodes can be probed by photon energies in the soft x-ray regime [15], where the final state structure is often much simpler and can be approximated by a free electron state [158]. If the influence of the final states is negligible, a reconstruction of the complete spin-orbital texture by measurements in different experimental alignments for example through a change of light incidence and polarization, becomes easier.

In any case, this thesis demonstrates that the result of a spin-sensitive photo-emission experiment is determined by the interplay between spin-orbit coupling in the initial state and the photoemission process. For a meaningful interpretation of

the photoelectron spin polarization not only the initial state properties but also the experimental geometry and the photoemission final state which leads to a photon energy dependence have to be taken into account.

In Appendix A, photon energy dependent angle-resolved photoelectron spectroscopy (ARPES) data on the surface electronic structure of the surface alloys BiAg$_2$/Ag(111) and PbAg$_2$/Ag(111) over the complete measured photon energy range are presented. The data was shown only partly in the main section of this work.

Fig. A.1 shows the complete measured photoelectron spectroscopy data on the surface electronic structure of BiAg$_2$/Ag(111) starting at $h\nu = 8\,\text{eV}$ until $h\nu = 40\,\text{eV}$. Light incidence was in the detection plane along the k_x-direction, which is parallel to the $\bar{\Gamma}\bar{\text{M}}$ crystal direction and at an angle of $\Theta = 17°$ with respect to the sample surface. The data nicely demonstrates the gradually evolving asymmetric intensity distribution with increasing photon energy. Whereas up to approximately $19\,\text{eV}$ the intensity distribution remains relatively symmetric, at energies between $20\,\text{eV}$ and about $28\,\text{eV}$ strong asymmetries appear. Thereby, at for example $h\nu = 22\,\text{eV}$ the left parabolic band dominates, while at around $h\nu = 26\,\text{eV}$ the right parabolic band has higher intensity. The photoemission intensity is again more evenly distributed at energies above approximately $28\,\text{eV}$. These intensity variations in a rather small photon energy interval can be traced back to a signature of the structure of the photoemission final state of BiAg$_2$/Ag(111).

Fig. A.2 shows photon energy dependent measurements on the surface states of BiAg$_2$/Ag(111), performed with s-polarized light in a photon energy range from $h\nu = 19\,\text{eV}$ to $h\nu = 29\,\text{eV}$. Light incidence was once more along the k_x-axis, with the crystal oriented with the $\bar{\Gamma}\bar{\text{M}}$ crystal direction parallel to k_x and at an angle of $17°$ between sample surface and light beam. The photoemission intensity distribution as
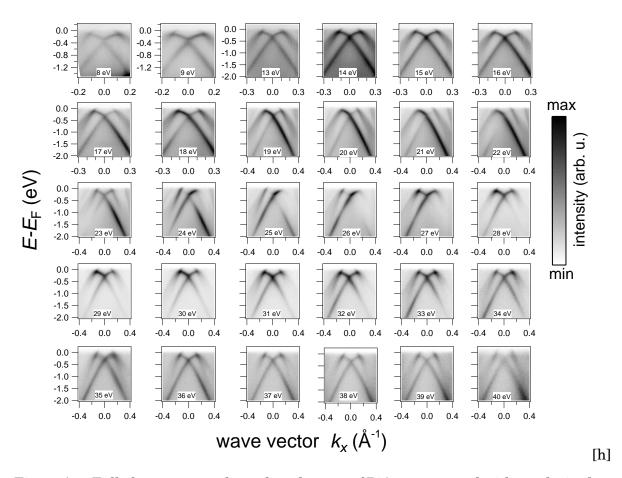
[h]

Figure A.1: Full photon energy dependent data set of BiAg$_2$, measured with p-polarized light along $\bar{\Gamma}\bar{M}$.

measured with s-polarized light is completely symmetric, within experimental accuracy, in all ARPES intensity plots shown.

Fig. A.3 shows ARPES data sets of the surface surface electronic structure of BiAg$_2$/Ag(111), measured with photon energies from $h\nu = 20\,\text{eV}$ to $h\nu = 29\,\text{eV}$ with p-polarized light. The direction of light incidence was in the detection plane along the k_x-axis and at an incidence angle of $\Theta = 17°$ with respect to the sample surface. Compared to the data displayed in Figs. A.1 and A.2, the sample was rotated by 90°, therefore the $\bar{\Gamma}\bar{K}$ crystal direction lies in the detection plane in the data in Fig. A.3. The photoemission intensity distribution shows a highly asymmetric intensity distribution throughout the photon energy range displayed. In particular at around $h\nu = 22\,\text{eV}$ the left parabolic band dominates the photoemission intensity, whereas at around $h\nu = 26\,\text{eV}$ it completely vanishes.
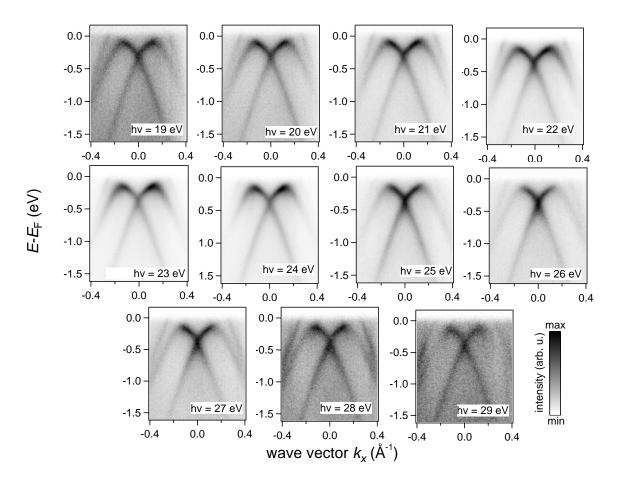
Figure A.2: Full photon energy dependent data set of BiAg$_2$/Ag(111), measured with s-polarized light along $\bar{\Gamma}\bar{M}$.

Fig. A.4 illustrates the photon energy dependence of the photoemission intensity as measured on the surface electronic structure of the surface alloy PbAg$_2$/Ag(111). The data displayed was measured with photon energies between $h\nu = 16$ eV and $h\nu = 30$ eV. Light incidence was parallel to the detection plane and k_x, and at an angle of $\Theta = 40°$ between sample surface and light beam. The sample was oriented with its $\bar{\Gamma}\bar{M}$ crystal direction parallel to k_x. Over the complete energy range strong variations of the photoemission intensities are present, in particular, a likewise high asymmetry as observed for the case of the BiAg$_2$/Ag(111) surface alloy is visible.
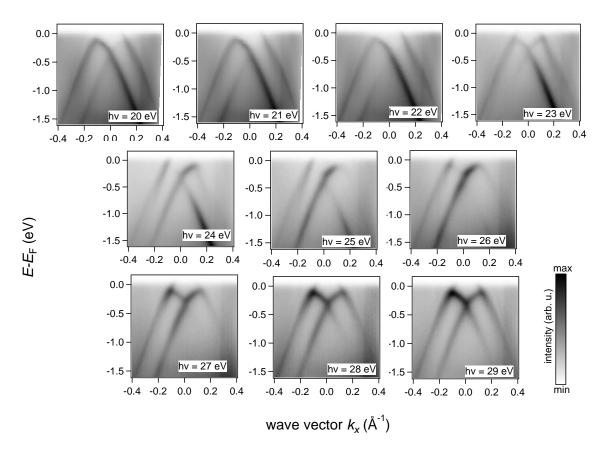
Figure A.3: Full photon energy dependent data set of BiAg$_2$/Ag(111), measured with p-polarized light along $\bar{\Gamma}\bar{K}$.
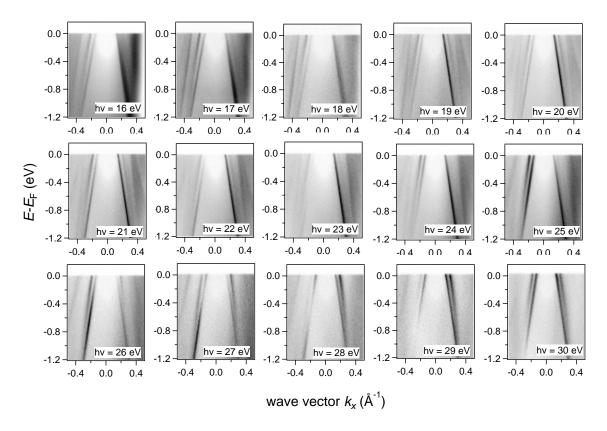
Figure A.4: Full photon energy dependent data set of PbAg₂/Ag(111), measured with p-polarized light along $\bar{\Gamma}\bar{M}$.

[1]   S. Datta and B. Das. "Electronic analog of the electro-optic modulator". *Appl. Phys. Lett.* **56** (1990), pp. 665–667.

[2]   T. Koga, J. Nitta, H. Takayanagi, and S. Datta. "Spin-Filter Device Based on the Rashba Effect Using a Nonmagnetic Resonant Tunneling Diode". *Phys. Rev. Lett.* **88** (2002), p. 126601.

[3]   D. D. Awschalom, M. E. Flatté, and N. Samarth. "Spintronics". *Sci. Am.* **286** (2002), pp. 66–73.

[4]   D. Pesin and A. H. MacDonald. "Spintronics and pseudospintronics in graphene and topological insulators". *Nat. Mater.* **11** (2012), pp. 409–416.

[5]   I. Žutić, J. Fabian, and S. D. Sarma. "Spintronics: Fundamentals and applications". *Rev. Mod. Phys.* **76** (2004), p. 323.

[6]   C. Felser, G. Fecher, and B. Balke. "Spintronics: A Challenge for Materials Science and Solid-State Chemistry". *Angew. Chem. Int. Ed.* **46** (2007), pp. 668–699.

[7]   L. Fu and C. Kane. "Topological insulators with inversion symmetry". *Phys. Rev. B* **76** (2007), p. 045302.

[8]   H. Zhang, C.-X. Liu, X.-L. Qi, X. Dai, Z. Fang, and S.-C. Zhang. "Topological insulators in Bi_2Se_3, Bi_2Te_3 and Sb_2Te_3 with a single Dirac cone on the surface". *Nat. Phys.* **5** (2009), pp. 438–442.

[9]   M. Z. Hasan and C. L. Kane. "Colloquium: Topological insulators". *Rev. Mod. Phys.* **82** (2010), pp. 3045–3067.

[10]   X.-L. Qi and S.-C. Zhang. "Topological insulators and superconductors". *Rev. Mod. Phys.* **83** (2011), pp. 1057–1110.

[11]   I. Zeljkovic, Y. Okada, C.-Y. Huang, R. Sankar, D. Walkup, W. Zhou, M. Serbyn, F. Chou, W.-F. Tsai, H. Lin, A. Bansil, L. Fu, M. Hasan, and V. Madhavan. "Map-

ping the unconventional orbital texture in topological crystalline insulators". *Nat. Phys.* **10** (2014), pp. 572–577.

[12] L. Fu. "Topological Crystalline Insulators". *Phys. Rev. Lett.* **106** (2011), p. 106802.

[13] Y. J. Wang, W.-F. Tsai, H. Lin, S.-Y. Xu, M. Neupane, M. Z. Hasan, and A. Bansil. "Nontrivial spin texture of the coaxial Dirac cones on the surface of topological crystalline insulator SnTe". *Phys. Rev. B* **87** (2013), p. 235317.

[14] B. Lv, H. Weng, B. Fu, X. Wang, H. Miao, J. Ma, P. Richard, X. Huang, L. Zhao, G. Chen, Z. Fang, X. Dai, T. Qian, and H. Ding. "Experimental Discovery of Weyl Semimetal TaAs". *Phys. Rev. X* **5** (2015), p. 031013.

[15] S.-Y. Xu, I. Belopolski, N. Alidoust, M. Neupane, G. Bian, C. Zhang, R. Sankar, G. Chang, Z. Yuan, C.-C. Lee, S.-M. Huang, H. Zheng, J. Ma, D. S. Sanchez, B. Wang, A. Bansil, F. Chou, P. P. Shibayev, H. Lin, S. Jia, and M. Hasan. "Discovery of a Weyl fermion semimetal and topological Fermi arcs". *Science* **349** (2015), pp. 613–617.

[16] M. Dzero, K. Sun, V. Galitski, and P. Coleman. "Topological Kondo Insulators". *Phys. Rev. Lett.* **104** (2010), p. 106408.

[17] H. Weng, J. Zhao, Z. Wang, Z. Fang, and X. Dai. "Topological Crystalline Kondo Insulator in Mixed Valence Ytterbium Borides". *Phys. Rev. Lett.* **112** (2014), p. 016403.

[18] M. Kim, J. Im, A. J. Freeman, J. Ihm, and H. Jin. "Switchable S= 1/2 and J= 1/2 Rashba bands in ferroelectric halide perovskites". *Proc. Natl. Acad. Sci.* **111** (2014), pp. 6900–6904.

[19] D. Di Sante, P. Barone, R. Bertacco, and S. Picozzi. "Electric Control of the Giant Rashba Effect in Bulk GeTe". *Adv. Mater.* **25** (2013), pp. 509–513.

[20] T. Ritschel, J. Trinckauf, K. Koepernik, B. Büchner, M. v. Zimmermann, H. Berger, Y. I. Joe, P. Abbamonte, and J. Geck. "Orbital textures and charge density waves in transition metal dichalcogenides". *Nat. Phys.* **11** (2015), pp. 328–331.

[21] X. Xu, W. Yao, D. Xiao, and T. F. Heinz. "Spin and pseudospins in layered transition metal dichalcogenides". *Nat. Phys.* **10** (2014), pp. 343–350.

[22] J. M. Riley, W. Meevasana, L. Bawden, M. Asakawa, T. Takayama, T. Eknapakul, T. K. Kim, M. Hoesch, S.-K. Mo, H. Takagi, T. Sasagawa, M. S. Bahramy,

and P. D. C. King. "Negative electronic compressibility and tunable spin splitting in WSe$_2$". *Nat. Nanotechnol.* **10** (2015), pp. 1043–1047.

[23] P. D. C. King, S. McKeown Walker, A. Tamai, A. de la Torre, T. Eknapakul, P. Buaphet, S.-K. Mo, W. Meevasana, M. S. Bahramy, and F. Baumberger. "Quasiparticle dynamics and spin-orbital texture of the SrTiO$_3$ two-dimensional electron gas". *Nat. Commun.* **5** (2014), p. 3414.

[24] A. F. Santander-Syro, F. Fortuna, C. Bareille, T. C. Rödel, G. Landolt, N. C. Plumb, J. H. Dil, and M. Radović. "Giant spin splitting of the two-dimensional electron gas at the surface of SrTiO$_3$". *Nat. Mater.* **13** (2014), pp. 1085–1090.

[25] C. M. Schneider, P. Schuster, M. Hammond, H. Ebert, J. Noffke, and J. Kirschner. "Spin-resolved electronic bands of FCT cobalt". *J. Phys.: Condens. Matter* **3** (1991), pp. 4349–4355.

[26] M. Getzlaff, J. Bansmann, J. Braun, and G. Schönhense. "Spin resolved photoemission study of Co(0001) films". *J. Magn. Magn. Mater.* **161** (1996), pp. 70–88.

[27] J. Kirschner. "Spin-polarized electron emission from magnetic and non-magnetic solids". *Appl. Phys. A* **44** (1987), pp. 3–11.

[28] M. Hoesch, M. Muntwiler, V. N. Petrov, M. Hengsberger, L. Patthey, M. Shi, M. Falub, T. Greber, and J. Osterwalder. "Spin structure of the Shockley surface state on Au (111)". *Phys. Rev. B* **69** (2004), 241401(R).

[29] J. Henk, A. Ernst, and P. Bruno. "Spin polarization of the L-gap surface states on Au(111)". *Phys. Rev. B* **68** (2003), p. 165416.

[30] D. Hsieh, Y. Xia, D. Qian, L. Wray, F. Meier, J. H. Dil, J. Osterwalder, L. Patthey, A. V. Fedorov, H. Lin, A. Bansil, D. Grauer, Y. S. Hor, R. J. Cava, and M. Z. Hasan. "Observation of Time-Reversal-Protected Single-Dirac-Cone Topological-Insulator States in Bi$_2$Te$_3$ and Sb$_2$Te$_3$". *Phys. Rev. Lett.* **103** (2009), p. 146401.

[31] C. Jozwiak, C.-H. Park, K. Gotlieb, C. Hwang, D.-H. Lee, S. G. Louie, J. D. Denlinger, C. R. Rotundu, R. J. Birgeneau, Z. Hussain, and A. Lanzara. "Photoelectron spin-flipping and texture manipulation in a topological insulator". *Nat. Phys.* **9** (2013), pp. 293–298.

[32] J. Kirschner, R. Feder, and J. F. Wendelken. "Electron spin polarization in energy-and angle-resolved photoemission from W (001): Experiment and theory". *Phys. Rev. Lett.* **47** (1981), pp. 614–617.

[33] E. Tamura, W. Piepke, and R. Feder. "New spin-polarization effect in photoemission from nonmagnetic surfaces". *Phys. Rev. Lett.* **59** (1987), pp. 934–937.

[34] U. Heinzmann and J. H. Dil. "Spin-orbit-induced photoelectron spin polarization in angle-resolved photoemission from both atomic and condensed matter targets". *J. Phys.: Condens. Matter* **24** (2012), p. 173001.

[35] C. M. Schneider, J. Garbe, K. Bethke, and J. Kirschner. "Symmetry-dependent alignment of the electron-spin polarization vector due to electronic band hybridization observed in photoemission from Ag (100)". *Phys. Rev. B* **39** (1989), pp. 1031–1035.

[36] H. Maaß, S. Schreyeck, S. Schatz, S. Fiedler, C. Seibel, P. Lutz, G. Karczewski, H. Bentmann, C. Gould, K. Brunner, L. W. Molenkamp, and F. Reinert. "Electronic structure and morphology of epitaxial Bi_2Te_2Se topological insulator films". *J. Appl. Phys.* **116** (2014), p. 193708.

[37] H. Maaß, H. Bentmann, C. Seibel, C. Tusche, S. V. Eremeev, T. R. F. Peixoto, O. E. Tereshchenko, K. A. Kokh, E. V. Chulkov, J. Kirschner, and F. Reinert. "Spin-texture inversion in the giant Rashba semiconductor BiTeI". *Nat. Commun.* **7** (2016), p. 11621.

[38] E. I. Rashba. "Properties of semiconductors with an extremum loop. 1. Cyclotron and combinational resonance in a magnetic field perpendicular to the plane of the loop". *Sov. Phys. Solid State* **2** (1960), p. 1109.

[39] Y. A. Bychkov and E. I. Rashba. "Properties of a 2D electron gas with lifted spectral degeneracy". *JETP Lett.* **39** (1984), pp. 66–69.

[40] J. J. Sakurai. *Advanced Quantum Mechanics*. Addison-Wesley Publishing Company, 1967.

[41] F. Schwabl. *Quantum Mechanics*. 4th ed. Springer, 1992.

[42] J. F. Moudler, W. F. Stickle, P. E. Sobol, and K. D. Bomben. *Handbook of X-Ray Photoelectron Spectroscopy*. Eden Prairie: Perkin-Elmer, 1992.

[43] F. Bloch. "Über die Quantenmechanik der Elektronen in Kristallgittern". *Z. Phys.* **52** (1929), pp. 555–600.

[44] C. Kittel. *Einführung in die Festkörperphysik*. 6th ed. München: R. Oldenbourg Verlag, 1983.

[45] G. Nicolay. "Vielteilchenanregungen nahe der Fermienergie am Beispielsystem der Shockley-Oberflächenzustände". PhD thesis. Saarbrücken: Universität des Saarlandes, 2002.

[46] M. Gradhand, M. Czerner, D. V. Fedorov, P. Zahn, B. Y. Yavorsky, L. Szunyogh, and I. Mertig. "Spin polarization on Fermi surfaces of metals by the KKR method". *Physical Review B* **80** (2009), p. 224413.

[47] M. Nagano, A. Kodama, T Shishidou, and T Oguchi. "A first-principles study on the Rashba effect in surface systems". *J. Phys.: Condens. Matter* **21** (2009), p. 064239.

[48] G. Dresselhaus. "Spin-orbit coupling effects in zinc blende structures". *Phys. Rev.* **100** (1955), pp. 580–586.

[49] E. E. Krasovskii. "Spin-orbit coupling at surfaces and 2D materials". *J. Phys.: Condens. Matter* **27** (2015), p. 493001.

[50] S. LaShell, B. McDougall, and E. Jensen. "Spin splitting of an Au (111) surface state band observed with angle resolved photoelectron spectroscopy". *Phys. Rev. Lett.* **77** (1996), pp. 3419–3422.

[51] G. Nicolay, F. Reinert, S. Hüfner, and P. Blaha. "Spin-orbit splitting of the *L*-gap surface state on Au(111) and Ag(111)". *Phys. Rev. B* **65** (2001), p. 033407.

[52] F. Reinert, G. Nicolay, S. Schmidt, D. Ehm, and S. Hüfner. "Direct measurements of the *L*-gap surface states on the (111) face of noble metals by photoelectron spectroscopy". *Phys. Rev. B* **63** (2001), p. 115415.

[53] G. Bihlmayer, Y. Koroteev, P. Echenique, E. Chulkov, and S. Blügel. "The Rashba-effect at metallic surfaces". *Surf. Sci.* **600** (2006), pp. 3888–3891.

[54] A. Tanaka, M. Hatano, K. Takahashi, H. Sasaki, S. Suzuki, and S. Sato. "Bulk and surface electronic structures of the semimetal Bi studied by angle-resolved photoemission spectroscopy". *Phys. Rev. B* **59** (1999), pp. 1786–1791.

[55] C. R. Ast and H. Höchst. "Fermi Surface of Bi(111) Measured by Photoemission Spectroscopy". *Phys. Rev. Lett.* **87** (2001), p. 177602.

[56] Y. M. Koroteev, G. Bihlmayer, J. E. Gayone, E. V. Chulkov, S. Blügel, P. M. Echenique, and P. Hofmann. "Strong Spin-Orbit Splitting on Bi Surfaces". *Phys. Rev. Lett.* **93** (2004), p. 046403.

[57] K. Sugawara, T. Sato, S. Souma, T. Takahashi, M. Arai, and T. Sasaki. "Fermi Surface and Anisotropic Spin-Orbit Coupling of Sb(111) Studied by Angle-Resolved Photoemission Spectroscopy". *Phys. Rev. Lett.* **96** (2006), p. 046411.

[58] A. Varykhalov, D. Marchenko, M. R. Scholz, E. D. L. Rienks, T. K. Kim, G. Bihlmayer, J. Sánchez-Barriga, and O. Rader. "Ir(111) Surface State with Giant Rashba Splitting Persists under Graphene in Air". *Phys. Rev. Lett.* **108** (2012), p. 066804.

[59] A. Tamai, W. Meevasana, P. D. C. King, C. W. Nicholson, A. de la Torre, E. Rozbicki, and F. Baumberger. "Spin-orbit splitting of the Shockley surface state on Cu(111)". *Phys. Rev. B* **87** (2013), p. 075113.

[60] C. Ast, J. Henk, A. Ernst, L. Moreschini, M. Falub, D. Pacilé, P. Bruno, K. Kern, and M. Grioni. "Giant Spin Splitting through Surface Alloying". *Phys. Rev. Lett.* **98** (2007), p. 186807.

[61] G. Bihlmayer, S. Blügel, and E. Chulkov. "Enhanced Rashba spin-orbit splitting in Bi/Ag(111) and Pb/Ag(111) surface alloys from first principles". *Phys. Rev. B* **75** (2007), p. 195414.

[62] H. Bentmann, F. Forster, G. Bihlmayer, E. V. Chulkov, L. Moreschini, M. Grioni, and F. Reinert. "Origin and manipulation of the Rashba splitting in surface alloys". *Europhys. Lett.* **87** (2009), p. 37003.

[63] H. Bentmann, T. Kuzumaki, G. Bihlmayer, S. Blügel, E. V. Chulkov, F. Reinert, and K. Sakamoto. "Spin orientation and sign of the Rashba splitting in Bi/Cu(111)". *Phys. Rev. B* **84** (2011), p. 115426.

[64] K. Ishizaka, M. S. Bahramy, H. Murakawa, M. Sakano, T. Shimojima, T. Sonobe, K. Koizumi, S. Shin, H. Miyahara, A. Kimura, K. Miyamoto, T. Okuda, H. Namatame, M. Taniguchi, R. Arita, N. Nagaosa, K. Kobayashi, Y. Murakami, R. Kumai, Y. Kaneko, Y. Onose, and Y. Tokura. "Giant Rashba-type spin splitting in bulk BiTeI". *Nat. Mater.* **10** (2011), pp. 521–526.

[65] M. S. Bahramy, R. Arita, and N. Nagaosa. "Origin of giant bulk Rashba splitting: Application to BiTeI". *Phys. Rev. B* **84** (2011), 041202(R).

[66] A. Crepaldi, L. Moreschini, G. Autès, C. Tournier-Colletta, S. Moser, N. Virk, H. Berger, P. Bugnon, Y. J. Chang, K. Kern, A. Bostwick, E. Rotenberg, O. V. Yazyev, and M. Grioni. "Giant Ambipolar Rashba Effect in the Semiconductor BiTeI". *Phys. Rev. Lett.* **109** (2012), p. 096803.

[67] S. V. Eremeev, I. P. Rusinov, I. A. Nechaev, and E. V. Chulkov. "Rashba split surface states in BiTeBr". *New J. Phys.* **15** (2013), p. 075015.

[68] S. V. Eremeev, I. A. Nechaev, Y. M. Koroteev, P. M. Echenique, and E. V. Chulkov. "Ideal Two-Dimensional Electron Systems with a Giant Rashba-Type Spin Splitting in Real Materials: Surfaces of Bismuth Tellurohalides". *Phys. Rev. Lett.* **108** (2012), p. 246802.

[69] L. Isaev, Y. H. Moon, and G. Ortiz. "Bulk-boundary correspondence in three-dimensional topological insulators". *Phys. Rev. B* **84** (2011), p. 075444.

[70] C. L. Kane and E. J. Mele. "Quantum Spin Hall Effect in Graphene". *Phys. Rev. Lett.* **95** (2005), p. 226801.

[71] L. Fu and C. L. Kane. "Time reversal polarization and a Z_2 adiabatic spin pump". *Phys. Rev. B* **74** (2006), p. 195312.

[72] J. E. Moore and L. Balents. "Topological invariants of time-reversal-invariant band structures". *Phys. Rev. B* **75** (2007), p. 121306.

[73] M. König, S. Wiedmann, C. Brüne, A. Roth, H. Buhmann, L. W. Molenkamp, X.-L. Qi, and S.-C. Zhang. "Quantum Spin Hall Insulator State in HgTe Quantum Wells". *Science* **318** (2007), pp. 766–770.

[74] B. A. Bernevig, T. L. Hughes, and S.-C. Zhang. "Quantum Spin Hall Effect and Topological Phase Transition in HgTe Quantum Wells". *Science* **314** (2006), pp. 1757–1761.

[75] D. Hsieh, D. Qian, L. Wray, Y. Xia, Y. S. Hor, R. J. Cava, and M. Z. Hasan. "A topological Dirac insulator in a quantum spin Hall phase". *Nature* **452** (2008), pp. 970–974.

[76] Y. L. Chen, J. G. Analytis, J.-H. Chu, Z. K. Liu, S.-K. Mo, X. L. Qi, H. J. Zhang, D. H. Lu, X. Dai, Z. Fang, S. C. Zhang, I. R. Fisher, Z. Hussain, and Z.-X. Shen. "Experimental Realization of a Three-Dimensional Topological Insulator, Bi_2Te_3". *Science* **325** (2009), pp. 178–181.

[77]   N. F. Mott. "Scattering of Fast Electrons by Atomic Nuclei". *Proc. R. Soc. London, Ser. A* **124** (1929), pp. 425–441.

[78]   C. G. Shull, C. T. Chase, and F. Myers. "Electron Polarization". *Phys. Rev.* **63** (1943), pp. 29–37.

[79]   G. C. Burnett, T. J. Monroe, and F. B. Dunning. "High-efficiency retarding-potential Mott polarization analyzer". *Rev. Sci. Instrum.* **65** (1994), pp. 1893–1896.

[80]   M. H. Berntsen, P. Palmgren, M. Leandersson, A. Hahlin, J. Åhlund, B. Wannberg, M. Månsson, and O. Tjernberg. "A spin- and angle-resolving photoelectron spectrometer". *Rev. of Sci. Instrum.* **81** (2010), p. 035104.

[81]   M. Hoesch, T. Greber, V. N. Petrov, M. Muntwiler, M. Hengsberger, W. Auwärter, and J. Osterwalder. "Spin-polarized Fermi surface mapping". *J. Electron Spectrosc. Relat. Phenom.* **124** (2002), pp. 263–279.

[82]   J. Kirschner and R. Feder. "Spin polarization in double diffraction of low-energy electrons from W (001): experiment and theory". *Phys. Rev. Lett.* **42** (1979), pp. 1008–1011.

[83]   T. Okuda, K. Miyamoto, H. Miyahara, K. Kuroda, A. Kimura, H. Namatame, and M. Taniguchi. "Efficient spin resolved spectroscopy observation machine at Hiroshima Synchrotron Radiation Center". *Rev. Sci. Instrum.* **82** (2011), p. 103302.

[84]   U. Fano. "Spin orientation of photoelectrons ejected by circularly polarized light". *Phys. Rev.* **178** (1969), pp. 131–136.

[85]   U. Heinzmann, J. Kessler, and J. Lorenz. "Elektronen-Spinpolarisation bei der Photoionisation unpolarisierter Cäsiumatome mit zirkularpolarisiertem Licht". *Z. Phys.* **240** (1970), pp. 42 –61.

[86]   U. Heinzmann, J. Kessler, and J. Lorenz. "Wavelength Dependence of the Fano Effect". *Phys. Rev. Lett.* **25** (1970), p. 1325.

[87]   B. Schmiedeskamp, B. Kessler, N. Müller, G. Schönhense, and U. Heinzmann. "Spin-resolved photoemission from Pd(111)". *Solid State Commun.* **65** (1988), pp. 665–670.

[88]   J. Garbe and J. Kirschner. "Spin-resolved photoemission from the (111) face of platinum". *Phys. Rev. B* **39** (1989), pp. 1530 –1534.

[89] G. Schönhense, A. Eyers, U. Friess, F. Schäfers, and U. Heinzmann. "Highly Spin-Polarized Photoemission near Threshold from Physisorbed Xenon and Krypton Atoms". *Phys. Rev. Lett.* **54** (1985), pp. 547–550.

[90] G. Schönhense. "Photoelectron spin-polarization spectroscopy: A new method in adsorbate physics". *Appl. Phys. A* **41** (1986), pp. 39–60.

[91] H. P. Oepen, K. Hünlich, and J. Kirschner. "Spin-Dependent Photoemission Intensities from Solids". *Phys. Rev. Lett.* **56** (1986), pp. 496 –499.

[92] J. Garbe and J. Kirschner. "Spin-dependent photoemission intensities from platinum (111)". *Phys. Rev. B* **39** (1989), pp. 9859–9864.

[93] C. Westphal, J. Bansmann, M. Getzlaff, and G. Schönhense. "Circular dichroism in the angular distribution of photoelectrons from oriented CO molecules". *Phys. Rev. Lett.* **63** (1989), pp. 151–154.

[94] J. Bansmann, C. Ostertag, G. Schönhense, F. Fegel, C. Westphal, M. Getzlaff, F. Schäfers, and H. Petersen. "Circular dichroism in x-ray photoemission from core levels of nonmagnetic species". *Phys. Rev. B* **46** (1992), pp. 13496–13500.

[95] G. Schönhense. "Circular dichroism and spin polarization in photoemission from adsorbates and non-magnetic solids". *Phys. Scr.* **1990** (1990), pp. 255–275.

[96] A. Eyers, F. Schäfers, G. Schönhense, U. Heinzmann, H. P. Oepen, K. Hünlich, J. Kirschner, and G. Borstel. "Characterization of symmetry properties of Pt (111) electron bands by means of angle-, energy-, and spin-resolved photoemission with circularly polarized synchrotron radiation". *Phys. Rev. Lett.* **52** (1984), pp. 1559–1562.

[97] C. Heckenkamp, F. Schäfers, G. Schönhense, and U. Heinzmann. "Angular Dependence of the Spin-Polarization Transfer from Circularly Polarized Synchrotron Radiation onto Photoelectrons from Atomic Xe $5p^6$". *Phys. Rev. Lett.* **52** (1984), pp. 421–424.

[98] B. Kessler, N. Müller, B. Schmiedeskamp, B. Vogt, and U. Heinzmann. "Spin-resolved off-normal photoemission from xenon adsorbates in comparison with free-atom photoionization". *Z. Phys. D: Atoms, Molecules and Clusters* **17** (1990), pp. 11–16.

[99] B. Schmiedeskamp, B. Vogt, and U. Heinzmann. "Experimental Verification of a New Spin-Polarization Effect in Photoemission: Polarized Photoelectrons from

Pt(111) with Linearly Polarized Radiation in Normal Incidence and Normal Emission". *Phys. Rev. Lett.* **60** (1988), pp. 651–654.

[100] U. Heinzmann, G. Schönhense, and J. Kessler. "Polarization of Photoelectrons Ejected by Unpolarized Light from Xenon Atoms". *Phys. Rev. Lett.* **42** (1979), pp. 1603 –1605.

[101] C. M. Lee. "Spin polarization and angular distribution of photoelectrons in the Jacob-Wick helicity formalism. Application to autoionization resonances". *Phys. Rev. A* **10** (1974), pp. 1598–1604.

[102] N. A. Cherepkov. "Angular distribution of photoelectrons with a given spin orientation". *Zh. Eksp. Teor. Fiz.* **65** (1973), pp. 933 –946.

[103] H. Hertz. "Ueber einen Einfluss des ultravioletten Lichtes auf die electrische Entladung". *Ann. Phys.* **267** (1887), pp. 983–1000.

[104] A. Einstein. "Über einen die Erzeugung und Verwandlung des Lichtes betreffenden heuristischen Gesichtspunkt". *Ann. Phys.* **322** (1905), pp. 132–148.

[105] S. Hüfner. *Photoelectron Spectroscopy - Principles and applications*. 2nd ed. Springer, 1995.

[106] M. P. Seah and W. A. Dench. "Quantitative electron spectroscopy of surfaces: a standard data base for electron inelastic mean free paths in solids". *Surface and interface analysis* **1** (1979), pp. 2–11.

[107] A. Damascelli. "Probing the electronic structure of complex systems by ARPES". *Phys. Scr.* **T109** (2004), pp. 61–74.

[108] A. Damascelli, Z. Hussain, and Z.-X. Shen. "Angle-resolved photoemission studies of the cuprate superconductors". *Rev. Mod. Phys.* **75** (2003), pp. 473–541.

[109] G. Borstel. "Theoretical aspects of photoemission". *Appl. Phys. A* **38** (1985), pp. 193–204.

[110] F. Reinert and S. Hüfner. "Photoemission spectroscopy-from early days to recent applications". *New J. Phys.* **7** (2005), pp. 97–97.

[111] J. Kessler. *Polarized Electrons*. 2nd ed. Springer, 1985.

[112] P. D. Johnson. "Spin-polarized photoemission". *Rep. Prog. Phys.* **60** (1997), pp. 1217–1304.

[113] T. E. Feuchtwang, P. H. Cutler, and D. Nagy. "A review of the theoretical and experimental analyses of electron spin polarization in ferromagnetic transition metals: II. New theoretical results for the analysis of ESP in field emission, photoemission, and tunneling". *Surf. Sci.* **75** (1978), pp. 490–528.

[114] C. N. Berglund and W. E. Spicer. "Photoemission studies of copper and silver: theory". *Phys. Rev.* **136** (1964), pp. 1030–1044.

[115] R. Feder. "Spin-polarised low-energy electron diffraction". *J. Phys. C: Solid State Phys.* **14** (1981), pp. 2049–2091.

[116] P. D. Johnson. "Spin Polarized Photoemission". *Annu. Rev. Mater. Sci.* **25** (1995), pp. 455–485.

[117] P. D. Johnson and G. Güntherodt. *Spin-polarized Photoelectron Spectroscopy as a Probe of Magnetic Systems*. Wiley Online Library, 2006.

[118] A. Takayama. "Basic Principle of Photoemission Spectroscopy and Spin Detector". *High-Resolution Spin-Resolved Photoemission Spectrometer and the Rashba Effect in Bismuth Thin Films*. Tokyo: Springer Japan, 2015, pp. 15–30.

[119] D. Tillmann, R. Thiel, and E. Kisker. "Very-low-energy spin-polarized electron diffraction from Fe (001)". *Z. Phys. B: Condens. Matter* **77** (1989), pp. 1–2.

[120] F. U. Hillebrecht, R. M. Jungblut, L. Wiebusch, C. Roth, H. B. Rose, D. Knabben, C. Bethke, N. B. Weber, S. Manderla, U. Rosowski, and E. Kisker. "High-efficiency spin polarimetry by very-low-energy electron scattering from Fe(100) for spin-resolved photoemission". *Rev. Sci. Instrum.* **73** (2002), pp. 1229–1234.

[121] R. Bertacco, M. Merano, and F. Ciccacci. "Spin dependent electron absorption in Fe(001)-p(1×1)O: A new candidate for a stable and efficient electron polarization analyzer". *Appl. Phys. Lett.* **72** (1998), pp. 2050–2052.

[122] R. Bertacco, M. Marcon, G. Trezzi, L. Duò, and F. Ciccacci. "Spin and energy analysis of electron beams: Coupling a polarimeter based on exchange scattering to a hemispherical analyzer". *Rev. Sci. Instrum.* **73** (2002), pp. 3867–3871.

[123] A. Winkelmann, D. Hartung, H. Engelhard, C.-T. Chiang, and J. Kirschner. "High efficiency electron spin polarization analyzer based on exchange scattering at Fe/W(001)". *Rev. Sci. Instrum.* **79** (2008), p. 083303.

131

[124] C. Tusche, A. Krasyuk, and J. Kirschner. "Spin resolved bandstructure imaging with a high resolution momentum microscope". *Ultramicroscopy* **159** (2015), pp. 520–529.

[125] D. Vasilyev, C. Tusche, F. Giebels, H. Gollisch, R. Feder, and J. Kirschner. "Low-energy electron reflection from Au-passivated Ir(001) for application in imaging spin-filters". *J. Electron Spectrosc. Relat. Phenom.* **199** (2015), pp. 10–18.

[126] C. Tusche, M. Ellguth, A. A. Ünal, C.-T. Chiang, A. Winkelmann, A. Krasyuk, M. Hahn, G. Schönhense, and J. Kirschner. "Spin resolved photoelectron microscopy using a two-dimensional spin-polarizing electron mirror". *Appl. Phys. Lett.* **99** (2011), p. 032505.

[127] M. Kolbe, P. Lushchyk, B. Petereit, H. J. Elmers, G. Schönhense, A. Oelsner, C. Tusche, and J. Kirschner. "Highly Efficient Multichannel Spin-Polarization Detection". *Phys. Rev. Lett.* **107** (2011), p. 207601.

[128] C. Tusche, M. Ellguth, A. Krasyuk, A. Winkelmann, D. Kutnyakhov, P. Lushchyk, K. Medjanik, G. Schönhense, and J. Kirschner. "Quantitative spin polarization analysis in photoelectron emission microscopy with an imaging spin filter". *Ultramicroscopy* **130** (2013), pp. 70–76.

[129] F. Reinert. "Spin-orbit interaction in the photoemission spectra of noble metal surface states". *J. Phys.: Condens. Matter* **15** (2003), S693.

[130] L. Fu. "Hexagonal Warping Effects in the Surface States of the Topological Insulator Bi_2Te_3". *Phys. Rev. Lett.* **103** (2009), p. 266801.

[131] K. Kokh, B. Nenashev, A. Kokh, and G. Shvedenkov. "Application of a rotating heat field in Bridgman-Stockbarger crystal growth". *J. Cryst. Growth* **275** (2005), e2129–e2134.

[132] Z. Ren, A. A. Taskin, S. Sasaki, K. Segawa, and Y. Ando. "Large bulk resistivity and surface quantum oscillations in the topological insulator Bi_2Te_2Se". *Phys. Rev. B* **82** (2010), 241306(R).

[133] K. Miyamoto, A. Kimura, T. Okuda, H. Miyahara, K. Kuroda, H. Namatame, M. Taniguchi, S. V. Eremeev, T. V. Menshchikova, E. V. Chulkov, K. A. Kokh, and O. E. Tereshchenko. "Topological Surface States with Persistent High Spin Polarization across the Dirac Point in Bi_2Te_2Se and Bi_2Se_2Te". *Phys. Rev. Lett.* **109** (2012), p. 166802.

132

[134] C. Chen, S. He, H. Weng, W. Zhang, L. Zhao, H. Liu, X. Jia, D. Mou, S. Liu, and J. He. "Robustness of topological order and formation of quantum well states in topological insulators exposed to ambient environment". *Proc. Natl. Acad. Sci.* **109** (2012), pp. 3694–3698.

[135] P. D. C. King, R. C. Hatch, M. Bianchi, R. Ovsyannikov, C. Lupulescu, G. Landolt, B. Slomski, J. H. Dil, D. Guan, J. L. Mi, E. D. L. Rienks, J. Fink, A. Lindblad, S. Svensson, S. Bao, G. Balakrishnan, B. B. Iversen, J. Osterwalder, W. Eberhardt, F. Baumberger, and P. Hofman. "Large tunable Rashba spin splitting of a two-dimensional electron gas in Bi_2Se_3". *Phys. Rev. Lett.* **107** (2011), p. 096802.

[136] H. M. Benia, C. Lin, K. Kern, and C. R. Ast. "Reactive Chemical Doping of the Bi_2Se_3 Topological Insulator". *Phys. Rev. Lett.* **107** (2011), p. 177602.

[137] M. Bianchi, R. C. Hatch, J. Mi, B. B. Iversen, and P. Hofmann. "Simultaneous Quantization of Bulk Conduction and Valence States through Adsorption of Nonmagnetic Impurities on Bi_2Se_3". *Phys. Rev. Lett.* **107** (2011), p. 086802.

[138] L. Barreto, L. Kühnemund, F. Edler, C. Tegenkamp, J. Mi, M. Bremholm, B. B. Iversen, C. Frydendahl, M. Bianchi, and P. Hofmann. "Surface-Dominated Transport on a Bulk Topological Insulator". *Nano Lett.* **14** (2014), pp. 3755–3760.

[139] M. Neupane, S.-Y. Xu, L. A. Wray, A. Petersen, R. Shankar, N. Alidoust, C. Liu, A. Fedorov, H. Ji, J. M. Allred, Y. S. Hor, T.-R. Chang, H.-T. Jeng, H. Lin, A. Bansil, R. J. Cava, and M. Z. Hasan. "Topological surface states and Dirac point tuning in ternary topological insulators". *Phys. Rev. B* **85** (2012), p. 235406.

[140] M. Bianchi, D. Guan, S. Bao, J. Mi, B. B. Iversen, P. D. King, and P. Hofmann. "Coexistence of the topological state and a two-dimensional electron gas on the surface of Bi_2Se_3". *Nat. Commun.* **1** (2010), p. 128.

[141] Measurement performed by Oleg Tereshchenko at BESSY.

[142] S. Fiedler, T. Bathon, S. V. Eremeev, O. E. Tereshchenko, K. A. Kokh, E. V. Chulkov, P. Sessi, H. Bentmann, M. Bode, and F. Reinert. "Termination-dependent surface properties in the giant-Rashba semiconductors BiTe X (X = Cl , Br, I)". *Phys. Rev. B* **92** (2015), p. 235430.

[143] S. Fiedler, L. El-Kareh, S. Eremeev, O. E. Tereshchenko, C. Seibel, P. Lutz, K. A. Kokh, E. V. Chulkov, T. V. Kuznetsova, V. I. Grebennikov, H. Bentmann,

M. Bode, and F. Reinert. "Defect and structural imperfection effects on the electronic properties of BiTeI surfaces". *New J. Phys.* **16** (2014), p. 075013.

[144]   G. Landolt, S. V. Eremeev, Y. M. Koroteev, B. Slomski, S. Muff, T. Neupert, M. Kobayashi, V. N. Strocov, T. Schmitt, Z. S. Aliev, M. B. Babanly, I. R. Amiraslanov, E. V. Chulkov, J. Osterwalder, and J. H. Dil. "Disentanglement of Surface and Bulk Rashba Spin Splittings in Noncentrosymmetric BiTeI". *Phys. Rev. Lett.* **109** (2012), p. 116403.

[145]   Z. Zhu, Y. Cheng, and U. Schwingenschlögl. "Orbital-dependent Rashba coupling in bulk BiTeCl and BiTeI". *New J. Phys.* **15** (2013), p. 023010.

[146]   J. Dalmas, H. Oughaddou, G. Le Lay, B. Aufray, G. Tréglia, C. Girardeaux, J. Bernardini, J. Fujii, and G. Panaccione. "Photoelectron spectroscopy study of Pb/Ag(111) in the submonolayer range". *Surf. Sci.* **600** (2006), pp. 1227–1230.

[147]   H. Bentmann. "Spin-Bahn-Kopplung in Grenzschichten: Mikroskopische Zusammenhänge und Strategien zur Manipulation". PhD thesis. Julius-Maximilians-Universität Würzburg, 2012.

[148]   D. Pacilé, C. R. Ast, M. Papagno, C. Da Silva, L. Moreschini, M. Falub, A. P. Seitsonen, and M. Grioni. "Electronic structure of an ordered Pb/Ag (111) surface alloy: Theory and experiment". *Phys. Rev. B* **73** (2006), p. 245429.

[149]   L. Moreschini, A. Bendounan, H. Bentmann, M. Assig, K. Kern, F. Reinert, J. Henk, C. Ast, and M. Grioni. "Influence of the substrate on the spin-orbit splitting in surface alloys on (111) noble-metal surfaces". *Phys. Rev. B* **80** (2009), p. 035438.

[150]   G. Landolt, S. Schreyeck, S. V. Eremeev, B. Slomski, S. Muff, J. Osterwalder, E. V. Chulkov, C. Gould, G. Karczewski, K. Brunner, H. Buhmann, L. W. Molenkamp, and J. H. Dil. "Spin Texture of Bi_2Se_3 Thin Films in the Quantum Tunneling Limit". *Phys. Rev. Lett.* **112** (2014), p. 057601.

[151]   Z.-H. Zhu, C. N. Veenstra, G. Levy, A. Ubaldini, P. Syers, N. P. Butch, J. Paglione, M. W. Haverkort, I. S. Elfimov, and A. Damascelli. "Layer-By-Layer Entangled Spin-Orbital Texture of the Topological Surface State in Bi_2Se_3". *Phys. Rev. Lett.* **110** (2013), p. 216401.

[152]   H. Mirhosseini, J. Henk, A. Ernst, S. Ostanin, C.-T. Chiang, P. Yu, A. Winkelmann, and J. Kirschner. "Unconventional spin topology in surface alloys with Rashba-type spin splitting". *Phys. Rev. B* **79** (2009), p. 245428.

[153]   Y. Cao, J. A. Waugh, X.-W. Zhang, J.-W. Luo, Q. Wang, T. J. Reber, S. K. Mo, Z. Xu, A. Yang, J. Schneeloch, G. D. Gu, M. Brahlek, N. Bansal, S. Oh, A. Zunger, and D. S. Dessau. "Mapping the orbital wavefunction of the surface states in three-dimensional topological insulators". *Nat. Phys.* **9** (2013), pp. 499–504.

[154]   Z. Xie, S. He, C. Chen, Y. Feng, H. Yi, A. Liang, L. Zhao, D. Mou, J. He, Y. Peng, X. Liu, Y. Liu, G. Liu, X. Dong, L. Yu, J. Zhang, S. Zhang, Z. Wang, F. Zhang, F. Yang, Q. Peng, X. Wang, C. Chen, Z. Xu, and X. J. Zhou. "Orbital-selective spin texture and its manipulation in a topological insulator". *Nat. Commun.* **5** (2014), p. 3382.

[155]   L. El-Kareh, G. Bihlmayer, A. Buchter, H. Bentmann, S. Blügel, F. Reinert, and M. Bode. "A combined experimental and theoretical study of Rashba-split surface states on the $(\sqrt{3} \times \sqrt{3})$ Pb/Ag(111)R30° surface". *New J. Phys.* **16** (2014), p. 045017.

[156]   S. Schirone, E. Krasovskii, G. Bihlmayer, R. Piquerel, P. Gambardella, and A. Mugarza. "Spin-Flip and Element-Sensitive Electron Scattering in the $BiAg_2$ Surface Alloy". *Phys. Rev. Lett.* **114** (2015), p. 166801.

[157]   Z.-H. Zhu, C. Veenstra, S. Zhdanovich, M. Schneider, T. Okuda, K. Miyamoto, S.-Y. Zhu, H. Namatame, M. Taniguchi, M. Haverkort, I. Elfimov, and A. Damascelli. "Photoelectron Spin-Polarization Control in the Topological Insulator Bi_2Se_3". *Phys. Rev. Lett.* **112** (2014), p. 076802.

[158]   J. Sánchez-Barriga, A. Varykhalov, J. Braun, S.-Y. Xu, N. Alidoust, O. Kornilov, J. Minár, K. Hummer, G. Springholz, G. Bauer, R. Schumann, L. Yashina, H. Ebert, M. Hasan, and O. Rader. "Photoemission of Bi_2Se_3 with Circularly Polarized Light: Probe of Spin Polarization or Means for Spin Manipulation?" *Phys. Rev. X* **4** (2014), p. 011046.

[159]   H. Zhang, C.-X. Liu, and S.-C. Zhang. "Spin-Orbital Texture in Topological Insulators". *Phys. Rev. Lett.* **111** (2013), p. 066801.

[160]   S. Wissing, A. Schmidt, H. Mirhosseini, J. Henk, C. Ast, and M. Donath. "Ambiguity of Experimental Spin Information from States with Mixed Orbital Symmetries". *Phys. Rev. Lett.* **113** (2014), p. 116402.

[161]   Q.-K. Xue. "Topological insulators: Full spin ahead for photoelectrons". *Nat. Phys.* **9** (2013), pp. 265–266.

[162] T. Maniv and H. Metiu. "Electrodynamics at a metal surface. II. Fresnel formulas for the electromagnetic field at the interface for a jellium model within the random phase approximation". *J. Chem. Phys.* **76** (1982), pp. 2697–2713.

[163] J. Henk, A. Ernst, S. V. Eremeev, E. V. Chulkov, I. V. Maznichenko, and I. Mertig. "Complex Spin Texture in the Pure and Mn-Doped Topological Insulator Bi_2Te_3". *Phys. Rev. Lett.* **108** (2012), p. 206801.

[164] S. Souma, K. Kosaka, T. Sato, M. Komatsu, A. Takayama, T. Takahashi, M. Kriener, K. Segawa, and Y. Ando. "Direct Measurement of the Out-of-Plane Spin Texture in the Dirac-Cone Surface State of a Topological Insulator". *Phys. Rev. Lett.* **106** (2011), p. 216803.

[165] K. Sakamoto, T. Oda, A. Kimura, K. Miyamoto, M. Tsujikawa, A. Imai, N. Ueno, H. Namatame, M. Taniguchi, P. E. J. Eriksson, and R. I. G. Uhrberg. "Abrupt Rotation of the Rashba Spin to the Direction Perpendicular to the Surface". *Phys. Rev. Lett.* **102** (2009), p. 096805.

[166] P. Höpfner, J. Schäfer, A. Fleszar, J. H. Dil, B. Slomski, F. Meier, C. Loho, C. Blumenstein, L. Patthey, W. Hanke, and R. Claessen. "Three-Dimensional Spin Rotations at the Fermi Surface of a Strongly Spin-Orbit Coupled Surface System". *Phys. Rev. Lett.* **108** (2012), p. 186801.

[167] C. Jozwiak, Y. L. Chen, A. V. Fedorov, J. G. Analytis, C. R. Rotundu, A. K. Schmid, J. D. Denlinger, Y.-D. Chuang, D.-H. Lee, I. R. Fisher, R. J. Birgeneau, Z.-X. Shen, Z. Hussain, and A. Lanzara. "Widespread spin polarization effects in photoemission from topological insulators". *Phys. Rev. B* **84** (2011), p. 165113.

[168] Z.-H. Zhu, C. N. Veenstra, S. Zhdanovich, M. Schneider, T. Okuda, K. Miyamoto, S.-Y. Zhu, H. Namatame, M. Taniguchi, M. W. Haverkort, I. S. Elfimov, and A. Damascelli. "Supplementary Information for: Photoelectron Spin-Polarization Control in the Topological Insulator Bi_2Se_3". *Phys. Rev. Lett.* **112** (2014), p. 076802.

[169] M. Lindroos, S. Sahrakorpi, and A. Bansil. "Matrix element effects in angle-resolved photoemission from $Bi_2Sr_2CaCu_2O_8$: Energy and polarization dependencies, final state spectrum, spectral signatures of specific transitions, and related issues". *Phys. Rev. B* **65** (2002), p. 054514.

[170] W. Eberhardt and F. J. Himpsel. "Dipole selection rules for optical transitions in the fcc and bcc lattices". *Phys. Rev. B* **21** (1980), pp. 5572–5576.

[171] M. Mulazzi, M. Hochstrasser, M. Corso, I. Vobornik, J. Fujii, J. Osterwalder, J. Henk, and G. Rossi. "Matrix element effects in angle-resolved valence band photoemission with polarized light from the Ni(111) surface". *Phys. Rev. B* **74** (2006), p. 035118.

[172] E. E. Krasovskii, V. N. Strocov, N. Barrett, H. Berger, W. Schattke, and R. Claessen. "Band mapping in the one-step photoemission theory: Multi-Bloch-wave structure of final states and interference effects". *Phys. Rev. B* **75** (2007).

[173] E. E. Krasovskii and W. Schattke. "Calculation of the wave functions for semi-infinite crystals with linear methods of band theory". *Phys. Rev. B* **59** (1999), R15609.

[174] I. Gierz, J. Henk, H. Höchst, C. R. Ast, and K. Kern. "Illuminating the dark corridor in graphene: Polarization dependence of angle-resolved photoemission spectroscopy on graphene". *Phys. Rev. B* **83** (2011), 121408(R).

[175] E. L. Shirley, L. J. Terminello, A. Santoni, and F. J. Himpsel. "Brillouin-zone-selection effects in graphite photoelectron angular distributions". *Phys. Rev. B* **51** (1995), pp. 13614–13625.

[176] N. Mårtensson, M. Weinelt, O. Karis, M. Magnuson, N. Wassdahl, A. Nilsson, J. Stöhr, and M. Samant. "Coherent and incoherent processes in resonant photoemission". *Applied Physics A: Materials Science & Processing* **65** (1997), pp. 159–167.

[177] S. Hüfner, S.-H. Yang, B. S. Mun, C. S. Fadley, J. Schäfer, E. Rotenberg, and S. D. Kevan. "Observation of the two-hole satellite in Cr and Fe metal by resonant photoemission at the 2p absorption energy". *Phys. Rev. B* **61** (2000), pp. 12582–12585.

[178] M. Weinelt, A. Nilsson, M. Magnuson, T. Wiell, N. Wassdahl, O. Karis, A. Föhlisch, N. Mårtensson, J. Stöhr, and M. Samant. "Resonant Photoemission at the 2p Edges of Ni: Resonant Raman and Interference Effects". *Phys. Rev. Lett.* **78** (1997), pp. 967–970.

[179] J. Henk, M. Hoesch, J. Osterwalder, A. Ernst, and P. Bruno. "Spin-orbit coupling in the L-gap surface states of Au(111): spin-resolved photoemission experiments and first-principles calculations". *J. Phys.: Condens. Matter* **16** (2004), pp. 7581–7597.

137

[180] E. E. Krasovskii, W. Schattke, P Jiříček, M. Vondráček, O. V. Krasovska, V. N. Antonov, A. P. Shpak, and I. Bartoš. "Photoemission from Al(100) and (111): Experiment and *ab initio* theory". *Phys. Rev. B* **78** (2008), p. 165406.

[181] C.-H. Park and S. G. Louie. "Spin Polarization of Photoelectrons from Topological Insulators". *Phys. Rev. Lett.* **109** (2012), p. 097601.

[182] R. Yu, H. Weng, Z. Fang, and X. Dai. "Pseudospin, real spin, and spin polarization of photoemitted electrons". *Phys. Rev. B* **94** (2016), p. 085123.

[183] M. R. Scholz. "Spin Polarization, Circular Dichroism and Robustness of Topological Surface States: A Photoemission Study". PhD thesis. Universität Potsdam, 2012.

[184] T. Mayer-Kuckuk. *Atomphysik*. Stuttgart: B. G. Teubner, 1977.

[185] F Meier, J. H. Dil, and J Osterwalder. "Measuring spin polarization vectors in angle-resolved photoemission spectroscopy". *New J. Phys.* **11** (2009), p. 125008.

[186] K. Gotlieb, Z. Hussain, A. Bostwick, A. Lanzara, and C. Jozwiak. "Rapid high-resolution spin- and angle-resolved photoemission spectroscopy with pulsed laser source and time-of-flight spectrometer". *Rev. Sci. Instrum.* **84** (2013), p. 093904.

[187] G. Schönhense, K. Medjanik, and H.-J. Elmers. "Space-, time- and spin-resolved photoemission". *J. Electron. Spectrosc. and Relat. Phenom.* **200** (2015), pp. 94–118.

[188] V. N. Strocov, V. N. Petrov, and J. H. Dil. "Concept of a multichannel spin-resolving electron analyzer based on Mott scattering". *J. Synchrotron Radiat.* **22** (2015), pp. 708–716.

[189] R. Yu, W. Zhang, H.-J. Zhang, S.-C. Zhang, X. Dai, and Z. Fang. "Quantized Anomalous Hall Effect in Magnetic Topological Insulators". *Science* **329** (2010), pp. 61–64.

[190] D. Ciudad. "Weyl fermions: Massless yet real". *Nat. Mater.* **14** (2015), p. 863.

[191] S.-Y. Xu, I. Belopolski, D. S. Sanchez, M. Neupane, G. Chang, K. Yaji, Z. Yuan, C. Zhang, K. Kuroda, G. Bian, C. Guo, H. Lu, T.-R. Chang, N. Alidoust, H. Zheng, C.-C. Lee, S.-M. Huang, C.-H. Hsu, H.-T. Jeng, A. Bansil, T. Neupert, F. Komori, T. Kondo, S. Shin, H. Lin, S. Jia, and M. Z. Hasan. "Spin Polarization

and Texture of the Fermi Arcs in the Weyl Fermion Semimetal TaAs". *Phys. Rev. Lett.* **116** (2016), p. 096801.

- **H. Maaß**, H. Bentmann, C. Seibel, C. Tusche, S. V. Eremeev, T. R. F. Peixoto, O. E. Tereshchenko, K. A. Kokh, E. V. Chulkov, J. Kirschner and F. Reinert. "Spin-texture inversion in the giant Rashba semiconductor BiTeI". *Nat. Commun.* **7** (2016), p. 11621.

- **H. Maaß**, S. Schreyeck, S. Schatz, S. Fiedler, C. Seibel, P. Lutz, G. Karczewski, H. Bentmann, C. Gould, K. Brunner, L. W. Molenkamp and F. Reinert. "Electronic structure and morphology of epitaxial Bi_2Te_2Se topological insulator films". *J. Appl. Phys.* **116** (2014), p. 193708.

- C. Seibel, J. Braun, **H. Maaß**, H. Bentmann, J. Minár, T. V. Kuznetsova, K. A. Kokh, O. E. Tereshchenko, T. Okuda, H. Ebert and F. Reinert. "Photoelectron spin polarization in the $Bi_2Te_3(0001)$ topological insulator: Initial- and final-state effects in the photoemission process". *Phys. Rev. B* **93** (2016), p. 245150.

- T. R. F. Peixoto, H. Bentmann, S. Schreyeck, M. Winnerlein, C. Seibel, **H. Maaß**, M. Al-Baidhani, K. Treiber, S. Schatz, S. Grauer, C. Gould, K. Brunner, A. Ernst, L. W. Molenkamp and F. Reinert "Impurity states in the magnetic topological insulator $V:(Bi,Sb)_2Te_3$". *Phys. Rev. B* **94** (2016), p. 195140

- C. Seibel, H. Bentmann, J. Braun, J. Minár, **H. Maaß**, K. Sakamoto, M. Arita, K. Shimada, H. Ebert and F. Reinert. "Connection of a Topological Surface State with the Bulk Continuum in $Sb_2Te_3(0001)$". *Phys. Rev. Lett.* **114** (2015), p. 066802.

- C. Seibel, **H. Maaß**, H. Bentmann, J. Braun, K. Sakamoto, M. Arita, K. Shimada, J. Minár, H. Ebert and F. Reinert. "The Rashba-split surface state of $Sb_2Te_3(0001)$ and its interaction with bulk states". *J. Electron Spectr. Rel. Phenom.* **201** (2015), pp. 110-114.

- C. Seibel, **H. Maaß**, M. Ohtaka, S. Fiedler, C. Jünger, C.-H. Min, H. Bentmann, K. Sakamoto and F. Reinert. "Single Dirac cone on the Cs-covered topological insulator surface $Sb_2Te_3(0001)$". *Phys. Rev. B* **86** (2012), p. 161105(R).

143

Messzeiten wurden selbstverständlich nicht alleine durchgeführt sondern immer im Team. Ganz besonders eng war dabei die Zusammenarbeit mit Dr. Christoph Seibel, der bereits meine Masterarbeit betreute und mir dabei viel grundlegendes Wissen über die Messmethoden beibrachte. Diskussionen physikalischer und nicht-physikalischer Themen, und mal mehr, mal weniger freiwillige Freizeitausflüge während der Messzeiten in Hiroshima und Trieste haben diese anstrengenden Wochen bereichert. Mit von der Partie auf den unterschiedlichen Messzeiten waren auch Dr. Hendrik Bentmann, Dr. Thiago Peixoto, Prof. Friedrich Reinert, Sonja Schatz, Mohammed Al-Baidhani und Katharina Treiber.

Neben dem Würzburgern ist in Bezug auf die Messzeiten auch den jeweiligen Teams an den Beamlines zu danken: Taichi Okuda und Koji Miyamoto sowie Masahi Arita in Hiroshima, Thiagarajan Balasubramanian und Mats Leandersson bei den Max-laboratories in Lund und Jens Viefhaus bei Petra am DESY in Hamburg. Besonders möchte ich hier auch Dr. Christian Tusche meinen Dank aussprechen, der für das Impulsmikroskop in Halle verantwortlich war und bei allen Messungen, Auswertungen und Interpretationen im Zusammenhang mit den Daten aus Halle eng mit uns zusammengearbeitet hat.

Nennen möchte ich hier gerne auch Prof. Andres Santander-Syro, der mir zusammen mit seinem Team an der Beamline Cassiopeia am Synchrotron Soleil in Paris eine der lustigsten Messzeiten beschert hat und mir dabei einige Einblicke in die Welt der Oxide und in bestes alltagstaugliches Französisch ermöglichte.

Bei den Messzeiten an Petra in Hamburg waren unsere Kollegen von der Universität Kiel um Dr. Matthias Kalläne aus der Gruppe von Lutz Kipp ein wichtiger Bestandteil. Neben dem wissenschaftlichen Austausch und der engen Betreuung der Anlage Asphere von Seiten der Kieler, werden mir auch die sich immer wieder einschleichenden Schokoladenmarathons und intensive Quizduelle mit und gegen das Kiel-Team in guter Erinnerung bleiben.

Die theoretischen Daten, die in dieser Arbeit gezeigt wurden, stammen zum einen aus der Hand von Sergey Eremeev, im Falle der Daten an BiTeI, zum anderen von Eugene Krasovskii, für die Modelle zu der Oberflächenlegierung $BiAg_2$. Beiden möchte ich hier meinen Dank aussprechen. Ohne ein theoretisches Modell ist die korrekte Interpretation der Photoemissionsdaten oftmals nicht möglich.

Weiterhin gilt mein Dank Steffen Schreyeck, der die dünnen Filme Bi_2Te_2Se herstellte sowie Oleg Tereschchenko für die BiTeI Kristalle.

Während meiner Doktorarbeit durfte ich zwei Masterarbeiten betreuen. Einerseits war das die Arbeit von Sonja Schatz, die spinintegrierte Photoemissionsuntersuchungen an dünnen Bi_2Te_2Se Filmen durchführte (ein kleiner Teil ist zu Beginn dieser Arbeit gezeigt), andererseits die Arbeit von Katharina Treiber am Kondosystem $CePt_2$, deren Ergebnisse jedoch keinen Platz in der vorliegenden Dissertation gefunden

haben. Bei beiden habe ich mit Freuden gehört, dass sie so viel Spaß an der wissenschaftlichen Arbeit hatten, dass sie sie nun im Rahmen einer Doktorarbeit in unserer Gruppe fortsetzen. Danke euch beiden für die gute Zeit.

Neben diesen vielen wissenschaftlichen Beiträgen zu meiner Arbeit, haben außer den bereits Genannten, auch viele andere dazu beigetragen, dass meine Zeit an der EP7 mir immer in einer ausgezeichneten Erinnerung bleiben wird. Viel Freude haben mir meine vielen, immer wieder wechselnden Bürokollegen bereitet. Angefangen mit Sina Gusenleitner und Pascal Nigge zu Beginn meiner Doktorarbeit, für einige Zeit Christoph Seibel, dann Katharina Treiber zusammen mit Andreas Benkert und oft zu später Stunde Patrick Bayersdorfer, und ganz zu Ende noch für eine kurze Zeit Max Ünzelmann. Ihnen habe ich eine wunderschöne und lustige Zeit im Büro zu verdanken, geprägt durch eigenwilligen Büroschmuck, ungewöhnliche Gesprächsthemen, geteilte Ohrwürmer, immer einen Grund zu Lachen und auch einen Einblick in physikalische Thematiken, die durch meine Doktorarbeit nicht direkt berührt wurden.

Besonders hat für mich auch PD Dr Achim Schöll den Arbeitsalltag geprägt. Der allmorgentlichen Kaffee mit Milchschaum, viele Ratschläge, die fränkische Schweiz, Kletter- und Bouldercoaching... Danke Achim, für die vielen schönen Momente.

Auch alle anderen Mitglieder der EP7 haben mir die Zeit meiner Doktorarbeit zu einer ganz besonderen gemacht. Zu nennen sind hier zum Beispiel Seminarausflüge in die Rhön und nach Pottenstein, weihnachtliche Begüsse und meine persönliche Auseinandersetzung mit dem Crampus, den Sieg beim Fußballwettspiel zur EM 2016, Grill- und Filmeabende... Vielen Dank euch allen!

Nicht zuletzt habe ich eine besondere Unterstützung durch meine Freunde und Familie bekommen. Der Rückhalt, den ich dadurch hatte, hat einen wesentlichen Beitrag dazu geleistet, dass ich mich sorgenfrei auf meine Arbeit konzentrieren konnte. Meinen wundervollen Freunden danke ich, dass sie immer ein offenes Ohr für mich hatten und haben und mir immer wieder verzeihen, dass die Zeit die ich mir für sie nehme oft knapp ist.

Ganz besonders wichtig ist für mich meine Familie, die mich während meines ganzen Studiums immer unterstützt hat und mich in den richtigen Momenten entweder von der Arbeit weggeholt oder mich darin bestärkt hat. Ihr seid in den letzten Jahren immer für mich dagewesen und habt mir zur Seite gestanden und mich gestützt. Meinen Eltern Maria und Wolfram Maaß und meinen lieben Geschwistern Bernhard und Elrike sowie meinem Onkel Albert Duschl möchte ich hier Danke für Alles sagen.

Danken möchte ich auch meinem Freund Andreas Holm, für die nicht endende Geduld und Unterstützung in den letzten Monaten, positive Ablenkung, das viele gute Essen und die Liebe. Danke, dass es dich gibt!